STUDIA UNIVERSITATIS
BABEŞ-BOLYAI

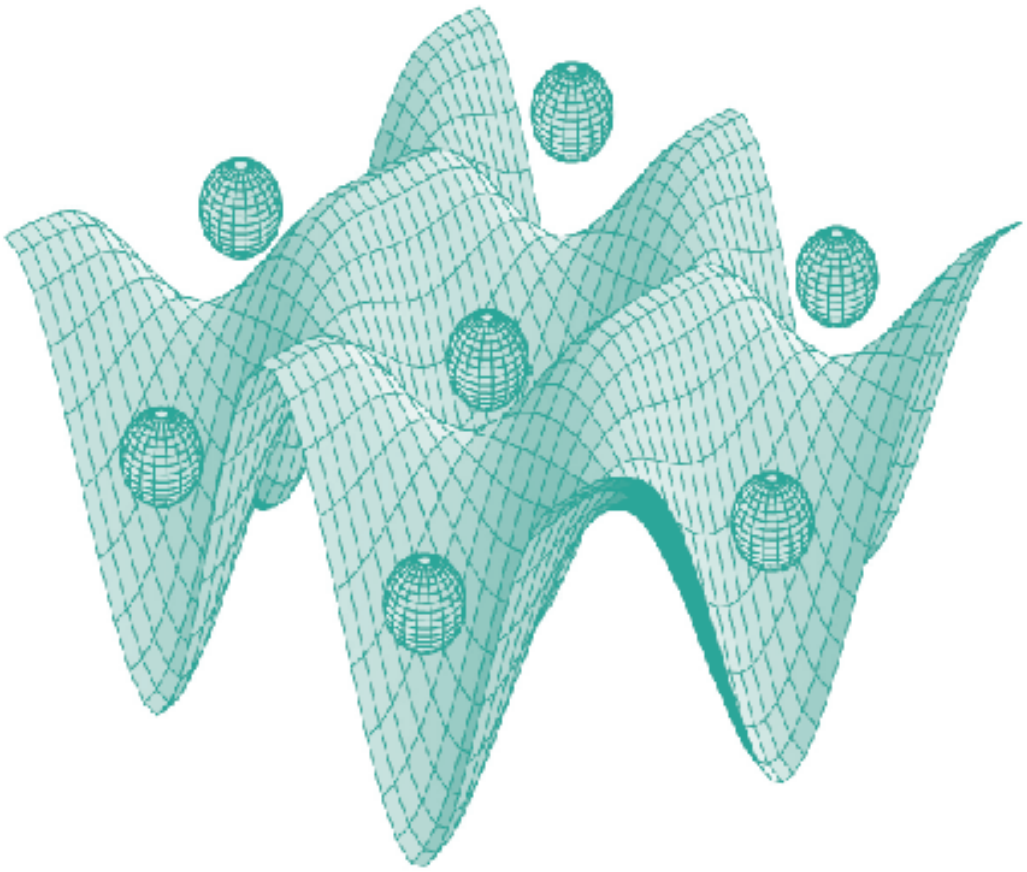

PHYSICA

2/2009

ANUL LIV **2009**

S T U D I A

UNIVERSITATIS BABEŞ–BOLYAI

PHYSICA

2

Desktop Editing Office: 51ST B.P. Hasdeu, Cluj-Napoca, Romania, Phone + 40 264-40.53.52

SUMAR - SOMMAIRE - CONTENTS - INHALT

STUDIA UNIVERSITATIS BABEŞ-BOLYAI, PHYSICA, LIV, 2, 2009

STRUCTURAL CHANGES INDUCED IN MINERAL CLAYS BY HIGH TEMPERATURE HEAT TREATMENTS

M. TĂMĂŞAN[1], H. MOCUŢA[1], C. IONESCU[2], V. SIMON[1]*

ABSTRACT. Thermal changes occurred during firing of clays in order to obtain ceramic samples are important for understanding their properties. In the present paper we report results obtained by thermogravimetric (TGA) and differential thermal analysis (DTA) as well as by X- ray diffraction (XRD) on row and high temperature heat treated clay samples used to produce black-ceramic. TGA and DTA data point out characteristic dehydroxylation and decomposition reactions, and only slight structural changes in the crystalline network up to 700 ^{o}C. For the samples heat treated 1100 ^{o}C and 1200 ^{o}C, the XRD results show the development of magnetite and/or maghemite crystalline phase.

Key words: Clays; heat treatment; structure; DTA; XRD.

1. Introduction

Natural clay minerals are well known and familiar from the earliest days of civilization. Because of their low cost, abundance in most continents of the world, high sorption properties and potential for ion exchange, clay materials are strong candidates as adsorbents. Clay materials possess a layered structure and are considered as host materials. They are classified by the differences in their layered structures. There are several classes of clays such as smectites (montmorillonite, saponite), mica (illite), kaolinite, serpentine, pylophyllite (talc), vermiculite and sepiolite [1]. The adsorption properties result from a net negative charge on the structure of minerals. This negative charge gives clay the capability to adsorb positively charged species. Their sorption properties also come from their high surface area and high porosity [2]. Montmorillonite clay has the largest surface area, around 200 m^2/g, and implicitly the highest cation exchange capacity, while the surface area of illite is only about tens of m^2/g [3, 4].

[1] *Babeş-Bolyai University, Faculty of Physics & Institute for Interdisciplinary Experimental Research, Cluj-Napoca, Romania*
** E-mail: viosimon@phys.ubbcluj.ro*
[2] *Babeş-Bolyai University, Faculty of Biology and Geology*

During the last decades, mineral clays attracted great interest due to their capacity to adsorb not only inorganic but also organic molecules, that was exploited in applications, such as adsorbents for pollutants [5-8], rheological control agents [9], reinforcing fillers for plastics [10], clay-based nanocomposites [11] and precursors for preparing mesoporous materials [12, 13].

This paper reports on structural changes caused by heat treatment applied at high temperatures on panonian age illite clay, with occurrence in Odorheiul Secuiesc area, Romania, as evidenced by thermal analysis, density measurements and X-ray diffraction analysis.

2. Experimental

The clay samples investigated were obtained from natural deposits of in Odorheiul Secuiesc area. This row clay is normally used in producing the traditional Marginea black-ceramic. The samples were washed, air-dried and sectioned as disks sized about 35x30x8 mm. Differential thermal analysis (DTA) and thermogravimetric analysis (DTA) were carried out on Shimadzu type derivatograph DTG-60H, with a heating rates of 5 ºC/min using alumina open crucibles. The samples were heat treated at temperatures ranging between 700^{o}C and 1200^{o}C, for 2 hours, in air under normal pressure. The density of the samples was determined by Archimedes principle using the pan balance. The structure of the non-treated and heat treated samples was investigated by X-ray diffraction with a Shimatzu XRD-6000 diffractometer, using Cu-K_{α} radiation (λ = 1.5418 Å), with Ni–filter.

3. Results and discussion

Thermal analysis runs are given in Fig. 1. The DTA curve of starting material presents three peaks which indicate the thermal changes of the row material. The first endothermic peak corresponds to a large water loss starting at about 50 °C, which is attributed to moisture present in the sample. Another endothermic process takes place about 600 °C where dehydroxylation is substantially complete [14]. At the same time, the mass loss noticed starting with 600 ºC could be related to the elimination of some gaseous species existing in these clay [15]. The weak exothermic event at 330 °C is expected to arise from slight structural changes in the crystalline network or combustion of some organic matter. The temperature at which ancient ceramics and pottery were fired is considered to vary over a wide range (600-1300°C) depending on the type of clay used and the kiln available, although firing temperatures only up to 300-400 ^{o}C have also been suggested [15].

For our sample, the grey colour of the non-heated clay changes to bright brown by heat treatment at 700 °C. By increasing the treatment temperature, the colour becomes more intense and changes to black for the sample heat treated at 1200 °C.

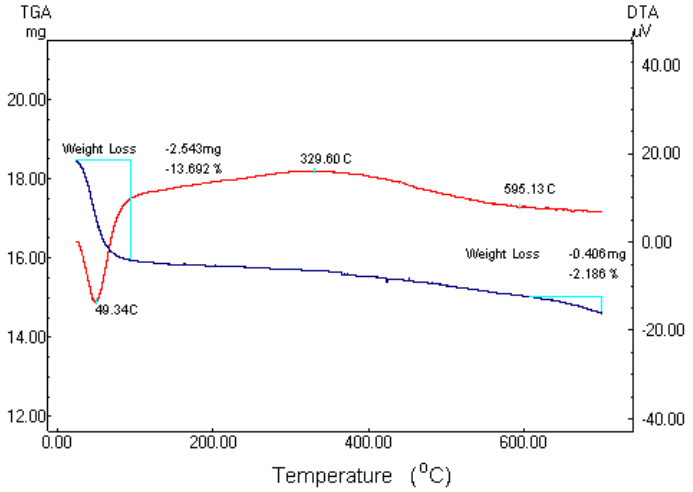

Fig. 1. Differential thermal analysis (DTA) and thermogravimetric (TGA) curves for the non-treated sample.

The change of the density after the applied heat treatments is displayed in Fig. 2. A weak decrease of the density is observed after heating at 700 °C, but this is very pronounced after the heat treatment applied at 800 °C. By further increasing of the treatment temperature, the density starts to enhance and a highly compacted sample results for the sample heat treated at 1200 °C.

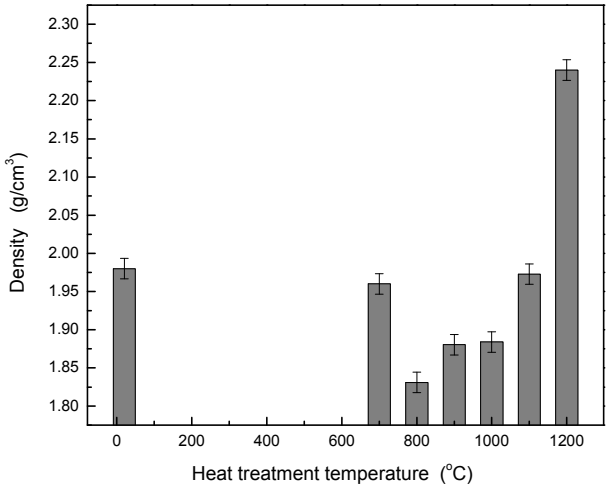

Fig. 2. The density of the row and heat treated samples.

The X-ray diffraction patterns are shown in Fig. 3. A typical illite diffraction pattern [16] with peaks at 8.67, 17.87, 27.83, 36, 37.5 and 45.3^o is recorded from the raw clay sample. Beside the dominant illite phase, kaolinite and quartz components are also identified (Fig. 4). For the samples heat treated between 700 ^{o}C and 1100 ^{o}C the silica polymorph moganite is also present, as suggested be the new diffraction peak recorded at 19.7^o [17]. The increasing crystallinity is shown by the sharpening, up to 1100 ^{o}C, of all diffraction peaks. The two hours heat treatment applied at high temperatures of 1100 ^{o}C and 1200 ^{o}C induce the crystallisation of hematite and magnetite on the account of the iron oxide contained in the clay [18]. The diffraction peaks recorded at 30.2 and 35.6^o clearly point out the prevalence of magnetite in relation with the hematite, because hematite is mainly represented by the 33.2^o diffraction peak. At the same time it is to take care on the fact that the crystal structure of maghemite (g-Fe2O3) is similar to that of magnetite (Fe3O4). The main structural difference between maghemite and magnetite is the existence of vacancies in maghemite, which lowers the symmetry of maghemite (primitive Bravais lattice) with respect to magnetite (face-centered Bravais lattice). Further ordering of the vacancies results in a tetragonal supperlattice structure with c =3a [19-21]. In general, solid-state oxidation of magnetite may result in maghemite formation. Because magnetite and maghemite are very similar in their structures and their XRD patterns, diffraction peaks from magnetite nearly overlap with those from maghemite. Unit cell parameters for magnetite- and maghemite-based cubic setting are 0.840 nm and 0.835 nm, respectively. A slight difference in the unit cell parameters results in a slight shift of all peaks from maghemite towards higher angles with respect to the peaks from magnetite [18]. When magnetite and maghemite coexist together, diffraction peak intensity and peak shape will change as their proportions change and it is difficult to identify them by using powder XRD analysis alone.

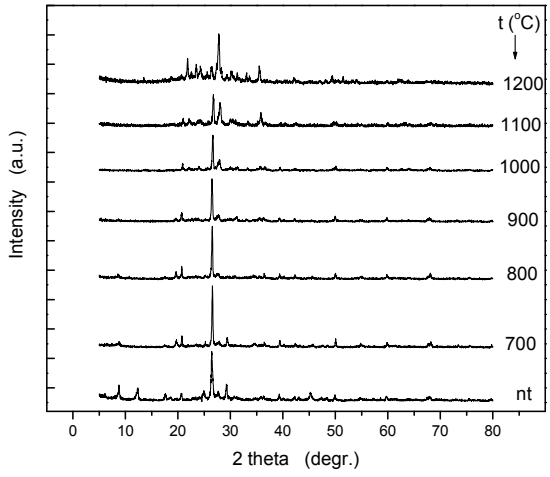

Fig. 3. X-ray diffractograms of non-treated (nt) and heat-treated samples.

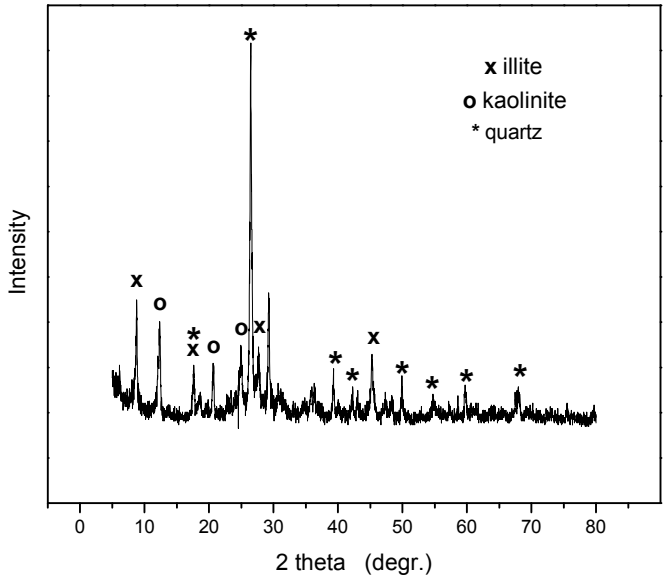

Fig. 4. X-ray diffraction pattern of row clay sample.

The development of magnetite and/or maghemite in our sample is additionally proved by the black colour of the sample heat treated at 1200 ^{o}C. At the same time, one remarks that this sample has the highest density (Fig. 2) and, as already mentioned, it has a glassy glint. A careful inspection/analysis of the corresponding XRD pattern (Fig. 3) evidences the appearance of a vitreous phase giving rise to a very large diffraction line in the 20-30^{o} range of 2θ. Another remarks refers to the slight width broadening of the diffraction lines, that denotes a diminishing of sample crystallinity.

4. Conclusions

The row mineral clay consists of a dominant illite phase, but kaolinite and quartz components are also identified in XRD pattern. DTG and DTA point out characteristic dehydroxylation and decomposition reactions, and only slight structural changes in the crystalline network up to 700 ^{o}C. For the samples heat treated at 1100 ^{o}C and 1200 ^{o}C, the XRD results show the development of magnetite and/or maghemite crystalline phase. Under normal heating conditions at 1200 ^{o}C for two hours, the colour of the grey row clay is changed to black and the sample achieves a glassy glint.

Acknowledgements: The present work was partially supported by the scientific research project PNII 2241/2008 in the framework of Romanian Excellence Research Program.

REFERENCES

1. T. Shichi, K. Takagi, J. Photochem. Photobiol. C: Photochem. Rev., 1, 113 (2000)
2. M. Alkan, O. Demirbas, S. Celikcapa, M. Dogan, J. Hazardous Mater., 116, 135 (2004)
3. L.A.G. Aylmore, I.D. Sills And J.P. Quirk, Clay Clay Miner., 18, 91 (1970)
4. A. Vulpoi, I. Ionescu, V. Simon, Studia, Physica, LIV/1, 11 (2009)
5. M.R. Stackmeyer, Appl. Clay Sci., 6, 39 (1991)
6. L.P. Meier, R. Nueesch, F.T. Madsen, J. Colloid Interf. Sci., 238, 24 (2001)
7. L.Z. Zhu, B.L. Chen, Environ. Sci. Technol., 34, 2997 (2000)
8. L.Z. Zhu, B.L. Chen, X.Y. Shen, Environ. Sci. Technol., 34, 468 (2000)
9. E. Manias, G. Hadziioannou, G. Brinke, Langmuir, 12, 4587 (1996)
10. Z. Wang, T.J. Pinnavaia, Chem. Mater., 10, 3769 (1998)
11. S.S. Ray, M. Okamoto, Prog. Polym. Sci., 28, 1539 (2003)
12. M. Nakatsuji, R. Ishii, Z.M. Wang, K. Ooi, J. Colloid Interf. Sci., 272, 158 (2004)
13. R. Ishii, M. Nakatsuji, K. Ooi, Micropor. Mesopor. Mater., 79, 111 (2005)
14. S. Guggenheim, A.F.K. Van Groos, Clays and Clay Miner., 49, 433 (2001)
15. A. Moropoulou, A. Bakolas, K. Bisbikou, Thermochim. Acta, 269-270, 743 (1995)
16. M.W. Totten, M.A. Hanan, D. Knight, J. Borges, Am. Mineral., 87, 1571 (2002)
17. O. Yong-Taeg, S. Fujino, K. Morinaga, Sci.Techn. Adv. Mater., 3, 297 (2002)
18. T. Chen, H. Xu, Q. Xie, J. Chen, J. Ji, H. Lu, Earth Planet. Sci. Lett., 240, 790 (2005)
19. P.P.K. Smith, Contrib. Mineral. Petrol., 69, 249 (1979)
20. C. Greaves, J. Solid State Chem., 30, 257 (1983)
21. D.R. Lovley, Microbiol. Rev., 55, 259 (1991)

STUDIA UNIVERSITATIS BABEŞ-BOLYAI, PHYSICA, LIV, 2, 2009

SYNTHESIS AND STRUCTURAL CHARACTERIZATION OF SiO_2-CaO-P_2O_5 SOL-GEL DERIVED BIOGLASSES

G. MELINTE[1], M. TĂMĂŞAN, L. BAIA, V. SIMON

ABSTRACT. Bioglasses of composition $55SiO_2$-$41CaO$-$4P_2O_5$ (mol %) were prepared by sol-gel method. The synthesized xerogels was heat treated at different temperatures between 80 ^{0}C and 910 ^{0}C, according to the data obtained from thermogravimetric and differential thermal analyses. The structure of the silica network was investigated by X-ray diffraction and Fourier transform infrared spectroscopy. It was found that an amorphous structure build up the network of the glasses treated at 80 ^{0}C and 300 ^{0}C, while both crystalline and amorphous phases coexist in the samples structure even at high treatment temperature. A less connected SiO_4 network was found to make up the structure of the samples annealed at high temperatures, most probably because of the phosphate units dispersion into the silica network.

Key words: Bioglasses; sol-gel; heat treatment; TGA/DTA; XRD; FTIR.

1. Introduction

Replacement and regeneration of tissues is required in many clinical issues. Since they were discovered in 1969, several kinds of bioactive glasses have been studied for treating damaged and diseased tissues, expecially bones [1, 2]. A bioactive material is defined as a material that elicits a specific biological response at the interface of the material, which results in the formation of a bond between the tissue and that material [3]. The formation of a hydroxycarbonate apatite layer on the surface of bioactive glasses and the release of soluble silica and calcium ions to the surrounding tissue are key factors in the rapid bonding of these to tissues, stimulation of tissues growth and use of tissue engineering scaffolds [4]. Bioactive glasses have been shown to regulate gene expression in both hard and soft tissue repair. New resorbable bioactive glass constructs are now being developed that can influence gene expression in the local environment by manipulating material properties such as the surface structural units, topography and the release of dissolution ions [5].

There have been developed few methods for the preparation of the bioglasses. The traditional one is the melting method used for glass preparation. It is simple and suitable for massive production, but there are difficulties and high costs in the

[1] *Babeş-Bolyai University, Faculty of Physics & Institute for Interdisciplinary Experimental Research*

case of high temperature melting of glasses with high SiO_2 content. In the last decades the sol-gel route has become the major method of bioactive glass preparation. There are several advantages of a sol-gel derived glass over a melt-derived glass which are important for making tissue engineering scaffolds: lower processing temperature, improved purity and homogeneity in the final glass composition, higher bioactivity. It is proved that enhanced bioactivity can be achieved in sol-gel derived materials because of their large specific surface, high porosity and large open pores [6-10].

Sol-gel derived bioglasses in the system of SiO_2-CaO-P_2O_5 have been considered more appropiate for medical applications [11] and therefore in the present paper are presented the structural properties of sol-gel derived $55SiO_2$ - 41CaO - $4P_2O_5$ bioglasses. The samples were heat treated at 80, 300, 550 and 910 °C. The characterization of the structure is important because of the intimate relation between ion release and dissolution properties of bioglasses and their structure and composition. FT-IR spectroscopy was used to determine the structural units that build up the network of the annealed samples and to find out the structural changes that occurred for different thermal treatments. The obtained results were correlated with those obtained from XRD diffraction and TGA/DTA measurements.

2. Experimental

Sol-gel derived bioglass of composition $55SiO_2$ - 41CaO - $4P_2O_5$ (mol%) was prepared by hydrolysis and polycondesation of tethraethyl orthosilicate (TEOS), calcium nitrate tetrahydrate ($Ca(NO_3)_2 \cdot 4H_2O$) and dibasic ammonium phosphate ($(NH_4)_2HPO_4$), mixed in proper amounts. The catalysts used were HCl and NH_3. A small amount (1-2 ml) of concentrated HCl was added to the solution of TEOS with ethanol under a continuous stirring. Double distillated water was used to prepare almost saturated solutions of calcium nitrate and ammonium phosphate. Each solution was consecutively added to TEOS solution under continuous stirring. NH_3 was added to the resulted mixture until gelatinization occurred.

A part of the obtained gel was dried after 30 minutes at 80 °C for 50 min. Other parts of the gel were calcined at 300 °C for 30 min (aged 30 hrs), 550 °C for 30 min (aged 31 hrs) and 910 °C for 1 min (aged 43 hrs).

The thermal behavior of the 80 ^oC dried gel was investigated through thermogravimetric analysis (TGA) and differential thermal analysis (DTA). Analyses were conducted on Shimadzu type derivatograph DTG-60H at a heating rate of 10ºC/min in the temperature range of 28-1000 ºC. Alumina open crucibles were used and the measurements were made in a dynamic nitrogen and air atmosphere at a flow rate of 70 ml/min.

The samples were investigated by X-ray diffraction with a Shimatzu XRD-6000 diffractometer, using CuKα radiation (λ = 1.5418 Å), with Ni–filter. The measurements were performed at a scan speed of 10°/min (80^{o}C dried sample) and 7°/min (300, 550 and 910^{o}C heat treated samples) on a 2θ scan range of 10-80º and as calibrating material it was used quartz powder. Operating power of the X-ray source was 40 kV at 30 mA intensity.

The FT-IR spectra were recorded by using a Bruker Equinox 55 spectrometer. The powdered samples were mixed with KBr in order to obtain thin pellets with a thickness of about 0.3 mm. The IR spectra were recorded with a spectral resolution of 2 cm^{-1}.

3. Results and discussion

The TGA/DTA curves of the gel are shown in Fig. 1. The total weight loss between 35-1000 °C is about 42.5%. The first and most evident weight loss occurs in the range of 35-124 °C (24%) and coincides with an endothermic peak with maximum at 74.47 °C. This is associated to the loss of the residual water and ethanol. Total elimination of the bonding water from the bioglass network occurs in the range of 183-242 °C (3.38%) and coincides with a large endothermic peak. A third weight loss (15.15 %) is observed in TGA curve in the range of 491-562 °C, accompanied in the DTA curve by an endothermic event recorded around 524.37 °C, that can be ascribed to the removal of nitrate radicals and structural hydroxyl groups. A small exothermic peak observed at 920 °C without weight loss marks out a possible structural rearrangement in a crystalline form.

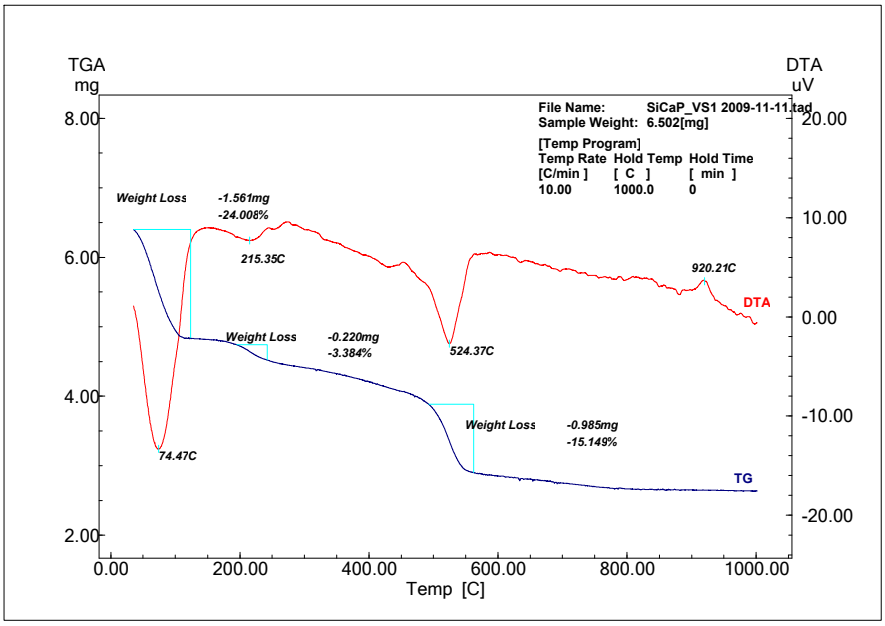

Fig. 1. TGA and DTA curves.

The XRD patterns of the samples heat treated at 80, 300, 550, 910 and 950 °C are illustrated in Fig. 2. The results show an amorphous character for the sample dried at 80 °C and for that annealed at 300 °C. Even after annealing at 550 °C, the vitreous structure appears highly preserved. In the XRD pattern of 910 °C treated sample, the peaks observed at 2θ = 32.5° and 41.5° clearly indicates the occurrence of a crystalline structure. These peaks are attributed to the calcium silicate (Ca_2SiO_4) crystalline phase [12]. Although the sample structure becomes more ordered, the amorphous phase is still present.

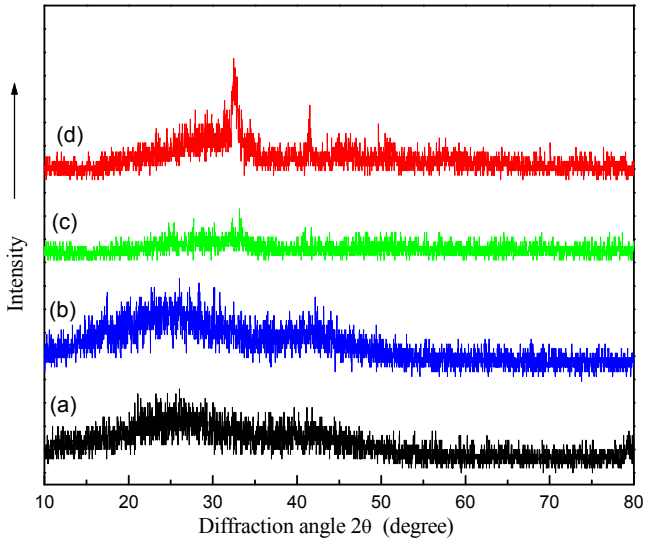

Fig. 2. X-ray diffractograms of samples heat-treated at 80°C (a), 300 °C (b), 550°C (c) and 910 °C (d).

The 400-2000 cm^{-1} spectral range of the FT-IR spectra is shown in Fig. 3. For a better inspection and interpretation of IR spectra this range was divided in three regions: 400-700 cm^{-1}, 700-1250 cm^{-1} and 1250-2000 cm^{-1}.

For the bands arising in the first spectral domain, both SiO_4 and PO_4 unit vibrations are responsible. The infrared bands that appear in the second domain are preponderantly given by SiO_4 unit vibrations. One should note that a well connected SiO_4 network gives rise to infrared bands located around 1200 cm^{-1} (Q_4 units). A less connected SiO_4 structure leads to the appearance of bands at lower wavenumbers, e.g. between 1050 and 1100cm^{-1} for Q_3 units, between 950 and 1000 cm^{-1} for Q_2 units, around 950 for Q_1 units and around 850 for Q_0 units. By looking at the IR spectra presented in Fig. 3 one can observe a diminution of the relative intensities of the bands associated with Q_4 units and an intensity increase for the bands assigned to

Q_3, Q_2 and even Q_0 units, as the heat treatment temperature increases. This spectral behavior could be interpreted in terms of a network with less connected SiO_4 units [13-15]. The infrared bands from the third spectral region are preponderantly given by phosphate unit vibrations. As the heat treatment temperature becomes higher, there can be observed a vanishing of these absorption bands. One can assume that the higher number of isolated phosphate units are dispersed into the network formed by SiO_4 units at higher temperatures. This could be the cause for the structural changes observed in the already discussed spectral region and related to the SiO_4 unit vibrations.

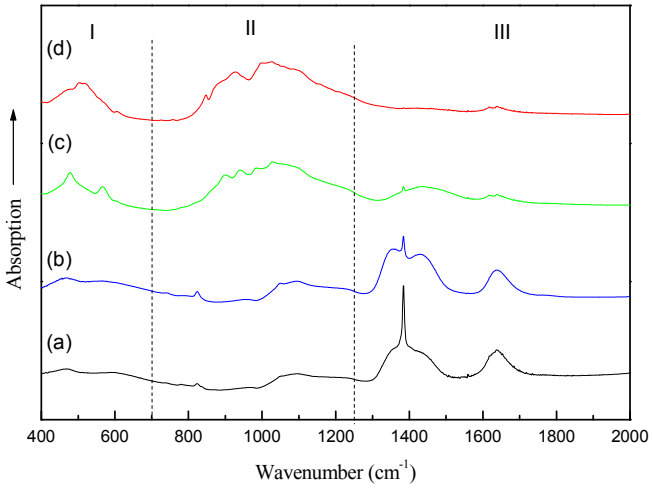

Fig. 3. FT-IR spectra of samples heat-treated at 80°C (a), 300 °C (b), 550°C (c) and 910 °C (d).

Well defined bands located at 1384 cm^{-1} can be also observed in the FT-IR spectra of the samples heat-treated at 80 °C and 300 °C. These bands are associated with residual nitrate ions [16]. In fact, nitrate residues give rise to IR absorption bands at 1384 and 825 cm-1 [17, 18]. Adsorbed water and O-H group bands that appear at 1640 cm^{-1} present a sharp peak for the samples heat-treated at 80 and 300 °C. Once the heat treatment temperature increases, the peak of these bands become less intense and very broad, reflecting the fact that only small amount of structural hydroxyl groups remains in the sample obtained after high temperature treatment.

Conclusions

$55SiO_2$-41CaO-$4P_2O_5$ bioglasses were prepared following the sol-gel route and applying heat treatments at different temperatures between 80 ^{0}C and 910 ^{0}C. DTA/DTG results show that the temperature range of heat treatments applied in

order to remove the residual groups is extended up to 550 ^{o}C, and the development of a crystalline phase is signalized close to 920 ^{o}C. X-ray and FTIR results indicate that crystalline and amorphous phases coexist in the samples heat treated at higher temperatures. A less connected SiO_4 network was found to make up the samples structure of the samples heat treated at high temperatures, most probably because of the phosphate units dispersion into the silica network.

REFERENCES

1. L.L. Hench, J.K. West, Life Chem. Rep., 13, 187 (1996)
2. L.L. Hench, J. Mater. Sci. Mater. Med., 17, 967 (2006)
3. L.L. Hench, Biomaterials, 19, 1419 (1998)
4. D.C. Greenspan, L.L. Hench, J. Biomed. Mater. Res., 10, 503 (1976)
5. G. Jell, M. M. Stevens, J. Mater. Sci: Mater. Med., 17, 997 (2006)
6. T. Peltola, M. Jokinen, H. Rahiala, E. Levanen, J.B. Rosenholm, I. Kangasniemi, A. Yli-Urpo, J. Biomed. Mater. Res., 44, 12 (1999)
7. K. Franks, I. Abrahams, G. Georgious, J.C. Knowles, Biomaterials, 22, 497 (2001)
8. J.D. Santos, P.L. Silva, J.C. Knowles, S. Talal, F.J. Monteriro, J. Mater. Sci. Mater. Med., 7, 187 (1996)
9. M. Tamasan, T. Radu, S. Simon, I. Barbur, H. Mocuta, V. Simon, J. Optoelectr. Adv. Mat., 10, 948 (2008)
10. V. Simon, S. Cavalu, S. Simon, H. Mocuta, E. Vanea, M. Prinz, M. Neumann, Solid State Ionics, 180, 764 (2009)
11. R.M. Vallet-Regi, Biomaterials, 22, 2301 (2001)
12. S. Tsunematsu, K. Inoue, K. Kimura, H. Yamada, Cement Concrete Res., 34, 717 (2004)
13. J. Qian, Y. Kang, Z. Wei, W. Zhang, Mat. Sci. Eng. C, 29, 1361 (2009)
14. D. Carta, J.C. Knowles, M.E. Smith, R.J. Newport, J. Non-Cryst. Solids, 353, 1141 (2007)
15. A. Balamurugan, G. Sockalingum, J. Michel, J. Faure, V. Banchet, L. Wortham, S. Bouthors, D. Laurent-Maquin, G. Balossier, Mater. Lett., 60, 3752 (2006)
16. D.M. Fernandes, R. Silva, A.A.H. Winkler, E. Radovanovic, M.A. Custodio Melo, E.A. Gomez Pineda, Mater. Chem. Phys., 115, 110 (2009)
17. M.W. Glenny, A.J. Blake, C. Wilson, M. Schroder, Dalton Trans., 10, 1941 (2003)
18. M.C. Fernandez-Fernandez, Ru. Bastida, A. Macias, P. Perez-Lourido, L. Valencia, J. Organomet. Chem., 694, 3608 (2009)

STUDIA UNIVERSITATIS BABEŞ-BOLYAI, PHYSICA, LIV, 2, 2009

FORMATION OF GOLD NANOPARTICLE AGGREGATES BY CHEMICAL CROSS-LINKING: UV-VISIBLE SPECTROSCOPY AND SURFACE-ENHANCED RAMAN SCATTERING STUDIES

MILOHUM MIKESOKPO DZAGLI[1,2*], SANDA BOCA[1], MESSANH AGBEKO MOHOU[2], SIMION ASTILEAN[1]

ABSTRACT. Gold has a high affinity to thiol groups (SH) in molecules, leading to the formation of molecular self-assembled layers on the metal surface. In this study, we investigate by UV-visible spectroscopy the modification of optical properties of gold nanoparticle (GNPs) as result of their cross-linking induced by chemical interaction with a dithiolated, bifunctional molecule, here 1,3-propanedithiol (1,3-PDT). The chemical binding of GNPs via 1,3-PDT and formation of molecular layers on gold surface was studied by Surface-Enhanced Raman Scattering (SERS). Correlations between plasmons resonances and nanometer-scale morphology were devised by atomic force microscopy (AFM). The cross-linking of nanoparticles is an important step toward developing plasmonic substrate for biosensing based on metallic networks and nanowires.

Keywords: SERS, gold nanoparticles, self-assembly, dithiol, nanocomposites.

1. Introduction

Noble metal nanoparticles are a subject of investigation in nanoscience in the last years. Nanoparticles share the same size as that of many biomolecules and can be used in vivo or in vitro for cell imaging or biotechnology essay applications. High enhancement of the electromagnetic field at the nanoparticle surface occurs from the excitation of surface plasmons by light. The enhanced near field can be used to design highly sensitive chemical- and bio-sensors [1,2]. Different nanostructured architectures were developped by self-assembly of nanoparticles with the intention to achieve various functionalities in microelectronics, nonlinear optics, catalysis, sensor science and other areas [3,4]. Interesting applications of colloidal metal nanoparticles are created by quantum wires [5], superclusters [6,7] and chains of metal cluster aggregates. Many structures were achieved in colloidal solution by capping metal particles by using alkane-dithiols [6]. Gold has a good affinity to thiol groups forming a

[1] *Babes-Bolyai University, Nanobiophotonics Laboratory, Institute for Interdisciplinary Experimental Research, Treboniu Laurian 42, 400271 Cluj-Napoca, Romania*

[*] *Corresponding author: Permanent address: 02 BP 20427 Lomé-Togo (+228 9876649) Email-address: mdzagli@tg.refer.org*

[2] *Laboratoire de Physique des composants à semi-conducteurs, Université de Lomé, BP 1515 Lomé, Togo*

strong S-Au bond, and this may lead to self-assembled monolayers of dithiol molecule on gold clusters [9]. In particular for molecules containing two thiolated groups the interaction of such molecules with gold nanoparticle (GNPs) can lead to cross-linking of nanoparticles. Complex nanostructures can be resulted also by controlling the attachment of nanoparticles to suitably functionalized surfaces. This is a versatile approach in which long-range ordered bulk nanocomposites[6], thin film structures [10] or well-defined superstructures were formed by particles grouping [11].

The self-assembly of cross-linked nano-networks with nonmetallic electronic conductivity has been reported in previous works [6, 8] using the reaction of colloidal gold nanoparticles with alkaneditiols. Bard and co-workers have fabricated self-assembled spherical ultramicroelectrodes by confining the self-assembly process to the tip end of a quartz micropipet [12]. Dithiols have been used as linkers to bind spherical Au nanoparticles and to assembly nanoparticles onto surfaces. It is possible to build ordered 2D (two dimensional) and 3D structures. Due to the isotropic nature of spherical Au nanoparticles, the selective binding of molecules on surfaces to design 1D nanomaterials will be difficult [13,14].

Surface enhanced Raman scattering (SERS) technique is one of the most sensitive spectroscopic tools available for the detection of a wide range of adsorbate molecules [8]. Surface plasmon resonances of noble metal nanoparticles produce intense electromagnetic fields particularly at the interstitial sites of the nanostructures, enhancing the Raman scattering of molecules residing at the place. Electromagnetic mechanism is especially effective when a cluster of nanoparticles is concentrated in a small spatial region. A combined effect of surface plasmon local fields from different particles acting on a molecule trapped in a gap can result in a giant enhancement of the Raman scattering crossection.

In our study, we focused on optical absorption spectroscopy investigation of the aggregates gold nanoparticles induced by 1,3-propanedithiol (1,3-PDT). We demonstrated the adsorption characteristics of 1,3-PDT on gold by SERS. 1,3-PDT can be present as a mixture of various conformational isomers around the two C-C bonds and the two C-S bonds [15]. We correlated these results with the AFM topography imaging. In particular, 1,3-propanedithiol (1,3-PDT) has affinity to couple many gold nanoparticles, prevent the attachment of two thiol groups to the same gold particle [7]. The terminal thiol group can lead to cross-linking of the colloidal particles which can be demonstrated by the changes induced in their optical absorbance.

2. Experimental

2.1. Materials and methods

Tetrachloroauric acid ($HAuCl_4$), trisodium citrate and 1,3-propanedithiol were purchased from Aldrich. Ultrapure water was used throughout the experiments. All reagents employed were of analytical grade.

The optical absorption spectra of gold colloidal suspension, mixed solution and the solution on the substrate with 1,3-PDT were recorded with a JascoV-670 UV–VIS-NIR spectrophotometer. The mixed solution was dropped on a cleaned quartz substrate and was dried a few minutes at 80^{o}C.

Ordinary Raman spectrum of the neat 1,3-PDT and SERS spectrum of the mixed solution were recorded by a confocal Raman microscope (Witec Alpha300 R) using a 20X objective (NA=0.4) and a 632.8 nm (λ_{ex}) He-Ne laser with a spot diameter of 5 microns and a power of 3 mW.

Atomic Force microscopy (AFM) images of gold nanoparticles aggregates induced by 1,3-PDT dropped on quartz substrate were recorded with a WiTec Alpha 300 AFM microscope, in AC Mode using an aluminum-coated tip.

2.2. Gold nanoparticle synthesis

The colloidal gold was prepared by citrate reduction of tetrachloroauric acid following a previous described procedure [16]. Briefly, 100 ml of 10^{-3}mol.l^{-1} (M) $HAuCl_4$ are brought to a boil by vigorous stirring on a magnetic stirring hot plate. 10 ml of a solution of 38.8 mM trisodium citrate are added to the solution all at once while continuing the stirring process. The yellow solution turned clear, dark blue and then deep burgundy-red within a few minutes. The boiling continued for another 10-15 minutes and then the solution was removed from heat and kept stirring for 15 minutes. The solution final volume was adjusted to 100 ml with deionized water and was stored in clean brown glass bottle until used.

Few microliters of 1,3-PDT were used to yield 5.10^{-3} M to 2.10^{-2} M overall concentration of the surfactant in the hydrosol mixture. The gold clusters were capped with the dithiol molecules (PDT) by mixing 1 ml of gold hydrosol and 0.5 and 2 microliters of dithiol.

3. Results and discussions

We induced the formation of gold nanoparticles nanonetworks by 1,3-PDT cross-linking. We recorded the optical absorption spectra of uncapped gold nanoparticles and gold nanoparticles capped with 1,3-PDT. The figures 1A and 1B show the absorption spectra recorded as a function of time for gold nanoparticles mixed with $2x10^{-2}$ and $5x10^{-3}$mol.l^{-1} dithiol solution, respectively. The spectrum of bare gold nanoparticles is also shown as reference. Two resonances can be seen on the spectra as a result of coexisting two types of structures. The shorter wavelength resonance corresponds to isolated particles capped with dithiol molecules showed by the red shift. Its decrease can be attributed to the decrease of the number of isolated particles. The longer wavelength resonance corresponds to superclusters of gold nanoparticles. The longer wavelength resonance indicates the formation of aggregates gold nanoparticles [17]. The longer wavelength resonance is known to shift to higher wavelengths when the size of the aggregate increases [17]. Our results showed

that the capping of clusters with 1,3-PDT induced the cross-linking of gold nanoparticles which leads to the formation of superstructures of gold colloidal nanoparticles. 1,3-PDT was confirmed to adsorb on gold by forming a single Au-S bond [15].

The formed superstructures can be a network of gold nanoparticles by closeness of nanospheres through the 1,3-PDT molecules linking. The shorter and longer wavelength resonances become more broader in time due to the increasing size of GNPs network. The red shift of both resonances can be explained by the more regrouping of clusters. This means the formation of many Au-S binding by adsorption of other dithiol molecules on the same nanoparticle.

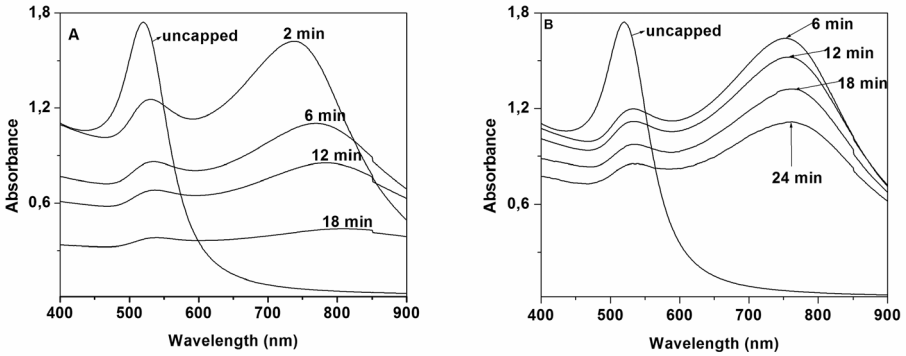

Figure 1. Optical absorption spectra recorded at different times for gold nanoparticle solution mixed with dithiol molecules and uncapped gold sol.
A: 2.10^{-2}M and B: 5.10^{-3}M of 1,3-PDT in final solution.

Figure 2 shows the optical absorption spectra recorded for gold nanoparticles aggregates induced by 1,3-PDT in solution directly and for aggregates dropped on quartz substrate, respectively. The spectrum of gold nanoparticles aggregates induced by 1,3-PDT dropped on quartz substrate is similar to all presented above. The redshift observed for the spectrum of the substrate sample can be explained by the variation on the environmental refractive index from water (1.33) in solution and quartz (1.54) on the substrate.

Figures 3A and 3B show the Atomic Force Microscopy (AFM) topography and 3D-view images of gold nanoparticles capped with dithiol molecule, respectively.

These images show the grouping together of gold nanoparticles induced by the dithiol molecule. This confirms the red shifts observed in the optical absorption spectra presented in this work.

Figure 4 shows ordinary Raman spectrum of the neat 1,3-PDT (figure 4a) and Surface-Enhanced Raman scattering (SERS) spectrum of 10^{-2}M 1,3-PDT in gold sol (figure 4b) respectively, taken in the 200-2700 cm^{-1} wavenumber region. In the Raman spectrum of 1,3-PDT (figure 4a) the band observed at 667 cm^{-1} corresponds to C-S stretching and the bands at 2569 cm^{-1} and 1435 cm^{-1} were assigned to the SH and

CH_2 vibrations, respectively [15, 18]. In the SERS spectrum a strong band at 280 cm^{-1} can be observed which can be attributed to the Au-S vibration [15]. This indicates that 1,3-PDT has adsorbed on gold after the rupture of its thiol proton [17] and suggests that 1,3-PDT should bind to gold forming only one Au-S bond.

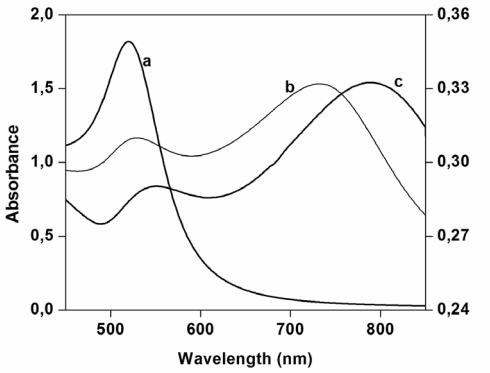

Figure 2. Optical absorption spectra recorded for the capped gold nanoparticle solution with dithiol molecule 10^{-4}M of 1,3-PDT in final solution. a-uncapped gold sol, b-capped gold sol, c-capped gold sol on quartz substrate.

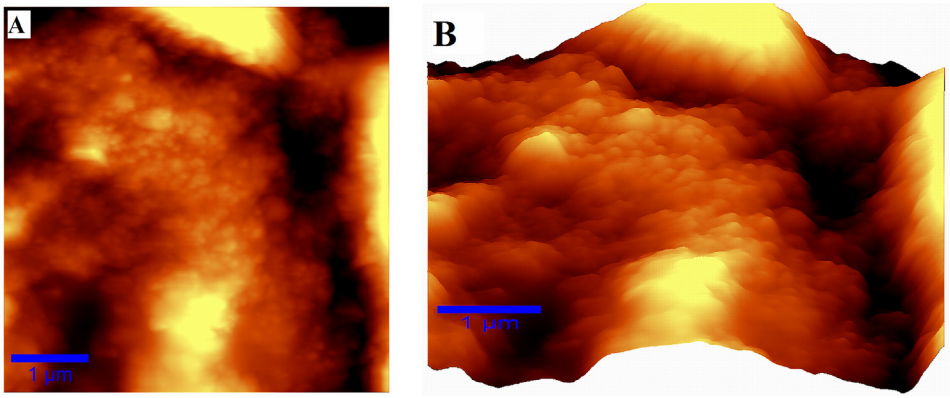

Figure 3. A- AFM Topography and B- 3D view images of gold nanoparticles capped with dithiol molecule 10^{-4}M of 1,3-PDT in final solution.

The concentration of 1,3-PDT required for monolayer coverage was estimated to be 3 x 10^{-6} $mol.l^{-1}$ [19]. We can say that the SERS spectrum shown in figure 4b corresponds to 1,3-PDT on gold above the monolayer coverage. The S-S stretching band, identified at 511 cm^{-1} might represent multilayers of 1,3-PDT on gold by forming

intermolecular S-S bonds. The band at 762 cm^{-1} can be attributed to C-S stretching according to the literature [15, 17]. The appearance of the band at 1415 cm^{-1} can also be associated with the formation of multilayered films [15].

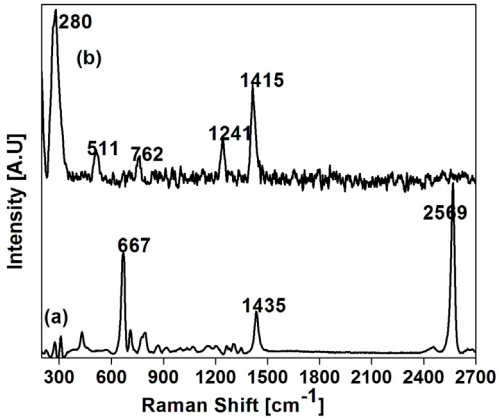

Figure 4. (a) Ordinary Raman spectrum of neat 1,3-PDT.
(b) SERS spectrum of 10^{-2} M 1,3-PDT in colloidal gold sol.

4. Conclusion

In our study, we demonstrated by optical absorption spectroscopy, SERS and AFM measurements the cross-linking of gold clusters capped with a dithiol molecule (1,3-propanedithiol). Moreover, the nanoparticles degree of aggregation can be controlled by adjusting the cluster surface coverage with the dithiol molecule and the contact between the clusters is dependent on the dithiol coverage surface. This cross-linking technique can lead to the generation of ordered assemblies of colloidal particles in solution having optoelectronic properties. Our results showed the formation of plausible nanostructures as nanowires and nano-networks of metal nanoparticles.

Acknowledgements

M. M. Dzagli and M. A. Mohou gratefully acknowledge the financial support from the Agence Universitaire Francophone (AUF) project No CE/MC/466/08 through Eugen Ionescu Program. Other authors (S. Astilean and S. Boca) gratefully acknowledge the financial support from CNCSIS (Project IDEI 477 /2007).

REFERENCES

[1] J.N. Anker, W. P. Hall, O. Lyandres, N. C. Shah, J. Zhao, R. P. Van Duyne, Biosensing with plasmonic Nanosensors, *Nat. Mater.,* 2008, 7, 442-453.

[2] H. Liao, C. L. Nehl, J. H. Hafner, Biomedical applications of plasmon Resonant Metal nanoparticules. *Nanomedicine*, 2006, 1, 201-208.

[3] M. Baia, L. Baia, S, Astilean, Gold nanostructured films deposited on polystyrene colloidal crystal templates for surface-enhanced Raman spectroscopy, *Chem. Phys, Lett.*, 2005, 404, 3-8.

[4] J.B. Jackson, S. L. Wescott, L. R. Hirsch, J. L. West, N. J. Halas, Controlling the surface enhanced Raman effect via the nanoshell geometry, *Appl. Phys. Lett*., 2003, 82, 257-259.

[5] U. Simon, G. Schon and G. Schimid, The Application of Au55 Clusters as Quantum Dots, *Angew. Chem., Int. Ed. Engl.*, 1993, 32, 250-254.

[6] Brust, M.; Bethell, D.; Schiffrin, D. J.; Kiely, C. J., Novel Gold-Dithiol Nano-Networks with Non-metallic Electronic Properties, *Adv. Mater.,* 1995, 7, 795-797.

[7] C. P. Collier, R. J. Saykally, J.J. Shiang, S.E. Henrichs and J.R. Heath, Reversible Tuning of Silver Quantum Dot Monolayers Through the Metal-Insulator Transition*, Science*, 1997, 277, 1978-1981.

[8] F. Toderas, A. M. Mihut, M. Baia, S. Astilean, S. Simion, Self-assembled gold nanoparticules on solide substrate, *Studia Universitas Babes-Bolyai, Phsica*, 2004, XLIX, 3, 89-94.

[9] K. S. Mayya, V. Patil, and M. Sastry, On the Stability of Carboxylic Acid Derivatized Gold Colloidal Particles: The Role of Colloidal Solution pH Studied by Optical Absorption Spectroscopy, *Langmuir,* 1997, 13, 3944-3947.

[10] Colvin, V. L.; Schlamp, M. C.; Alivisatos, A. P., Light-emitting diodes made from cadmium selenide nanocrystals and a semiconducting polymer, *Nature,* 1994, 370, 354-356.

[11] Lawless, D.; Kapoor, S.; Meisel, D., Bifunctional Capping of CdS Nanoparticles and Bridging to TiO2, *J. Phys. Chem.* 1995, 99, 10329-10335.

[12] Demaille, C.; Brust, M.; Tsionsky, M.; Bard, A. J., Fabrication and Characterization of Self-Assembled Spherical Gold Ultramicroelectrodes, *Anal. Chem.* 1997, 69, 9, 2323-2328.

[13] Thomas, K. G.; Kamat, P. V., Chromophore-Functionalized Gold Nanoparticles*, Acc. Chem. Res.* 2003, 36, 888- 898.

[14] Jackson, A. M.; Myerson, J. W.; Stellacci, F., Spontaneous assembly of subnanometre-ordered domains in the ligand shell of monolayer-protected nanoparticles, *Nat. Mater.* 2004, 3, 330-336.

[15] S. W. Joo, S. W. Han and K. Kim, Adsorption Characteristics of 1,3-Propanedithiol on Gold: Surface-Enhanced Raman Scattering and Ellipsometry Study. *J. Phys. Chem.* B 2000, 104, 6218-6224.

[16] H. Xie, A. G. Tkachenko, W. R. Glomm, J. A. Ryan, Franzen, L. Feldheim, Critical Flocculation Concentrations, Binding Isotherms, and Ligand Exchange Properties of Peptide-Modified Gold Nanoparticles Studied by UV−Visible, Fluorescence, and Time-Correlated Single Photon Counting Spectroscopies, *Anal. Chim.*, 2003, 75, 5797-5805.

[17] U. Kreibig and L. Genzel, Optical absorption of small metallic particles, *Surf. Sci.,* 1985, 156,678-700.

[18] Joo, S. W.; Han, S. W.; Kim, K., Multilayer Formation of 1,2-Ethanedithiol on Gold: Surface-Enhanced Raman Scattering and Ellipsometry Study, Langmuir 2000, 16, 5391 5396.

[19] Joo, S. W.; Han, S. W.; Kim, K., Adsorption Characteristics of p-Xylene-α,α‘-dithiol on Gold and Silver Surfaces: Surface-Enhanced Raman Scattering and Ellipsometry Study, *J. Phys. Chem. B* 1999, 103, 10831.

STUDIA UNIVERSITATIS BABEŞ-BOLYAI, PHYSICA, LIV, 2, 2009

SPECTROSCOPIC STUDIES OF SOME METALLIC COMPLEXES WITH PHENYLALANINE AS LIGAND

A. BEBU[1], I.B. COZAR, L. MOGONEA, D. COZMA, CS. NAGY, L. DAVID

ABSTRACT. The $[Cu(L)_2]\cdot H_2O$ (**1**), $[Co(L)_2]\cdot 2H_2O$ (**2**) and $[Zn(L)_2]\cdot H_2O$ (**3**) metallic complexes with phenylalanine (**L**) as ligand were synthesized in aqueous solution and characterized by means of atomic absorption, elemental analysis, differential scanning calorimetry, FT–IR, UV–VIS and ESR spectroscopies.

The elemental analysis and atomic absorption spectroscopy measurements confirm the ratio 1:2 metal ion: phenylalanine composition for the synthesised compounds.

The comparative analysis of the IR spectra for the ligand and the complexes indicate the coordination of the metallic centre to the carboxylic oxygen atom and the nitrogen atom of the amino group due to the shift of the ν_s(C=O) and ν_s(N–H) stretching vibrations. In the ligand spectrum the ν(N–H) stretching vibration appears splitted at 3078 cm^{-1} and 3030 cm^{-1} and is shifted at 3320 cm^{-1} and 3256 cm^{-1} in the copper complex**,** at 3220 cm^{-1} in the cobalt spectrum and at 3256 cm^{-1} and 3334 cm^{-1} for the zinc complex proving the involvement of the $–NH_2–$ group in the complex formation.

The ν(C=O) stretching vibration emerge in the ligand spectrum at 1623 cm^{-1} and appears to be shifted toward higher wave numbers with 4 cm^{-1} and 10 cm^{-1} for Cu and Co complexes and with 9 cm^{-1} toward lower wave numbers for Zn complex.

The free ligand and the complexes exhibit similar spectra in the UV region in relation to the number of absorption bands. The $n\rightarrow \pi^*$ characteristic band in the UV spectra assigned to the C=O bond appear at 231 nm for phenylalanine and is shifted toward lower wave lengths in the complexes spectra proving the covalent nature of the metal-ligand bond.

Powder ESR spectra at room temperature are typically for monomeric species with pseudotetrahedral symmetry around the copper ions and octahedral environment for the cobalt ion.

***Keywords**:* phenylalanine, metal complexes, spectroscopic methods.

1. Introduction

Amino acids are the “building blocks” of the body. Besides building cells and repairing tissue, they form antibodies to combat invading bacteria and viruses; they are part of the enzyme and hormonal system, they build nucleoproteins and carry oxygen throughout the body and participate in muscle activity. When a protein is

[1] *“Babes Bolyai” University, Faculty of Physics, Cluj-Napoca, Romania*

broken down by digestion the result is 22 known amino acids, from which eight are essential and cannot be manufactured by the body, and the rest are non-essential and can be manufactured by the body with proper nutrition.[1,2]

The amino acids in peptides and proteins consist of a carboxylic acid and an amino functional group attached to the same tetrahedral carbon atom. This carbon is the α-carbon. Distinct R-groups, that distinguish one amino acid from another, also are attached to the alpha-carbon. The fourth substitution on the tetrahedral a-carbon of amino acids is hydrogen.[3]

The metallic complexes with amino acids as ligands were deeply investigated due to their capacities of forming chelates, which are used in various domains like: medicine, chemistry, pharmacy, biology, nutrition and physics.[4]

Phenyalanine (Fig.1) is used by the brain to produce Nor epinephrine, a chemical that transmits signals between nerve cells and the brain; keeps you awake and alert; reduces hunger pains; functions as an antidepressant and helps improve memory.

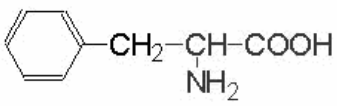

Fig. 1. Structure formula for phenylalanine

2. Experimental

The Elemental analysis measurements were realized with a Vario EL device.

The Differential scanning calorimetry measurements were carried out with a Mettler Toledo 821e device, with a 10^0C/minute heating rate until a 500^0C temperature was reached. The sample size varying from 1 to 2.5 mg, inserted in perforated aluminium crucible and the azoth debit used: 20mL/min. The utilized software is Stare 5.1 [4].

Atomic absorption measurements for the copper complexes were carried out with an AAS-1 device at λ=320nm wave length. The samples were prepared as following: 0.02 g of each complex was weight and dissolved in distillate water; a 5ml quantity of HCl 35% was added, to decompose the complex [4]. Distillate water was added until 100 ml quantity was reached. The dilutions were 1:2.

The iron and zinc dosage were realized with a Shimadzu AA 6300 device at λ=232 nm for iron and λ =219 nm for zinc. The samples were prepared as following: 40-60 mg samples of each compound were weight and dissolved in azothic acid. Regarding the etalon curves, weighted mass and dilution volume, iron and zinc concentrations were calculated.

The cobalt dosage from B_{12} vitamin was through UV-VIS method. The samples were realized as fallowing: 10 mg of the complex were weight and dissolved in 5ml HCl 37%, water was added until 25 ml were reached. From the clorhidric

solution, 5 ml were taken and inserted in a 25 ml balloon. Diluted ammoniac (1:1) was added in order to have a 4-4.5 pH. Afterward 1 ml of acids mixture, 5 ml of nitroso R 0.2% salt and 5 ml of nitrous acetate were added. The mixture was heater until near boiling point was reached, and 5 ml of azothic acid were added, then for 2 minutes the complex was boiled fallowed by cooling. Distilled water was added until the sign was reached. The reading were realized at λ=540 nm.

FT-IR spectra were recorded with a Perkin-Elmer FT-IR 1730 spectrophotometer over KBr solid samples in 4000-400 cm^{-1} range.

UV and visible electronic spectra were performed in λ=190-1100 nm range in aqueous solution, using a standard Jasco V-530 spectrophotometer. By dissolving the complexes in water, 10^{-3} M concentration solutions were prepared, and investigated by spectroscopic means.

Powder EPR measurements were performed at room temperature at 9.4 GHz (X band) using a Brucker ESP 380 spectrometer.

3. Results and discussions

Elemental analysis

The Vario El device allows the quantitative determination of the carbon, nitrogen, hydrogen, sulphur, and oxygen in various operating modes.

For the synthesised copper complexes the elemental analysis results confirm the purposed formulae. Data of the elemental analysis for copper amino acids complexes are illustrated in Table 1.

Table 1.

Elemental analysis results for copper amino acids complexes

Symbolic formulae	Molecular weigth	%C		%H		%N	
		Meas.	Calc.	Meas.	Calc.	Meas.	Calc.
$Cu(L)_2$	391.5	54.79	55.1	7.31	7.66	6.92	7.15
$Co(L)_2$	389.4	51.42	55.46	8.59	8.2	8.28	7.59
$Zn(L)_2$	395	51.85	54.69	9.07	8.10	6.57	7.08

Atomic absorption spectroscopy

The copper, cobalt and zinc complexes theoretical concentrations have similar values with those of the synthesized complex, which demonstrates that complete reaction took place (Table 2).

Table 2.

Copper concentrations obtained by means of atomic spectroscopy

Complex	Metal complex concentration	
	Measured (%)	Calculated (%)
Cu-L	16.37	16.03
Co-L	20,41	19.17
Zn-L	14.52	15.25

Differential scanning calorimetry (DSC)

The differential scanning calorimetry advantages are owed to the direct measurement of the intrinsec thermal properties of the sample and are not invasive and do not need chemical conversion [6]. Differential scanning calorimetry (DSC) was used for a qualitative interpretation of the synthesized complexes.

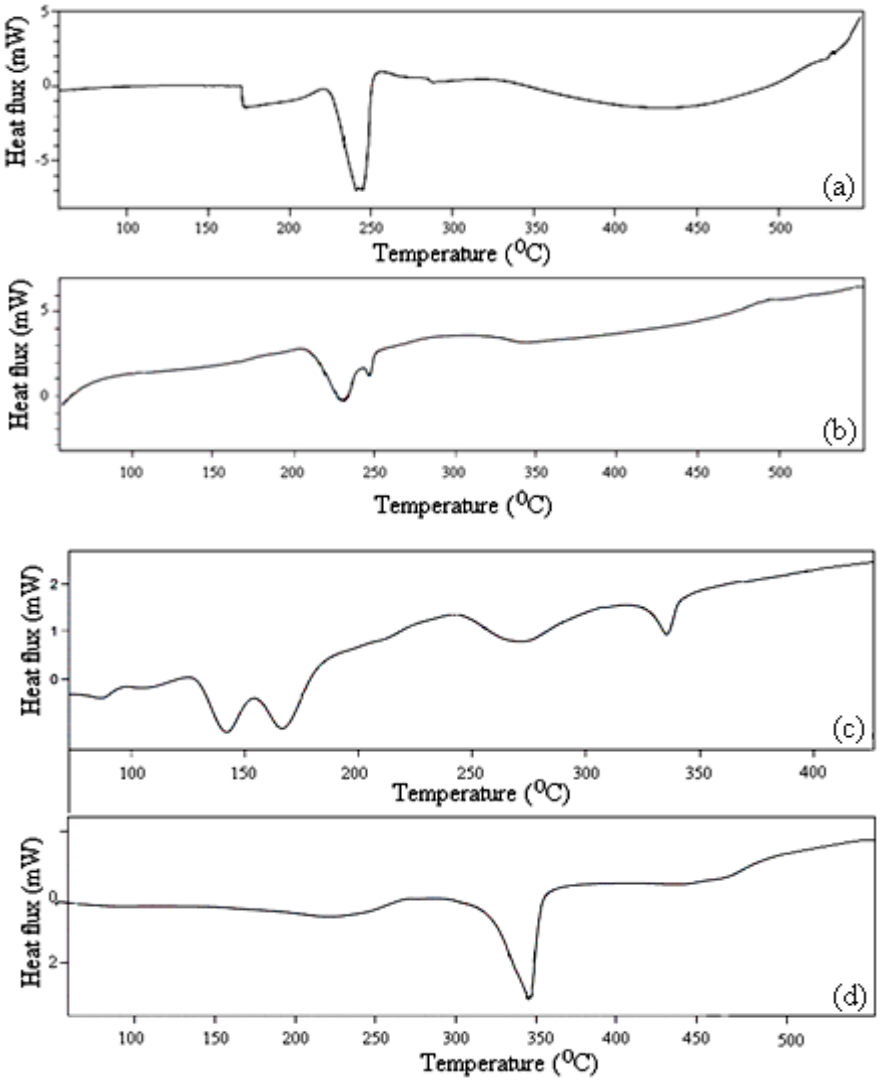

Fig. 2. DSC curves of **L** (a), **1** (b), **2** (c) and **3**(d)

The ligand trace indicates a first glass transition process illustrated at 170^0C, fallowed by phenylalanine melting that takes place with decomposition in 220^0C-260^0C temperature interval, and complete combustion subsequent to 450^0C.

A more complex plot emerges for complex **1** with peaks owing to glass transition between 100^0C and 180^0C and endothermic decomposition pointed up at 230^0C respectively 250^0C. At 300^0C is illustrated the maximum of the exothermic crystallisation process, fallowed by pyrolysis after 450^0C [7].

The DSC trace of complex **3** indicates a melting process fallowed by decomposition in 295^0C-320^0C temperature interval. The complete combustion took place subsequent to 450^0C. The DSC trace for all samples are given in Fig. 2.

FT-IR spectroscopy

Information about the metal ions coordination was obtained by comparing the IR frequencies of the ligand with those of the copper, cobalt and zinc complexes (Fig. 3).

In the spectrum of the ligand, the ν_s(N-H) stretching vibration appears splitted at 3078cm^{-1} and 3030 cm^{-1}, and is shifted at 3320cm^{-1} and 3256cm^{-1} in the complex 1 spectrum, at 3220cm^{-1} and 3334 cm^{-1} for the cobalt complex and at 3256 cm^{-1} in the zinc complex spectra proving the involvement of the $-NH_2-$ group in the complex formation (table 4) [9,10].

The δ(N-H) bending vibration shifting in the complexes spectra also prove the involvement of the $-NH_2-$ group to the metal bonding [9].

The absorption band at 1623 cm^{-1} was attributed to the ν_s(C=O) stretching vibration in the spectrum of the ligand and appears to be shifted toward higher wave numbers in the complexes spectra, at 1629cm^{-1} (**1**), 1633cm^{-1} (**2**) and 1614cm^{-1} (**3**) proving the involvement of the carboxylic group in the covalent bonding to the metal ion [10,11].

Table 4.

FT-IR spectral data (cm^{-1})

Band	L	1	2	3
ν_s(N–H)	3078, 3030	3320, 3256	3220	3334, 3256
N_s(C=O)	1623	1629	1633	1614
ν(O-H)	-	3454	3453, 3359	-
Δ(N-H)	1557	1567	1586	1531

The ν(OH) stretching vibration does not appear in the spectra of the ligand and complex 3, but emerges in the spectra of complexes 1 and 2 complexes at 3454 cm^{-1} respectively 3453 cm^{-1} and 3359 cm^{-1} suggesting the presence the crystal water in these compounds.

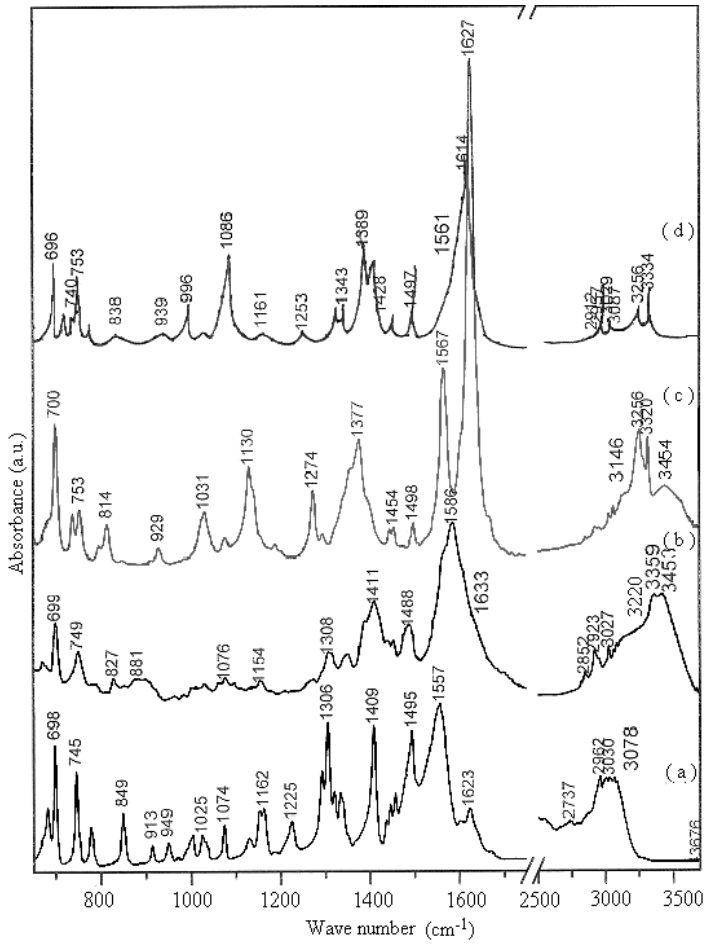

Fig. 3. FT-IR spectra of **L** (a), **1** (b), **2** (c) and **3** (d)

Electronic spectroscopy

Information about local symmetry of metal ions was obtained by comparing the ligand spectra with those of complexes with amino acids [12].

The n→ π* characteristic band in the UV spectra assigned to the C=O bond appear at 231nm for phenylalanine (Fig.4.a) and is shifted toward higher wave lengths at 225nm (**1**), 235nm (**2**) and 220 nm (**3**) confirming the presence of the ligand in the complex [14] and the covalent nature of the metal-ligand bond. In the UV spectrum of the ligand the π→π* characteristic band appears at 260nm, and is shifted in the complexes spectra wit 15nm (**1**), 20nm (**2**) and 7nm (**3**), being assigned to conjugated systems [14].

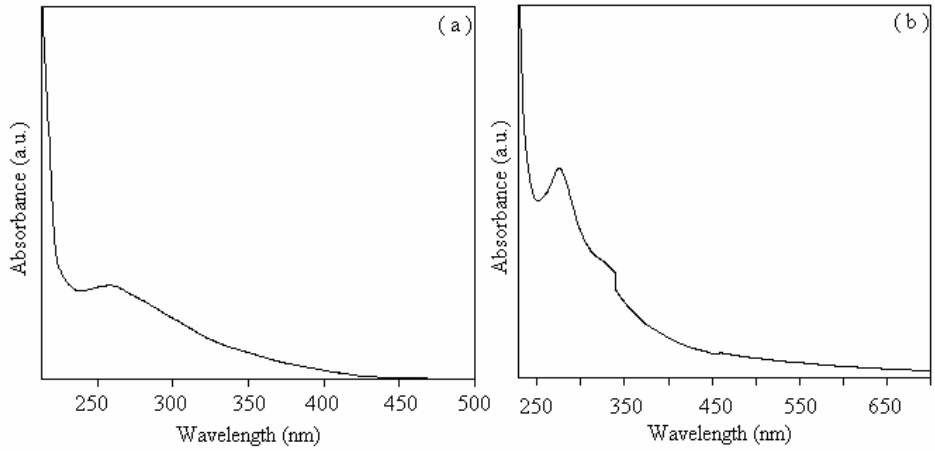

Fig. 4. UV spectra of phenylalanine (a) and Cu-L (b)

In the visible domain (Fig.5) a d–d transition point out at 615 nm in the copper complex spectrum and was assigned to the $^2T_{2g} \rightarrow {}^2E_g$ transition, specific for Cu (II) complexes with tetragonal distortion owing to the Jahn–Teller effect. In the visible domain, the cobalt complex spectrum shows a band at 540nm attributed to the d–d transition of cobalt electrons [15].

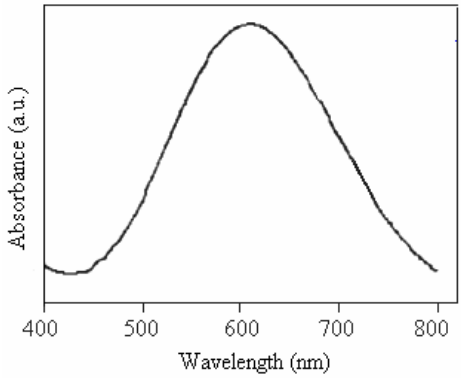

Fig. 5. Visible spectrum of complex **1**

Electronic Spin Resonance spectroscopy

Powder ESR spectra (Fig. 6.a) at room temperature are typical for monomeric species with pseudotetrahedral symmetry around the copper ion (g= 2.009) [16, 17]. The ESR spectrum of complex **1** in DMF solution at room temperature (Fig.6.b) exhibit the copper hyperfine structure with the isotropic parameters: g_0= 2.124, A_0=82G.

The powder ESR spectrum of complex **2** revealed the presence of monomeric compounds, with octahedral symmetry around the cobalt ion, the g tensor value is g= 2.185 [18].

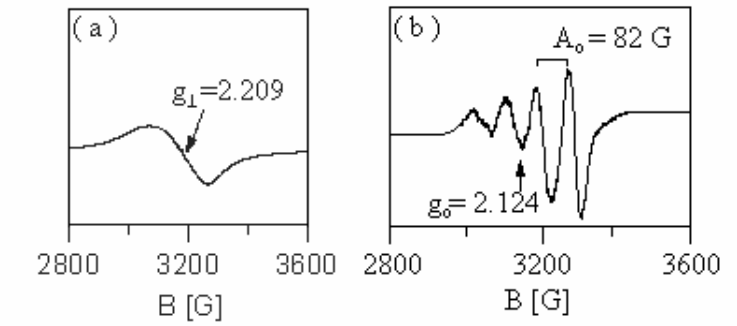

Fig. 6. ESR spectra of complex **1** in powder (a) and DMF solution (b)

4. Conclusions

New metallic complexes with phenylalanine as ligand were synthesised and investigated by thermal and spectroscopic means. The elemental analysis and atomic absorption spectroscopy measurements confirm the ration 1:2 metal ion: phenylalanine composition for the synthesized complexes. The IR spectra show that the amino acid is acting as bidentate ligands with the coordination involving the carbonyl oxygen and the nitrogen atom of amino group. The UV-VIS and ESR spectroscopies confirm the pseudotetrahedral local symmetry around the copper ion and the octahedral symmetry around the cobalt and zinc ions.

The obtained structural data allow us to propose the molecular formulas for the studied metal complexes which are shown in Figure 7.

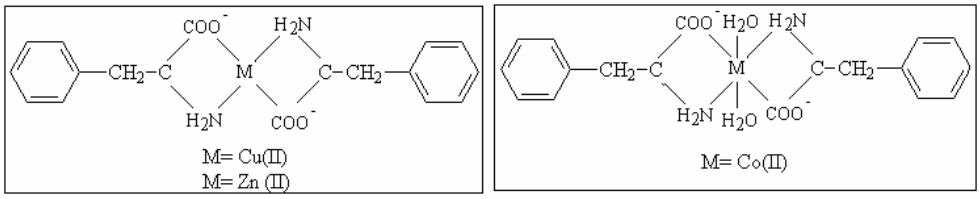

Fig. 7. Structural formulas proposed for the synthesized complexes

BIBLIOGRAPHY

[1] M.Z. Iqbal, S. Khurshid, M.S. Iqbal, J. Pak. Med. Assoc. 40 (9) (1990) 221.

[2] D. Voet, J. Voet, *Biochemistry*, Wiley, New-York (1993).

[3] T. Vemrlinov, S. Arpadjan, I. Karadjova, J. Beattie, Acta Pharm. 56 (2006) 105.

[4] T.B. Choi, W.M. Pardridge, J. Biol. Chem. 261 (14) (1986) 6525.

[5] M. Pope, M. Judd, *Differential Thermal Analysis*, London, Acad. Press, London (1977).

[6] K. Burger, *Coordination Chemistry: Exp. Methods*, Akademiai Kiado, Budapesta (1973).

[7] G. Socrates, *Infrared and Raman Characteristic group frequencies: tables and charts*, third edition, Wiley, Chichester (2001).

[8] B. Schrader, *Infrared and Raman Spectroscopy*, *Methods and Applications*, VCH, Weinheim (1995).

[9] M. Matsushita, T. Irino, T. Komoda, Y. Sakagishi, Clin. Chim. Acta 216 (1993) 103.

[10] G. Malandrinos, K. Dodi, M. Louloudi, Inorg. Chem. 79 (2000) 21.

[11] K. Nakamoto, *Infrared Spectra of Inorganic and Coordination Compounds*, Wiley-Interscience, New York, (1970).

[12] R. Bentley, Biochemistry and Molecular Biology Education, 33 (4) (2005) 274.

[13] S. Zolezzi, A. Decinti, D. Spodine, Polyhedron 18 (1999) 897.

[14] B. L.Silva, P. T. C. Freire, F. E. A Melo, I. Guedes, Araújo Silva, Mendes Filho, A. J. D. Moreno, Brazilian Journal of Physics, 28 (1998) 19.

[15] D. Xiee, J.G. Park, M. Faddak, J. Zhao, H. Khanjoun, J. Biomat. Appl., 21 (2006) 147.

[16] A. Marcu, A. Stanila, D. Rusu, M. Rusu, O. Cozar, L. David, Journal of Optoelectronics and Advanced Materials, 9 (3) (2007) 741.

[17] F. Mabbs, D. Colisson, *Electron Paramagnetic Resonance of d transition Metal Compounds*, Elsevier, Amsterdam, (1992).

[18] S. Bandyopadhyaya, G.N. Mukherjeea, M.G.B. Drewb, Inorganica Chimica Acta**,** 359 (10) (2006) 3243.

STUDIA UNIVERSITATIS BABEŞ-BOLYAI, PHYSICA, LIV, 2, 2009

NANOSIZE EFFECT IN TiO_2 POROUS NANOSTRUCTURES

D. GEORGESCU[1], L. BAIA[1] AND S. SIMON[1, 2]

ABSTRACT. Structural properties of TiO_2 nanostructured porous materials are studied by using Raman spectroscopy and X-ray diffraction (XRD). TiO_2 aerogels have been thermally treated at temperatures ranging between 400 and 525°C, where anatase crystalline phase was found. Different aerogel nanoarchitectures made up from nanoparticles with mean size between 7.62 and 12.87 nm, as obtained from XRD, have been further investigated by Raman spectroscopy. It was found that the intensity, position, full width at half maximum (FWHM) and asymmetry of the most intense TiO_2 anatase Raman bands, i.e. 144 and 638 cm^{-1}, are influenced by nanoparticles dimension. These spectral changes were discussed in terms of nanosize effect. This effect was found to be more pronounced for the smallest nanoparticles.

Keywords: TiO_2 aerogel, nanosize effect, Raman spectroscopy, XRD.

1. Introduction

Aerogels are complex nanostructured porous materials, with low density, but with a very large surface area, as well as a big volume of the pores [1]. This special class of very strong cross-linked structures drew attention owing to their applications, such as the photocatalysis of polluting organic substances, detection of Cherenkov radiation, manufacture of thermal isolators with exceptional properties, preparation of organic polymers, electronic devices, etc [1]. Therefore, the study of structural particularities of such materials is of extreme importance. In the particular case of TiO_2 aerogels three crystalline phases exist, i.e. rutile, anatase and brookite. Anatase phase is of special interest due to its use in applications like photocatalysis, electronic devices, bactericidal potential, etc.

Because all physical properties of nanomaterials are dependent on dimension [2], the aim of the present study is to analyze the structural properties of several TiO_2 porous nanostructures by using Raman spectroscopy and XRD. Because Raman spectroscopy is an excellent tool to investigate the properties of materials at nanometric scale, particular interest was focused on the way in which the intensity, position, FWHM and asymmetry of the most intense TiO_2 anatase Raman bands, i.e. 144 and 638 cm^{-1}, are influenced by nanoparticles dimension.

[1] *Faculty of Physics, Babes-Bolyai University, M. Kogalniceanu 1, 400084 Cluj-Napoca, Romania*
[2] *Institute for Interdisciplinary Experimental Research, Babes-Bolyai University, T. Laurian 42, 400271 Cluj-Napoca, Romania*

2. Experimental

Samples preparation

The TiO_2 gels were prepared by sol-gel method using titanium isopropoxide (TIP), acid HNO_3 catalyst, EtOH and H_2O with 1/0.08/21/3.675 molar ratio. The gels were allowed to age for six weeks and supercritical dried with LCO_2 ($T > 38^0C$ and $p = 1350$ psi) using Tousimis Autosamdri 815 equipment [3]. TiO_2 aerogels were subjected to a thermal treatment at 400, 450, 500 and 525 ^oC for 2h.

Sample measurements

FT-Raman spectra were recorded using a Bruker Equinox 55 spectrometer with an integrated FRA 106 Raman module. A radiation of 1064 nm, a power of 100 mW incidents on sample and a spectral resolution of 1 cm^{-1} were employed for obtaining the spectra of the heat-treated TiO_2 aerogels. The asymmetry calculation was performed after the Raman data were differentiated.

The samples were investigated by X-ray diffraction with a Shimatzu XRD-6000 diffractometer, using CuKα radiation ($\lambda = 1.5418$ Å), with Ni–filter, working at 40 kV and 30 mA.

3. Results and discussion

In the case of TiO_2 the main phase transformations take place around 360 ^0C, when the amorphous structure is transformed into anatase phase, and around 600 ^0C, when the anatase to rutile phase transformation begins [4]. Raman spectra recorded on the heat treated aerogel samples are presented in *Fig. 1a* and show well-defined bands located around 144, 197, 399, 515 and 638 cm^{-1}, typical for fundamental vibrational modes of the anatase phase [5-9].

A close analysis of the spectra reveals a few differences that are better observed when the attention is focused on the most intense band located around 144 cm^{-1} (see *Fig. 1b*). One can see that an increase in intensity, a shift to the lower wavenumbers and a narrowing of this band occur as the thermal treatment temperature increases. The observed spectral modifications could be associated with changes in the particle size [2,4]. If this is the case, with a decrease in particle size the 144 cm^{-1} peak should broadens asymmetrically, shifts to the blue, and decreases in intensity. The physical phenomenon behind this spectral behavior is explained in the next paragraph.

In the Raman scattering process in bulk materials the value of wavenumber for the photons is very small by reported with the phonon wave vector, because $\lambda \gg a$, where λ is the wavelength of photons, and a is the lattice constant. This means that only phonons with $k \approx 0$ have a contribution in the Raman scattering process and in the Brillouin scattering [10].

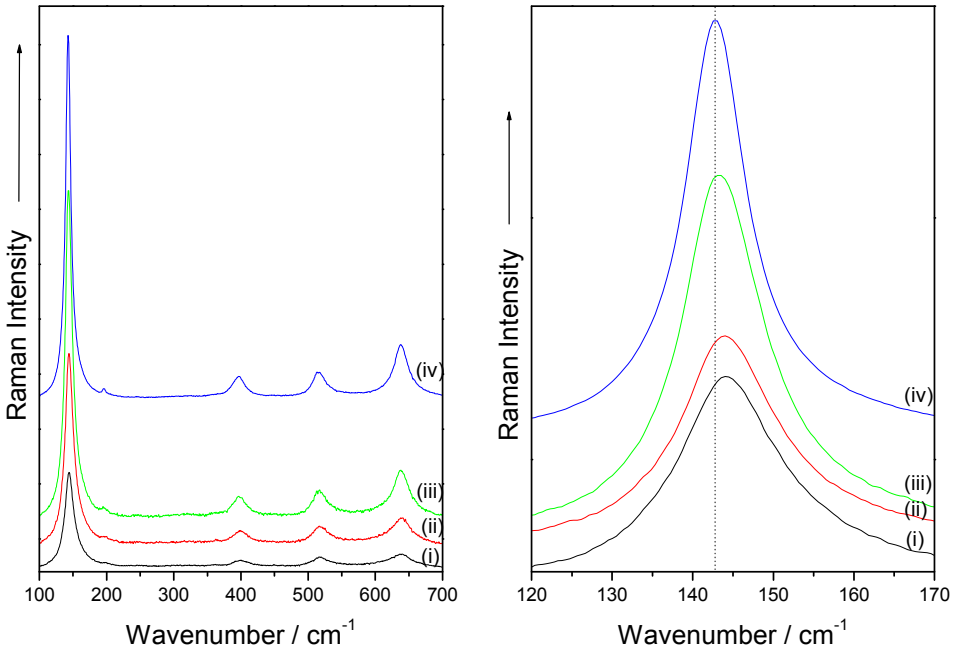

Fig. 1. Raman spectra of the heat treated TiO_2 aerogels (a) together with the spectral details of the 144 cm^{-1} band (b) as follows: (i) 400 ^0C; (ii) 450 ^0C; (iii) 500 ^0C; (iv) 525 ^0C.

In the case of nanosized materials the wave vector selection rules are changed for optical processes, because dimensions of this materials are comparable with phonon wavelength and the description of the elementary lattice excitons with plane waves is not justified anymore. An uncertainty in wave vectors and phonons with $k \neq 0$ can be involved in Raman scattering, because a wave packet have a spatial dimension comparable to the crystallite size. A size reduction increases this uncertainty because the wave packet becomes more localized in real space and consequently the phonons become more dispersed. As the optical phonon dispersion curves are in general not flat new frequencies are introduced in the Raman spectra when contribution from phonons with significantly different wave vectors starts to play a role [10]. For example, based on the Heisenberg uncertainty principle, the relationship between crystallite size (ΔD) and phonon momentum (Δp) is:

$$\Delta D \Delta p \geq \frac{\hbar^2}{4}. \tag{1}$$

As the particle size decreases, the phonon momentum distribution increases. According to the momentum conservation law the broadening of the phonon momentum will cause the broadening of the scattered phonon momentum [11]. This phonon dispersion leads to a asymmetric broadening and a shift of the Raman bands. The nature of the changes and the crystal size at which these changes take place depend on the dispersion curve of the material, and also on the intrinsic phonon lifetime. Normally, the smaller the size, the stronger the spectral changes of the Raman characteristics.

In order to validate the assumed hypothesis of nanosize effect when 144 cm^{-1} Raman band was analyzed, XRD measurements where performed and are presented in *Fig. 2*.

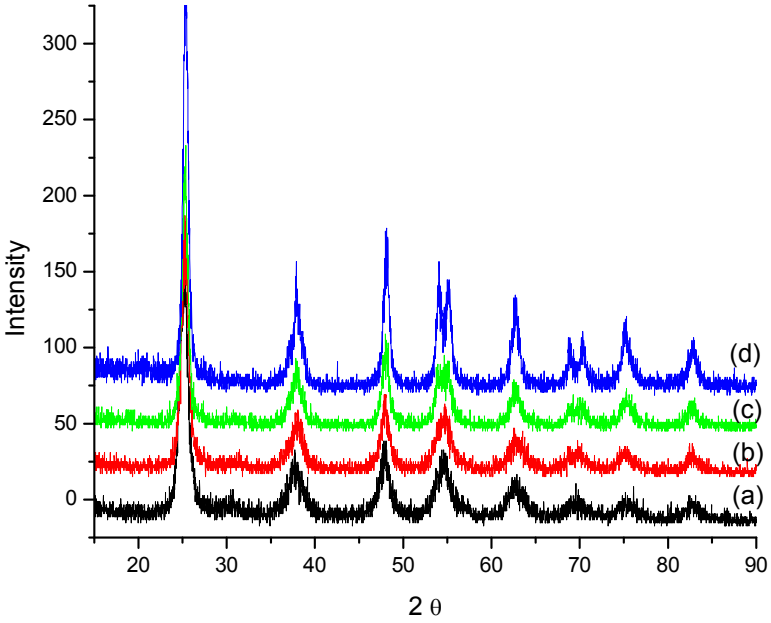

Fig. 2. XRD data of the heat treated TiO_2 aerogels: (a) 400 ^{0}C; (b) 450 ^{0}C; (c) 500 ^{0}C; (d) 525 ^{0}C.

XRD difractograms show peaks characteristic for anatase phase. Lattice parameters of titanium dioxide tetragonal system (a = b ≠ c) have been calculated by using XRD data corresponding to the more intense peak with (1, 0, 1) Miller indices. As expected, thermal treatment induces some changes of lattice parameters. The following equation was used for calculating the *c* parameter:

$$c = \frac{l}{\sqrt{\frac{1}{d^2} - \frac{h^2 + k^2}{a^2}}}, \tag{2}$$

where the interplanar distance *d* and *a* were derived from Bragg equation and experimental data, respectively. The obtained values for the as prepared samples are presented in *Table 1*. Based on XRD data particle mean size of the TiO_2 heat treated aerogels was calculated using Debye-Sherrer formula [12] as can been seen from *Table 1*.

Table 1

XRD data, lattice parameters, and mean size values of the heat treated TiO_2 aerogels.

Heat treatement temperature (^{0}C)	2θ	a (Å)	c (Å)	<D> (nm)
400	25.1175	3.7852	10.0503	7.62
450	25.2650	3.7852	9.5910	8.12
500	25.2590	3.7852	9.6092	11.12
525	25.3294	3.7852	9.4151	12.87

The heat treatment has as consequence the increase of the TiO_2 crystallites size. One can be observed from *Table 1* that there is no comprehensible behavior of *c* lattice parameters for different TiO_2 particles mean size.

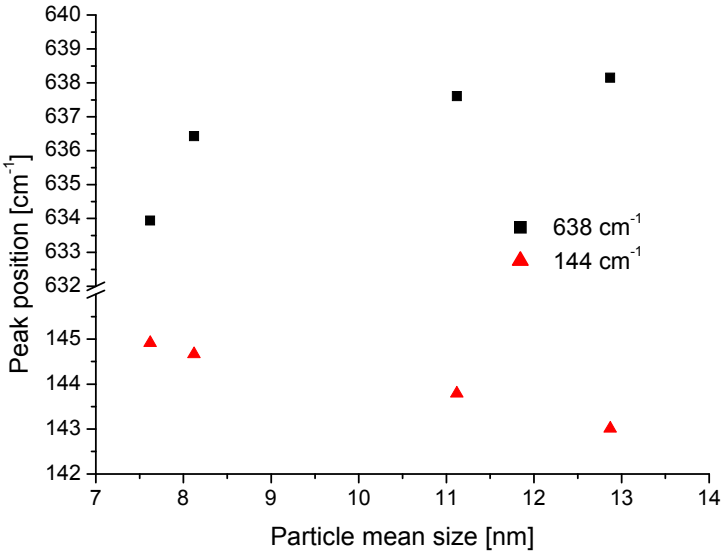

Fig. 3. Peak position deplacement with particle mean size for more intense band situated around 144 cm^{-1} and 638 cm^{-1}.

The peaks position and band half-widths for the Raman characteristics located around 144 and 638 cm^{-1} are displayed in *Fig. 3* and *Fig. 4*. One observes that the position and half-width of these bands are significantly changed as TiO_2 nanoparticles size decreases. The shift of the peak position behaves similarly for both Raman bands (see *Fig. 3*). Unexpected, the change of the nanoparticle size for the 638 cm^{-1} band offer a better discrimination of the half-width in comparison with that obtained for the 144 cm^{-1} peak (see *Fig. 4*).

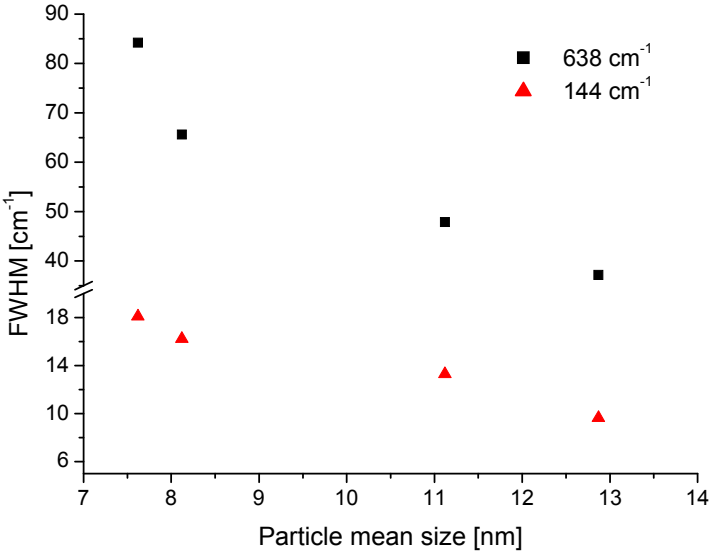

Fig. 4. FWHM dependence with particle mean size for more intense bands situated around 144 cm^{-1} and 638 cm^{-1}.

Additionally, the size reduction should cause the appearance of Raman band asymmetry (see *Fig. 5*). The asymmetry ($\Gamma_{right\ side}/\Gamma_{left\ side}$) is relatively the same for the Raman bands of all samples, excepting the values obtained for the particles with the smallest size. In the case of band located at 638 cm^{-1} the calculated values are higher than those derived for the at 144 cm^{-1} band.

The spectral changes discussed for the Raman bands located around 144 cm^{-1} and 638 cm^{-1} certainly show the evidence of nano-size effect in the case of TiO_2 nanostructures and especially for the particles with the smallest size.

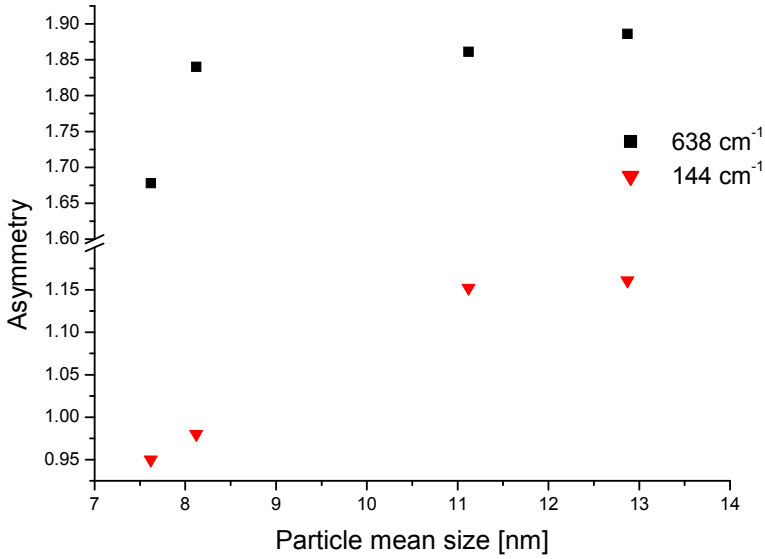

Fig. 5. Asymmetry vs. particle mean size for more intense bands situated around 144 cm^{-1} and 638 cm^{-1}.

4. Conclusion

Nanosize effect was evaluated for several TiO_2 porous nanostructures with dimensions between 7.62 and 12.87 nm. Despite the previously reported data when TiO_2 was investigated it was found that a better discrimination of the band half-width with the nanoparticle size for the 638 cm^{-1} band exists in comparison with that obtained for the 144 cm^{-1} peak. The same effect was observed for the peak position of both Raman bands. The band asymmetry was evidenced for all samples, but no major changes were found for various particles size, excepting the asymmetry values obtained for the particles with the smallest size.

REFERENCES

[1] N. Hüsing, U. Schubert, *Angew. Chem. Int. Ed.* **1998**, 37, 22 – 45.

[2]. S. Kelly, F. H. Pollak, M. Tomkiewicz, *J. Phys. Chem. B* **1997**, 101, 2730 – 2734.

[3]. D. Georgescu, L. Baia, S. Simon, *The 6th International Edition of Romanian Conference on Advanced Materials: ROCAM 2009,* Brasov, Book of abstracts, p. 136.

[4]. M. Šćepanović, Z.Dohčević-Mitrović, M. Grujić-Brojčin, Z. V. Popović, *Appl. Phys*. A **2007**, 86, 365-371.

[5]. L. Baia, A. Peter, V. Cosoveanu, E. Indrea, M. Baia, J. Popp, V. Danciu, *Thin Solid Films* 511-512, **2006**, 512-516.

[6]. S. Balaji, Y. Djaoued, J. Robichaud, *J. Raman Spectrosc.* **2006**, 37: 1416–1422.

[7]. L. Baia, M. Baia, A. Peter, V. Cosoveanu, V. Danciu, *J. of Optoelect.s & Adv. Mater*, (9) 3, **2007**, 668 – 671.

[8]. Y.-H. Zhang, C. K. Chan, J. F. Porter, W. Guo, *J. Mater. Res.*, **1998**, (13) 9, 2602-2609.

[9]. H. C. Choi, Y. M. Jung, S. B. Kim, *Vib. Spectrosc.* **2005**, 37, 33–38.

[10]. D. Nesheva, *J. of Optoelect.s & Adv. Mater.* **2005**, 7(1) 185-192.

[11]. J. E. Spanier, R. D. Robinson, F. Zang, S-W. Chan, I. P. Herman, *Phys. Rev. B,* **2001**, 64, 245007-1-8.

[12]. C. J. Doss, R. Zallen, *Phys. Rev. B,* **1993**, (48) 21, 15626-15637.

STUDIA UNIVERSITATIS BABEŞ-BOLYAI, PHYSICA, LIV, 2, 2009

I.N.A.A. AT DUBNA NUCLEAR REACTOR TRACE ELEMENT CHARACTERIZATION OF OBSIDIAN FOUND IN ROMANIA

O.A. CULICOV[1*], M.V. FRONTASYEVA[1], L. DARABAN[2], V.GHIURCA+[2]

ABSTRACT. We measured the significant elements for provenance studies of obsidians by INAA at IBR-2 pulse reactor from, JINR, Dubna, Rusia.

The aims of this study are to identification an obsidian source in Orasu Nou (Maramures country from Romania).

Comparatively with geological studies, the results of correlation and dendrological diagrams of the analyzed elements from irradiated samples are presented in this paper. Until now the geologist assumed that the obsidian from Oaş area is of a new source. But this isn't confirmed by our experimental results. By this we can say that in Paleolithic these materials were extracted from Slovakia and they were brought by the river Tisa and exchanged for any kind of products.

***Keywords**:* obsidian,corellation, activation analysis, nuclear reactor

1. Introduction

Obsidian is a natural glass of volcanic origin. It is hard and brittle and breaks with conchoidal fracture. It can be readily flaked in any direction and thus fashioned into sharp edges. Where available it was the basic material for making Man's tools until the advent of metals.

Obsidian was widely traded from the restricted areas where it was found and was shaped into tools, weapons and statuary, [1].

Obsidian is certainly the lithic material providing archaeologists with the clearest evidence of contact between different cultures. In fact, obsidian is almost the ideal material for source characterization by elemental analysis. Moreover, it permits analysis, on a methodological level, of factors which could have influenced the choice of deposit by prehistoric people [2].

According to the data of the International Association for Obsidian Studies near to Romanian border exist several defined sourses of obsidian in Slovakia (Banska Stiavnica, Bysta, Cejkov, Hlinik nad Hronom, Kremnitz, Mala Torona, Nora Bana, Sklene Teplice, Streda nad Bodrogom, Szolloske), Hungary (Csepego Forras, Erdobenye, Olaszliska, Tolcsva, Telkibanya, Tokaj) and Ukraine (Beregovo, Gertsovtse-Fedeleshovtse, Khust, Mukacevo). The most investigated are such named Charpathian I and Carpathian II

[1] *Joint Institute for Nuclear Research (JINR), Dubna, 141980, Russia*
[*] *National Research and Development Institute for Electrical Engineering, ICPE-Advanced Research, 74204, Bucharest, Romania*
[2] *"Babeş-Bolyai" University, Cluj-Napoca, 400084, Romania*

sources located in eastern Slovakia and north-eastern Hungary, respectively [3-8]. Acording to the literature data, the Carpathian obsidians are responsible for a few artifacts found even in northern Italy and some as far east as Greek Macedonia, [9], [10].

In the last 30 years a quite large number of Romanian and foreigner specialists were interesed in dating and provenance of obsidian samples found on Romanian territory, [11-14].

Extensive research on obsidian has shown that no sources are found in Romania, [15] despite claims of the existence of such sources in the country [6], [[10], [16], [17].

On the other hand, the obsidians appeared during recent vulcanic erruptions. Some experimental data indicate that the obsidians change to perlit in about 2 thousand years. In this sens, a single region where the vitrous acide vulcanite of recent provenience in Romania exists: Oas mountains, North-Western Romania. With this very zone the hope of Romanian specialists to find a source of obsidian is connected.

It should be mentioned that in the North-Western Romania, the production of obsidian tools is significant, starting with the Aurignacian and evolving throughout the Gravettian [11].

The majority samples investigated in our study are from this very region. Samples of obsidian, riolite and perlite were investigated together with a sample from Slovakia.

The chemical composition of obsidian is not altered in the hands of the artisan, therefore, multielemental analytical techniques are suitable for identification of the patterns in obsidians.

A variety of methods for multielemental characterization and dating of obsidians: PIXE, PIGE, LA-ICP-MS, XRF, PIXE-PIGE-RBS, FTD, SIMS were used in the last fifty years [2], [4], [8],[19],[20],

Nevertheless, instrumental neutron activation analysis (INAA) has been the technique of choice in provenance investigation for a long time [22-25], largely due to the high sensitivity to many trace elements along multiple dimensions of element concentration. It also ensures good precision and accuracy of data compared to other techniques.

The aim of the present research was to identify by means of multielemental characterization and statistical methods the origin of geological and archeological fragments of obsidian.

2. Materials and methods

Conventional and epithermal neutron activation analysis at the IBR-2 pulsed fast reactor of FLNP JINR Dubna, Russia [26], were used to determine the content of 35 elements in 8 samples of obsidian, riolite and perlite (Table 1).

Archeological samples I and IV were found in Ukraina and near Carei, respectively. Geological sample II was found in a slag-heap of bentonite quarry Mujdeni without any references to the original level of exploitation or outcrop. Geological sample III was collected in 1975 in Valea Sunatoare (Turt) at aprox. 18 km NNW

from Orasu Nou. The sample was surrounded by dacites, pumice stone, marl and clay. Sample VI is geological obsidian found in a peroclastic breach (98% pumice stone and 2% obsidian) of panonical age located in the North of Racsa Vii. Samples VII and VIII found in Orasu Nou are riolite and perlite, respectively.

Table 1

Sample location

Nr.	Cod	Location	Type
1.	I	Ungvar	arch
2.	II	Orasu Nou	geo
3.	III	Turt	geo
4.	IV	Carei	arch
5.	VI	Rocsa Vii	geo
6.	SK	Slovakia, Cejkov	geo
7.	VII	Orasu Nou	Riolite
8.	VIII	Orasu Nou	Perlite

Samples of 50 mg were irradiated for 60 seconds and after 2 and 7 minutes γ-ray spectra were obtained for 5 and 12 minutes, respectively. Independently, samples of 100 mg were neutron irradiated for 72 hours. These samples were allowed to decay for 4 and 20 days, and then γ-ray spectra were recorded for 45 and 120 minutes, respectively. All radioactivity values were corrected, taking into account half-life and decay times. Table 2 shows the nuclear data of the identified isotopes and the most important energy peaks of their γ-ray spectra. The relative method on basis of SL-1 (IAEA) and SRM 2709 (NIST) reference materials was used.

3. Results

Results of the NAA analysis of obsidians was presented in the Table 2:

Table 2:

Results of the NAA analysis of obsidians

Index	Name	Na	%	Al	%	K	%	Sc	%	Ca	%
1L	Ungvar	2,25E+04	8,3	7,37E+04	2,3	3,99E+04	9,8	3,24E+00	6,7	5,08E+03	28,5
2L	Proba 2	1,97E+04	8,3	9,84E+04	2,4	3,46E+04	9,9	2,78E+00	6,7	2,09E+04	21,4
3L	Proba 3	2,33E+04	8,3	6,82E+04	2,3	4,01E+04	10,6	3,65E+00	6,7	7,21E+03	18,3
4L	Carei	2,28E+04	8,3	9,89E+04	2,4	4,00E+04	10	3,38E+00	6,7	1,60E+04	22,8
5L	Slovacia	2,16E+04	8,3	7,29E+04	2,3	3,46E+04	10,2	3,23E+00	6,6	8,77E+03	15,7
6L	Racşa	1,58E+04	8,3			3,71E+04	12	3,29E+00	9,2		
7L	Riolit	1,73E+04	8,3	1,18E+05	2,4	4,45E+04	9,1	3,77E+00	6,6	1,30E+04	18,7
8L	Perlit	1,51E+04	8,3	6,54E+04	2,2	3,30E+04	12,5	3,47E+00	6,6	1,24E+04	12,7

Name	Ti	%	V	%	Cr	%	Mn	%	Fe	%
Ungvar	5,56E+02	52,5	9,61E+00	607,7	6,39E+00	392,3	3,79E+02	5	8,04E+03	3,8
Proba 2	1,06E+03	148,2	1,66E+01	206,2	5,62E+00	360,7	4,99E+02	6,1	7,04E+03	3,7
Proba 3	4,83E+02	88,1	6,57E+00	124,4	7,81E+00	300	3,01E+02	4,6	9,85E+03	3,8
Carei	1,04E+03	85,6	1,13E+01	204,3	7,31E+00	320	5,11E+02	5,9	8,37E+03	3,7
Slovacia	4,56E+02	84,5	5,69E+00	103,9	6,36E+00	333,3	3,76E+02	4,5	8,10E+03	3,6
Racşa					2,88E+01	13,4			9,23E+03	9,9
Riolit	1,03E+03	32,8	1,19E+01	66,8	6,55E+00	359,3	5,56E+01	13,1	3,58E+03	5
Perlit	7,62E+02	24,8	8,00E+00	42,4	7,65E+00	521,7	3,49E+02	4,4	1,01E+04	3,4

Name	Zn	%	As	%	Br	%	Sr	%	Rb	%
Ungvar	3,87E+01	5,4	9,44E+00	2,7	2,03E+00	26	6,71E+01	6,2	2,17E+02	9,8
Proba 2	3,35E+01	5,4	8,54E+00	2,7	1,85E+00	26	4,66E+01	7,5	1,95E+02	9,8
Proba 3	5,20E+01	5,3	9,81E+00	2,9	3,93E+00	25,6	7,19E+01	7	1,87E+02	9,8
Carei	3,71E+01	5,4	9,27E+00	2,7	2,10E+00	26	7,41E+01	6,2	2,18E+02	9,8
Slovacia	3,68E+01	5,3	8,69E+00	2,7	1,94E+00	25,9	5,97E+01	6,4	2,09E+02	9,8
Racşa	6,83E+01	9,3	3,18E+01	2,4	1,44E+00	27,9	1,03E+02	17,9	1,72E+02	10
Riolit	2,41E+01	6	1,11E+00	4,4	4,15E-01	35,5	9,01E+01	4,9	1,99E+02	9,8
Perlit	4,08E+01	5,3	4,84E+00	3,5	2,46E+00	25,8	1,11E+02	4,5	1,59E+02	9,8

Name	Zr	Sn	%	Sb	%	Sb	%	Ba	%
Ungvar	1,18E+02	2,27E+01	23,1	5,74E-01	9,7	5,73E-01	10,9	5,02E+02	4,3
Proba 2	9,71E+01	2,43E+01	20,6	5,39E-01	9,7	5,24E-01	10,9	4,06E+02	4,4
Proba 3	1,99E+02	2,04E+01	26,5	4,80E-01	10,1	4,67E-01	11,7	6,23E+02	4,4
Carei	1,18E+02	2,23E+01	23,7	5,96E-01	9,7	5,55E-01	11	5,26E+02	4,4
Slovacia	1,18E+02	2,17E+01	22,2	5,75E-01	9,7	5,72E-01	10,8	4,81E+02	4,4
Racşa	8,52E+01	3,25E+01	48,3	1,50E+00	9,5	1,68E+00	14,3	6,69E+02	6,3
Riolit	2,31E+02	3,17E+01	19,3	7,84E-01	9,6	7,39E-01	10,7	6,64E+02	4,3
Perlit	1,87E+02	1,28E+01	32,5	3,77E-01	10,1	2,42E-01	12,5	5,98E+02	4,3

Name	Cs	%	La	%	Ce	%	Nd	%	Eu	%	Sm	%
Ungvar	1,30E+01	12,7	3,34E+01	6,5	7,27E+01	14,5	1,96E+01	19,7	6,08E-01	12,7	7,17E+00	5,5
Proba 2	1,16E+01	12,7	2,43E+01	6,7	5,24E+01	14,6	1,62E+01	20,8	6,08E-01	11,8	5,75E+00	5,5
Proba 3	9,21E+00	12,7	4,34E+01	6,5	7,87E+01	14,6	3,16E+01	18,4	6,52E-01	13,8	7,00E+00	5,5
Carei	1,28E+01	12,7	2,95E+01	6,6	6,57E+01	14,5	2,41E+01	19,3	6,34E-01	12,3	6,79E+00	5,5
Slovacia	1,21E+01	12,7	2,99E+01	6,5	6,67E+01	14,5	2,27E+01	18,1	3,93E-01	15,3	6,52E+00	5,5
Racşa	9,36E+00	13	2,57E+01	7,3	5,94E+01	16,5	2,90E+01	43,1	2,97E+00	21,2	5,87E+00	5,5
Riolit	1,07E+01	12,7	3,95E+01	6,3	8,08E+01	14,5	3,13E+01	17	1,04E+00	10,6	8,81E+00	5,5
Perlit	2,64E+01	12,7	2,64E+01	6,7	5,74E+01	14,5	2,14E+01	23,3	1,01E+00	9,7	4,60E+00	5,5

Name	Gd	%	Tb	%	Yb	%	Tm	%	Hf	%	Ta	%	W	%
Ungvar	6,74E+00	50,2	1,01E+00	2,2	3,30E+00	18,9	7,49E-01	3,7	2,81E+00	14,1	2,51E+00	2,3	9,49E+00	12,5
Proba 2	5,32E+00	50,2	8,68E-01	2,2	2,92E+00	18,9	6,74E-01	3,7	2,25E+00	14,1	2,18E+00	2,3	6,81E+00	13,4
Proba 3	6,33E+00	50,2	9,82E-01	2,4	2,95E+00	19	5,77E-01	5,1	4,06E+00	14,1	1,62E+00	2,8	5,84E+00	17,7
Carei	5,15E+00	50,2	1,01E+00	2,2	3,25E+00	18,9	7,60E-01	4	2,86E+00	14,1	2,45E+00	2,3	8,48E+00	13
Slovacia	5,04E+00	50,2	9,48E-01	2,1	3,18E+00	18,9	7,23E-01	3,7	2,68E+00	14,1	2,31E+00	2,3	7,28E+00	13,5
Racşa	1,14E+00	113,3	8,61E-01	7,1	2,58E+00	21,5	5,27E-01	13,3	2,98E+00	15,5	1,22E+00	9,2	5,45E+00	20,2
Riolit	3,21E+00	51	1,53E+00	1,9	4,78E+00	18,9	8,23E-01	3,6	3,94E+00	14	1,29E+00	2,8	6,04E+00	13
Perlit	2,70E+00	51,1	7,55E-01	2,2	2,36E+00	19	4,56E-01	4,4	3,67E+00	14,1	1,23E+00	2,7	4,93E+00	18,4

Name	Au	%	Hg	%	Th	%	U	%	Co	%
Ungvar	8,64E-02	503,6	2,38E-01	16,4	1,95E+01	5,1	1,07E+01	8,3	4,67E-01	17,4
Proba 2	7,57E-02	332,6			1,45E+01	5,2	9,42E+00	8,4	2,60E-01	24,3
Proba 3	1,07E-01	309,1			2,18E+01	5,1	5,68E+00	8,5	6,34E-01	16,3
Carei	8,33E-02	319			1,78E+01	5,1	1,03E+01	8,3	3,79E-01	20,1
Slovacia	7,63E-02	295,1			1,80E+01	5,2	9,64E+00	8,3	3,69E-01	18,2
Racşa	1,26E-01	293,3			1,09E+01	5,4	3,57E+00	8,9	1,89E+00	31,6
Riolit	6,33E-02	293,2			1,24E+01	5,2	4,95E+00	8,4	4,48E-01	17,4
Perlit	7,27E-02	781,8			1,14E+01	5,2	3,84E+00	8,5	7,01E-01	12,7

Literature data were also used in order to determine the provenance of obsidian samples (Table 3).

Table 3

Description of samples from literature used in discussions

Nr.	Cod	Location	Type	References
1.	SK1	Slovakia (Streda nad Bodrogom)	geo	[3]Oddone et al., 1999
2.	SK2	Slovakia (Vinicky)	geo	[3]Oddone et al., 1999
3.	SK3	Slovacia (Mala Bara)	geo	[3]Oddone et al., 1999
4.	SK4	Slovakia (Cejkov)	geo	[3]Oddone et al., 1999
5.	SK5	Slovakia (Cejkov)	geo	[3]Oddone et al., 1999
6.	H	Hungary (Tolcsva)	geo	[21]Bugoi et al.,2004
7.	SK6	Slovakia (Vinicky)	geo	[21]Bugoi et al.,2004
8.	R	Romania (Oradea)	arch	[21]Bugoi et al.,2004
9.	P	Romania (Parta)	arch	[13]Salagean et al., 1987

The first attempt to identify possible similarities between new investigated samples was to apply a discrimination factor known from literature [13] (Figure 1).

The riolite and perlite clearly separate from other samples. The geological samples samples III and VI originated from Turt and Racsa Vii, respectively, indicate also another structure.

Using this results and the discrimination factor calculated from elements concentrations:

$$\Delta = (1/Sc)[Cs+Ta+(Rb/100)+(Th+La+Ce)/10] \quad (1)$$

we have constructed an correlation diagram from witch we can say that the samples are from Slovacia where are natural sources of obsidians. Until now the geologist assumed that the obsidian from Oaş area is of a new source.

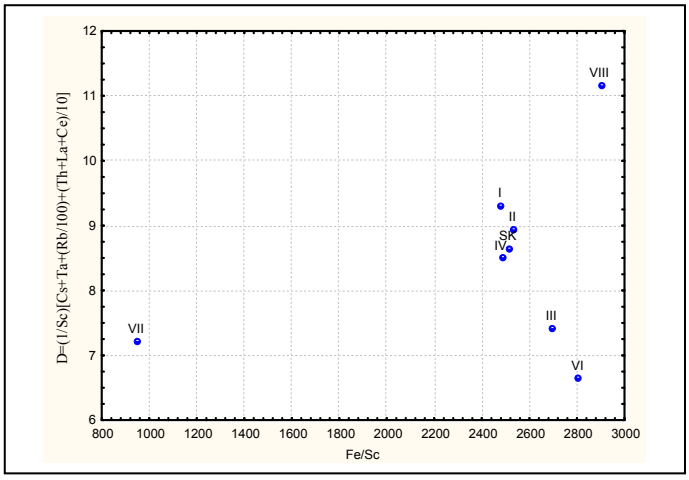

Fig. 1. Discriminant factor versus Fe/Sc

Farther, the cluster analysis was applied to a group of samples formed from our own and data from literature regarding Slovak samples [3]. A very compact Slovak group we remark. The sample II, found in a slag-heap in Orasu Nou joints to this group, but sample III geological from Turt joints to archeological samples I and IV.

When a sample from Parta (Timis region) was included in analysis, we found that this sample of Vinča culture, which previously was compared with samples from Melos and Sardinia, associates very well with Slovak samples.

When the whole set of sample was supplied to cluster analysis, unfortunately for a narrow spectra of elements, we saw that the sample R from Oradea region with an early attributed Slovak origin make a distinguish note.

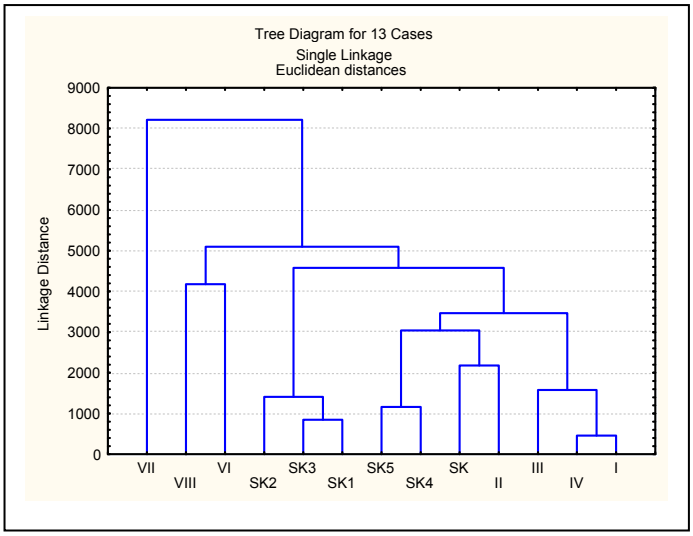

Fig. 2. Dendrogram of obsidian, perlite and riolite samples, including literature data on Slovak geological obsidian ([3]Oddone et al., 1999), based on Na, K, Sc, Cr, Fe, Co, Zn, As, Sr, Rb, Zr, Sb, Ba, Cs, La, Ce, Nd, Sm, Eu, Gd, Tb, Yb, Tm, Hf, Ta, Th, U

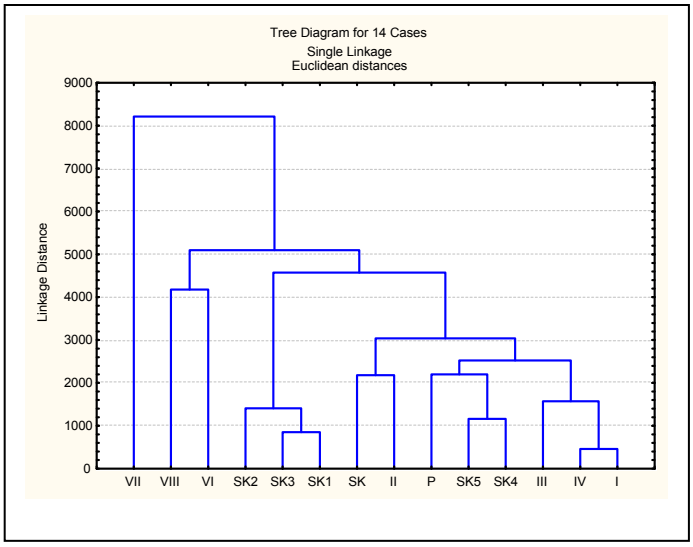

Fig 3. Dendrogram of obsidian, perlite and riolite samples, including literature data on Slovak geological obsidian ([13]Oddone et al., 1999) and Romanian archeological obsidian ([13]Salagean et al., 1987), based on Na, K, Sc, Cr, Fe, Co, Zn, As, Sr, Rb, Ba, Cs, La, Ce, Nd, Sm, Eu, Tb, Yb, Hf, Ta, Th, U

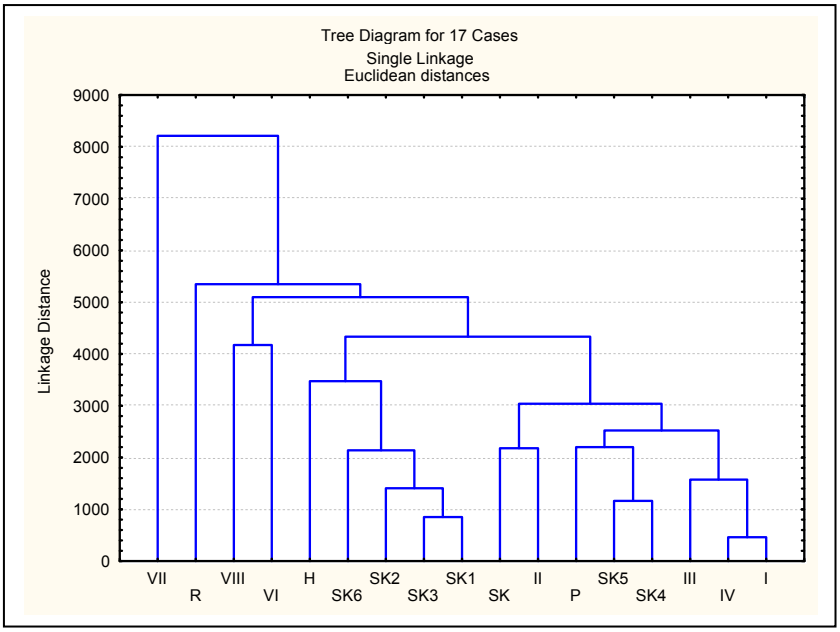

Fig 4. Dendrogram of obsidian, perlite and riolite samples, including all set of experimental and literature data, based on Na, K, Fe, Zn, As, Sr, Rb, Ba

4. Conclusions

The hypothesis regarding a possible source of obsidian in Turt founds a week allusion in our study. This has to be confirmed or not in farther studies including beside Slovak samples, a larger number of Hungarian samples and samples from Zakarpatya, Ukraine;

The earlier suppositions regarding a possible Slovak origin of sample from Parta was confirmed;

The origin of the sample from Oradea has to be investigated in a larger context of samples.

Acknowledgment

The authors wish to thank to: S. S. Pavlov, S. F. Gundorina and T.M. Ostrovnaya for help in carrying out NAA.

REFERENCES

[1] Z. Goffer, *Physical studies of archaeological materials*, Rep. Prog. Phys., Vol. 46, pp 1193-1234, 1983. Printed in Great Britain.

[2] O. Barge, C. Chataigner, *The procurement of obsidian: factors influencing the choice of deposits*, J. Non-Crystalline Solids 323, 172–179, 2003.

[3] M. Oddone, P. Mfirton, G. Bigazzi, K. T. Biro, *Chemical characterisations of Carpathian obsidian sources by instrumental and epithermal neutron activation analysis,* J. Radioanal. Nucl. Chem., Vol. 240, No. 1, 147-153, 1999.

[4] Z. Elekes, K.T. Biro, I. Uzonyi, I. Rajta, A.Z. Kiss, *Geochemical analysis of radiolarite samples from the Carpathian basin,* Nucl. Instr.& Meth. in Phys. Res. B 170:501-514, 2000.

[5] K.Biro, *Carpathian obsidians: myth and reality, in Proceedings of the 34th International Symposium on Archaeometry, Institucion "Fernando el Catolico",* Zaragoza (2006), 267-277, 2006.

[6] Z. Kasztovszki, K. Biro, *Fingerprinting Carpathian obsidian by PGAA: first results on geological and archaeological sources,* in Proceedings of the 34th International Symposium on Archaeometry, Institucion "Fernando el Catolico", Zaragoza, 301-308, 2006.

[7] T. K. Biro, I. Pozsgai, A. Vlader, 1986, Electron beam microanalyses of obsidian samples from geological and archaeological sites. Acta Archaeol. Acad. Sci. Hung., 38, 257-278, 1986.

[8] G. Bigazzi, P.Marton, P.Norelli, L. Rozloznik, *Fission track dating of Carpathian obsidians and provenance identification*. Nucl. Tracks Radiat. Meas. 1990, 17, 391-396, 1990.

[9] K. Randle, L.H Barfield and B. Bagolini, *Recent Italian obsidian analysis,* Journal of Archeological Sciences, 20:503-509, 1993.

[10] V. Kilikoglou, Y. Bassiakos, A. P. Grimanis, K. Souvatzis, A. Pilali-Papasteriou and A. Papanthimou-Papaefthimiou, *Carpathian Obsidian in Macedonia, Greece*, J. of Archaeol. Sci. 23 (3):343-349, 1996.

[11] R. Dobrescu, *Obsidianul din aşezările aurignaciene din nord-vestul Romaniei,* Studii de Preistorie 4, pp. 17-31, 2007.

[12] P. Biagi, B.A. Voytek, 2006, *Excavations at Pestera Ungureasca (Caprelor) (Cheile Turzii, Petresti de Jos, Transylvania) 2003-2004: a preliminary report on the chipped stone assemblages from the chalcolithic toarte pastilate (Bodrogkeresztur) layers,* ANALELE BANATULUI, S.N., Arheologie–Istorie, XIV, 1, 2006 http://www.infotim.ro/mbt/publicatii/ab.htm

[13] M. Salagean, A. Pantelica, L. Daraban, T. Fiat, *Provenance studies of obsidian from the Neolithic Settlement of Prtza in South –Western Romania*, Proc.of the First Romanian Conference on the Application of Physics Methods in Archaeology, Cluj-Napoca, 5-6 Nov. 1987, Ed. P.T. Frangopol and V.V. Moraru, Bucharest, Romania, Vol. **I**, 73-86, 1988.

[14] L. Daraban, C. Cosma, O.Cozar, V. Simon, V. Znamirovschi, I. Ghiurca, M. Salagean, A. Pantelica, *Obsidian provenance studies.* In: Jerem, E. & Biró, K.T. eds., Archaeometry '98. Proceedings of the 31st Symposium, Budapest, April 26-May 3. Vol. II BAR International Series Archaeopress Oxford 1043/II:705-707, 2002.

[15]J. Nandris, 1975, *A reconsideration of the south-east European sources of archaeological obsidian,* in Bulletin London University Institute of Archaeology, 12 (1975), 71-94.

[16] E. Comsa, *Les matieres premieres en usage chez les hommes Neolithiques de l'actuel territoire Rouman*, ActaArchCarp, XVI, 1976, pp. 239-249, 1976.

[17] S.A. Luca, C. Roman, D. Diaconescu**,** 2004, *Cercetări arheologice în Peştera Cauce*, in *Bibliotheca Septemcastrensis*, 4, Editura *Economică*, Sibiu, ISBN 973-590-995-2.

[18] L. Bellot-Gurlet, Th. Calligaro, O. Dorighel J.-C. Dran, G. Poupeau,J. Salomon, 1999, *PIXE analysis and fission track dating of obsidian from South American prehispanic cultures (Colombia, Ecuador),* Nucl. Instr.& Meth.Phys.Res.B 150 ,616 – 662, 1999.

[19] C. E. de B. Pereira, N. Miekeley, G. Poupeaub, I.L. Kuchler, 2001, *Determination of minor and trace elements in obsidian rock samples and archaeological artifacts by laser ablation inductively coupled plasma mass spectrometry using synthetic obsidian standards*, Spectrochimica Acta Part B 56, 1927-1940, 2001.

[20] L.R. Riciputi, J.M. Elam, L.M. Anovitz, D.R. Cole, 2002*, Obsidian Diffusion Dating by Secondary Ion Mass Spectrometry: A Test using Results from Mound 65*, Chalco, Mexico, J.of Archaeological Science, 29, 1055–1075, 2002.

[21] R. Bugoi, B. Constantinescu, C. Neelmeijer, F. Constantin, 2004, *The potential of external IBA and LA-ICP-MS for obsidian elemental characterization,* Nucl. Instr. & Meth. Phys. Res. B 226, 136–146, 2004.

[22] Y.V. Kuzmin, M.D. Glascock, H. Sato, *Sources of Archaeological Obsidian on Sakhalin Island (Russian Far East),* Journal of Archaeological Science (2002) 29, 741–749, 2002.

[23] C. Mandujano, S. Elizalde, G. Cassiano, D. Soto, D. Tenorio, M. Jimenez-Reyes, *Provenance and use wears of Pre-Hispanic obsidian scrapers from Metztitlan, Hidalgo, Mexico*, J. Radioanal. and Nuclear Chem., Vol. 252, No. 1 81–88 (2002).

[24] M. G. Almazan-Torres, M. Jimenez-Reyes, F. Monroy-Guzman, D. Tenorio, P. I. Aguirre-Martinez, *Determination of the provenance of obsidian samples collected in the archaeological site of San Miguel Ixtapan, Mexico State, Mexico by means of neutron activation analysis,* J.Radioanal.Nucl. Chem., Vol. 260, No. 3: 533-542, 2004.

[25] S. Meloni, C. Luglie, M. Oddone, L. Giordani, 2007, *Diffusion of obsidian in the Mediterranean basin in the neolithic period: A trace element characterization of obsidian from Sardinia by instrumental neutron activation analysis*, J.Radioanal.Nucl.Chem., Vol. 271, No.3 (2007) 533–539.

[26] M.V. Frontasyeva, S.S.Pavlov: *Analytical investigations at the IBR-2 reactor in Dubna*, Preprint, E14-2000–177, JINR, Dubna, Russia (2000).

STUDIA UNIVERSITATIS BABEŞ-BOLYAI, PHYSICA, LIV, 2, 2009

SERS INVESTIGATION OF PARACETAMOL ADSORBED ON Ag ISLAND FILMS

L. M. ANDRONIE[1], S. CÎNTĂ PÎNZARU[1], N. PEICA[2], N. LEOPOLD[1], O. COZAR[1]

ABSTRACT. Commercial paracetamol drugs (normal and sinus) are analyzed using Raman and SERS spectroscopies. The active compound present in commercially tablets could be accurately identified and monitored even through the blister pack. Raman spectra show that the normal paracetamol contains a mixture between the monoclinic and orthorhombic forms, while the sinus paracetamol contains just the monoclinic form. The SERS spectra of paracetamol on Ag island films of different roughnesses have been obtained and discussed. From the SERS spectra it was concluded that the paracetamol molecules are chemisorbed on the Ag-surface in a flat orientation through the lone pair electrons of the nitrogen atom and the π electrons of the aromatic ring.

***Keywords**:* Paracetamol, Raman, SERS, Ag island films.

1. Introduction

Paracetamol ($C_8H_9NO_2$) with the molecular structure shown in Fig.1, is one of the largest used antipyretic, needed to reduce the body temperature in situations such as fever. This drug usually diminishes the thermo detection set point of the hypothalamic heat regulatory center, with resulting vasodilatation and diaphoresis [1].

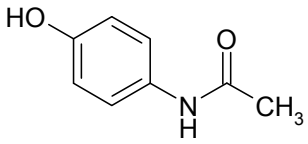

Figure 1. Molecular structure of paracetamol (4-hydroxyacetanilide).

Most antipyretics are also used for other purposes. These drugs are primarily used as analgesics (also known as pain relievers), and are known to act in various ways on the peripheral and central nervous systems.

[1] *Faculty of Physics, Babeş-Bolyai University, Kogălniceanu 1, 400084 Cluj-Napoca, Romania*
[2] *Institut für Festkörperphysik, Technische Universität Berlin, Hardenbergstr. 36, 10623 Berlin, Germany*

Paracetamol can crystallize in three different polymorphic forms known as form I, II and III [2-4]. The monoclinic form (form I) is the normal commercial form [5,6] the form II was identified by recrystallization from an ethanolic solution and corresponds to an orthorhombic form [6,7] and the form III was mentioned as a very unstable form [1,2], which cannot be studied due to its instability. The metastable polymorphs of paracetamol are of particular industrial interest because the commercial form I require binders for tablet formation [8,9]. The form I of paracetamol is stable at ambient temperature and pressure [10,11], while the orthorhombic form of paracetamol is suitable for direct compression tableting and may also be slightly more soluble and may crystallize only in small quantities [11].

Several IR [12,13] and Raman [14,15] studies are already performed in order to characterize and identify the three metastable forms of paracetamol, the transition between them, and the comparison between different structural forms in tablets and solutions samples.

In the present work, we propose the vibrational Raman and SERS characterization of two different commercial paracetamol tablets (normal and sinus).

2. Experimental

Pharmaceutical tablets of paracetamol commercially available (Europharm, Romania), as "normal" and "sinus" (500 mg active substance content), were used in our study without further purification.

The paracetamol normal tablet contains: 500 mg paracetamol, 50 mg maize starch, 30 mg Avicel PH 102, 17.5 mg talc, 17.5 mg Sterotex®, and 30 mg sorbitol. The paracetamol sinus tablet contains: 500 mg paracetamol, 3 mg maleateclorfeniramin, 30 mg pseudo-ephedrine hydrochloride.

The solutions of paracetamol were prepared by dissolving tablets in distilled water. The Ag island films used as SERS substrates in our measurements were prepared through thermal evaporation; the obtained films having different particles roughnesses (between 1.9 and 2.9 Å) as shown in detail in the reference [16].

For the SERS samples processing, we have dropped paracetamol solutions on the film surfaces, and then we kept drying for a number of few minutes. As soon as the drops become dry, the laser spot could be focused on the island films thus resulted.

The Raman and SERS spectra were recorded with a Raman spectrometer (Horiba-Jobin-Yvon, model LabRam) using the 514.5 nm excitation line from an argon ion laser (Spectra Physics, model 2016). The spectra were collected in backscattering geometry using a microscope equipped with an Olympus LMPlanFL 50x objective with a spectral resolution of 2 cm^{-1}. The detection of Raman signal was carried out with a Peltier-cooled CCD camera. The laser power output varied from 100 to 200 mW and is indicated in each figure caption.

3. Results and discussion

A tablet of each paracetamol type (normal and sinus) was dissolved in 10 ml distilled water and then one drop of this solution was kept drying on a glass surface, until the paracetamol recrystallized. The micro-Raman spectra of these samples, for both types of paracetamol (sinus and normal) forms are shown in Fig. 2a and 2b.

These spectra were analyzed by comparing the obtained vibrational bands with those of similar functional groups from the literature [13,14]. The micro-Raman spectra of both paracetamol types, generally present the same band positions and relative intensities with some minor differences.

The bands at 1559, 1099, 725 and 622 cm^{-1} from the normal paracetamol spectrum (Fig. 2a) are specific for the orthorhombic form of paracetamol. The normal paracetamol presents also three intense bands at 1320, 853 and 461 cm^{-1} due to the presence of the excipients lactose and talc [17].The other bands from this spectrum, as previous discussed in the literature [13], were attributed to the monoclinic form of the paracetamol. Thus, we can assume that after recrystallization, the normal paracetamol contain a mixture between monoclinic and orthorhombic forms.

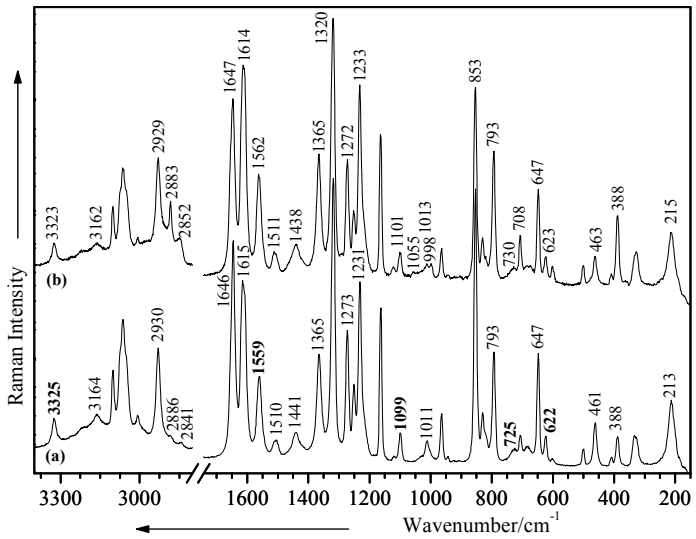

Figure 2. Micro-Raman spectra of recrystallized normal (a) and sinus (b) paracetamol. Excitation: 514.5 nm (a,b), 200 mW (a,b).

The bands at 1562, 1101, 730 and 623 cm^{-1} from the sinus paracetamol spectrum (Fig. 2b) are specific for the monoclinic form of the paracetamol [13]. The bands at 2883 and 2852 cm^{-1} from the same spectrum are also due to the presence of some excipients as cellulose, lactose, talc, stearic acid and magnesium stearate, with characteristic bands in the 2850-2895 cm^{-1} spectral range [18].

One can observe that the peaks at 708 and 388 cm^{-1} (Fig. 2b) from the sinus paracetamol spectrum are more intense as those from the spectrum of the normal paracetamol (Fig. 2a). This increase in relative intensity may be attributed to lactose, which presents strong features in the 864-698 cm^{-1} and 357-377 cm^{-1} spectral ranges. Moreover, the cellulose exhibits a characteristic substantial band around 382 cm^{-1} [19].

Beside the active ingredient 4-hydroxyacetanilide, the paracetamol tablet contains more inactive pharmaceutical substances generically entitled excipients, the common ones including lactose powder, maize starch and microcrystalline cellulose. These inactive ingredients can give additional Raman bands or can amplify and/or shift some bands from the drug spectra.

4. SERS spectra on Ag films

The SERS spectra of normal and sinus paracetamol aqueous solutions ($8x10^{-2}$ M) are presented in Figs. 3 and 4 in comparison with the Raman spectra of the bulk solutions ($3.3x10^{-1}$ M) at pH 5 and pH 7, respectively. Large differences in band positions and relative intensities are observed, allowing the assumption of a chemisorbed species.

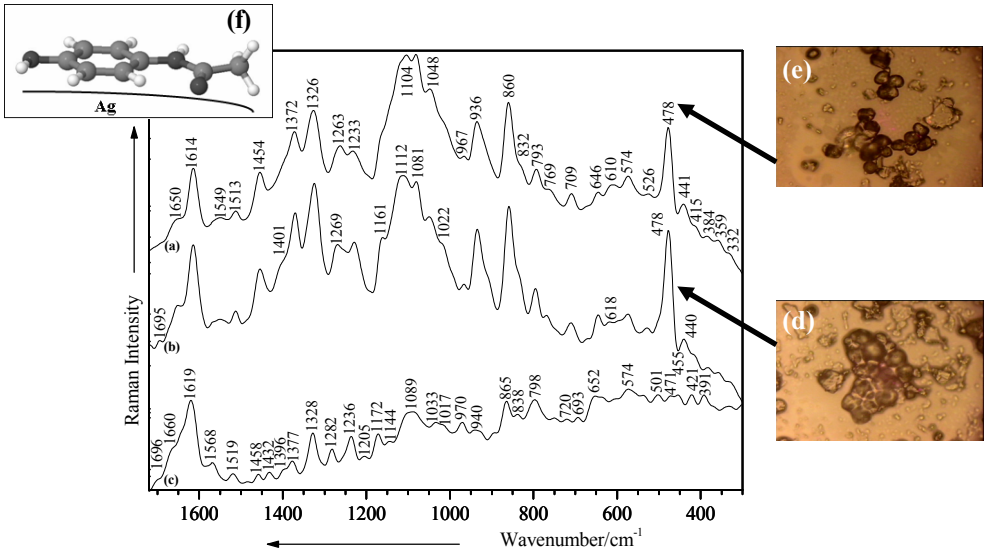

Figure 3. SERS spectra of $8x10^{-2}$ M normal paracetamol on thin silver films of 1.9 Å (a) 2.9 Å (b) roughnesses together with the microscopical images of the measured regions (e), (d) and its proposed orientation on the silver surface (f). Raman spectrum of $3.3x10^{-1}$M normal paracetamol solution (pH 7) (c). Excitation: 514.5 nm (a-c), 200 mW (c) and 50 mW (a,b).

The medium bands observed in the SERS spectra of normal paracetamol at 1263 and 1233 cm^{-1} (19 and 3 cm^{-1} red shifted from the Raman spectrum of the solution) are due to the C-N and phenyl-N stretching modes of the amide group and present changes in the band shape.

In the case of the sinus paracetamol (Fig. 4), the medium bands observed in the SERS spectra at 1270 and 1233 cm^{-1} (5 and 2 cm^{-1} red shifted from the Raman spectrum of the solution) have the same assignment as for the normal paracetamol and show changes in the shape as well. The medium bands at 1172 cm^{-1} (for the normal paracetamol) and at 1164 cm^{-1} (for the sinus paracetamol) in the Raman spectrum of the solution, become shoulders in the SERS spectra and are 11 and 1 cm^{-1} red shifted, being attributed to the C-OH bending modes.

The medium signal at 1089 cm^{-1} in the Raman spectrum of the normal paracetamol solution (Fig. 3) is split in the SERS spectrum in three peaks and one shoulder (1104, 1081, 1048 and 1022 cm^{-1}), which were assigned to the C-OH stretching, asymmetrical C-O-C stretching, CCC bending, and C-OH and phenyl bending modes, respectively.

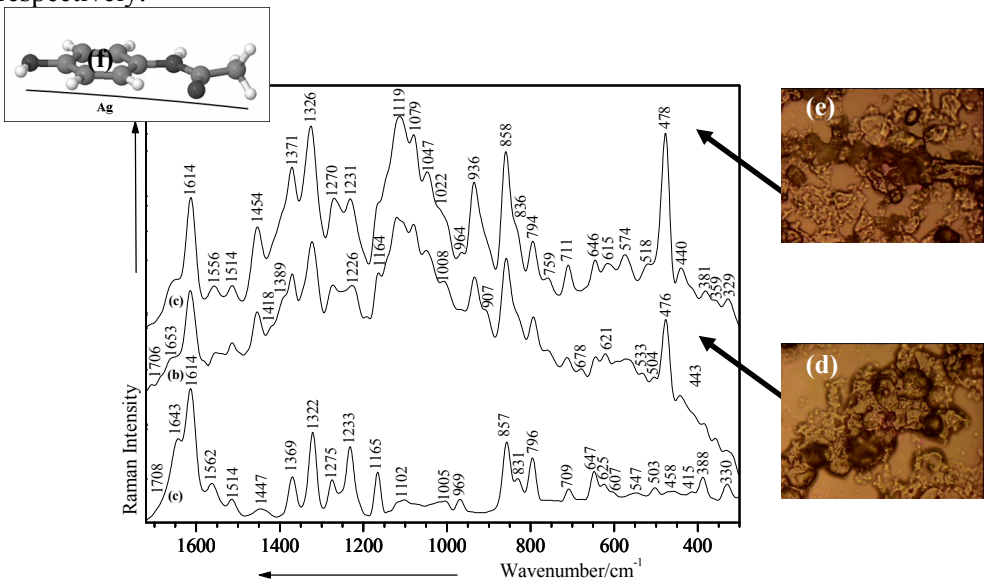

Figure 4. SERS spectra of $8x10^{-2}$ M sinus paracetamol on thin silver films of 1.9 Å (a) 2.9 Å (b) roughnesses, together with the microscopical images of the measured regions (e), (d) and its proposed orientation on the silver surface (f). Raman spectrum of $3.3x10^{-1}$M sinus paracetamol solution (pH 7) (c). Excitation: 514.5 nm (a-c), 200 mW (c) and 50 mW (a,b).

In the case of the sinus paracetamol, the unresolved signal between 1102 and 1000 cm^{-1}, in the Raman spectrum, increases in relative intensity in the SERS spectrum, where three bands (1119, 1079, 1047 cm^{-1}) and one shoulder (1022 cm^{-1}) with the same assignment as for the normal paracetamol can be observed.

The paracetamol molecule can interact with the Ag film surfaces *via* several functional groups. One possibility for paracetamol chemisorption is provided by the presence of the lone pair electrons of the nitrogen and oxygen atoms from the amide group. In this case, according to the surface selection rules [20], the amide I, II, and III bands are expected to be enhanced. Another possibility for paracetamol to chemisorb is through the π electrons of the phenyl ring. In accordance to the electromagnetic selection rules proposed by Creighton [20] and Moskovits and Suh [21], the C-H stretching mode should be relatively enhanced when the C-H bond is perpendicular to the metal surface plane, as compared to the case in which the C-H bond lies parallel to the surface.

The nitrogen interaction with the silver surface is shown by the enhancement of the amide group vibrations. More specifically, the very intense bands in the SERS spectra at 1454, 1372 and 1326 cm^{-1} for the normal paracetamol (Figs. 2a, b); 1454, 1371 and 1326 cm^{-1} for the sinus paracetamol (Figs. 3a, b), red and blue shifted, respectively, from the Raman spectra of the bulk solution (Figs. 3c, 4c), assigned to the symmetrical C=O stretching mode (amide I), to the H_3C-C=O stretching and symmetrical CH_3 bending modes and to the C-N stretching (amide III) mode, are preponderantly due to the amide group, showing its close vicinity to the Ag surfaces.

A flat orientation of the phenyl ring to the metal surface (Figs. 3f, 4f) is supported by the intense band due to the Ag-π electrons of phenyl bond, which can be detected at 478 cm^{-1} and 440 cm^{-1} for the normal paracetamol and at 476 cm^{-1} and 443 cm^{-1} for the sinus paracetamol, respectively, considering both silver film roughnesses.

The flat orientation of the phenyl ring is also supported by the importantly increase in relative intensity of the band at 936 cm^{-1} (in the SERS spectra of both normal and sinus paracetamol, Figs. 3a,b and 4a,b), which is due to the out-of-plane C-H deformation of the phenyl ring, by the highly increase in relative intensity of the bands at 860 cm^{-1} (SERS spectra of normal paracetamol) and 858 cm^{-1} (SERS spectra of sinus paracetamol), which were attributed to the C-H and C-C out-of-plane skeletal deformations.

5. Conclusion

The micro-Raman spectra of paracetamol after recrystallization on the glass surfaces show that the normal paracetamol contains a mixture between monoclinic and orthorhombic forms, while the sinus paracetamol contains just the monoclinic form. The most important bands of some excipients, added in the drug production could be identified.

Taking into account the surface selection rules and the reported literature data, we were able to give a reasonably explication of the adsorbate structures on the Ag metal surfaces from the SERS spectra. A strong chemical interaction of both types of paracetamol (normal and sinus) with the silver island films is realized through the lone pair electrons of the nitrogen atoms from the amide group and the π electrons of the phenyl ring, in a flat orientation.

REFERENCES

1. T. H. Bacon, J. G. Hole, M. North, I. Burnett, *J. Clin. Pharm.* 2002; **53**: 629-636.
2. P. Di Martino, P. Conflant, M. Drache, J. P. Huvenne, A. M. Guyot-Hermann, *J. Therm. Anal.* 1997; **48**: 447-458.
3. T. Beyer, G. M. Day, S. L. Price, *J. Am. Chem. Soc.* 2001; **123**: 5086-5094.
4. A. Rossi, A. Savioli, M. Bini, D. Capsoni, V. Massarotti, R. Bettini, A. Gazzaniga, M. E. Sangalli, F. Giordano, *Therm. Acta*.2003; **406**: 55-67.
5. M. Coen, S. U. Ruepp, J. C. Lindon, J. K. Nicholson, F. Pognan, E. M. Lenz, I. D. Wilson, *J. Pharm. Biomed. Anal.* 2004; **35**: 93-105.
6. S. Morgan, S. Dorman, *Letters*. 2004**; 27**: 99-101.
7. C. H. Florén, P. Thesleff, A. Nilsson, *Med. Scand.,* 1987; **222**: 185-288.
8. P. Espeau, R. Céolin, J. L. Tamarit, M. A. Perrin, J. P. Gauchi, F. Leveiller, *J. Pharm. Sci.* 2005; **94:** 524-539.
9. A. J. Florence, N. Shankland, K. Shankland, W. I. F. David, E. Pidcock, X. Xu, A. Johnston, A. R. Kennedy, P. J. Cox, J. S. O. Evans, G. Steele, S. D. Cosgrove, C. S. Frampton, *J. Appl. Cryst.* 2005; **38:** 249-259.
10. F. Giordano, A Rossi, R. Bettini, A. Savioli, A. Gazzaniga, C. Novák, *J. Therm. Anal. Cal.* 2002; **68:** 575-590.
11. K. V. R. Prasad, R. I. Ristic, D. B. Sheen, J. N. Sherwood, *Int. J. Pharm.* 2002; **238:** 29-41.
12. I. G. Binev, P. Vassileva-Boyadjieva, Y. I. Binev, *J. Mol. Struct.* 998; **447:** 235-246.
13. M. L. Ramos, J. F. Tyson, D. L. Curran, *Anal. Chim. Acta*. 1998; **364:** 107-116.
14. H. A. Moynihan, I. P. O'Hare, *Int. J. Pharm.* 2002; **247:** 79-185.
15. R. Szostak, S. Mazurek, *Analyst*. 2002; **127**: 144-148.
16. Aroca R, Martin F. *J. Raman Spectrosc*. 1985; **16**: 156.
17. B. M. Murphy, S. W. Prescott, I. Larson, *J. Pharm. Biomed. Anal.* 2005; **38**: 186-190.
18. A. Szép, P. Fekete, J. Virgula, Z. Budavári, G. Marosi, *Proceeding of the 8th Polymers for Advanced Technologies International Symposium*, Budapest, Hungary. 2005; 13-16 September.
19. B. M. Murphy, S. W. Prescott, I. Larson, *J. Pharm. Biomed. Anal.* 2005; **38**: 186-190.
20. S. J. Eichhorn, R. J. Young, *Cellulose*. 2001; **8:** 197-207.
21. A. Wang, J. Freeman, K. E. Kuebler, *Lunar and Planetary Science*, **XXXIII**; 2002.
22. J. M. Mercero, J. E. Fowler, J. M. Ugalde, *J. Phys. Chem. A.* 1998; **102**: 7006-7012.
23. T. Shoeib, K. W. M. Siu, A. C. Hopkinson, *J. Phys. Chem. A.* 2002; **106**: 6121-6128.
24. B. Morzyc-Ociepa, D. Michalska, *Spectrochim. Acta A.* 1999; **55:** 2671-2676.

STUDIA UNIVERSITATIS BABEŞ-BOLYAI, PHYSICA, LIV, 2, 2009

FT-MICRO RAMAN PROSPECTS ON FLUORIDE-TREATMENT INFLUENCE ON HUMAN TEETH

S. CÎNTĂ PÎNZARU[1]*, N. HAR[2], M. M. VENTER[3], N. STATOV[4]

ABSTRACT. The aim of the present work was to investigate how the native signal observed in the micro-Raman spectra of tooth enamel and dentin is associated with the conservation procedure after extraction as well as with the fluorinated treatment. This was achieved by analyzing the Raman and IR signal associated with organic components of tooth enamel and dentin, in natural and fluorinated specimens of human permanent molar or children specimen samples. The inorganic/organic content of the two tissues was monitored using the relative intensity ratio of the $\nu(PO_4)^{3-}$, ν(C-H) and $\nu(CO_3)^{2-}$ modes from 958, 2938 and 1446 cm^{-1} respectively. Three different teeth specimens were analyzed after common extraction. The micro-Raman signal was unaffected by the alcohol or methylen blue preservation procedure. The expected vibrational mode of CaF_2 associated to the OH <—> F diffusive exchange was observed as a very weak band in the micro-Raman spectra of enamel after the fluorinated treatment. The fluorinated procedure certainly did not seem to be favored for an increase in the CaF_2 instead, an increase in the crystallinity degree has been concluded, based on the relative intensity ratio and spectral shape of the mineral modes.

Keywords: hydroxyapatite, F-treatment, dentin, enamel, FT-Raman micro-spectroscopy.

1. Introduction

The incidence of dental caries occurs when tooth enamel is exposed to acid produced by bacteria in close proximity of the teeth. Acid production can occur within 5-10 minutes of exposure of the bacteria to sugar, and enamel is dissolved when the pH is below the 'critical' point of about 5.7. When the pH is above 5.7, there is some re-mineralization of the enamel, repairing initial surface damage. According to the recent studies [1], water fluoridation is the most effective public health strategy for caries prevention. Water fluoridation reduces the level of caries in children by about 50% and particularly benefits children from deprived backgrounds. Exposure to very high levels of fluoride during the development of tooth enamel

[1] *Babeş-Bolyai University, Molecular Spectroscopy Dept., Kogălniceanu 1, RO 400084 Cluj-Napoca, Romania*
** Corresponding author. E-mail: scinta@phys.ubbcluj.ro*
[2] *Babeş-Bolyai University, Dept. of Mineralogy, Kogălniceanu 1, RO 400084 Cluj-Napoca, Romania*
[3] *Babeş-Bolyai University, Faculty of Chemistry and Chemical Engineering, Arany Janos 11, RO-400028 Cluj-Napoca, Romania*
[4] *Private Stomatology Clinic "Statov", Cluj-Napoca, Romania*

(up to age 6) can result in enamel with opacity and brown mottling (fluorosis). However, it is not the case, with the appropriate use of fluoride-containing toothpaste and fluoridated water at 1ppm level.

Many spectroscopic studies were recently employed in order to get insight the structure-function relationship of the tooth components [2-13]. The mechanism of ablation of dental enamel investigated at different IR laser wavelengths varied markedly depending on whether the laser energy was coupled to the water or coupled to the mineral [2]. It was shown that the ablation was initiated at temperatures above the melting point of hydroxyapatite during irradiation with 9.6 μm CO_2 laser. Absorption spectra and SEM were used to support the hypothesis that the spatial distribution of water and mineral in the enamel microstructure is responsible for the mechanistic differences in ablation observed under different IR wavelength regions [2]. Moreover, the fluoride-treatment (F-treatment) both after Er:YAG and before CO_2 laser irradiation improved the acid resistance of enamel [3]. Investigations on the caries-preventive effect of calcium fluoride have been seriously hampered by the lack of adequate detection techniques.

The new developed high sensitivity techniques allowed the detection and quantification of calcium fluoride using micro-Raman spectroscopy [5]. It was shown [5] that the micro-Raman technique provides a suitable method for CaF_2 quantification. The technique has already been applied on fluoridated bovine enamel, and Raman bands due to CaF_2 or CaF_2-like material formed on/in enamel have been evidenced [5]. Advantages of this measuring technique and associated problems are described for CaF_2 determination in the presence of large amounts of hydroxyapatite. The data showed that a comparative analysis of Raman intensities of calcium fluoride and phosphate ions of hydroxyapatite could be used for quantification of CaF_2 concentrations. The intensity behavior of the CaF_2 and hydroxyapatite Raman lines was explained considering the absorption-scattering cross-sections of the two components. The ratio of the Raman intensity (322 cm^{-1}) of CaF_2 to the phosphate Raman intensity (432/447 cm^{-1}) of hydroxyapatite was found to be related linearly to the ratio of the concentration of CaF_2 to that of hydroxyapatite.

Modifications due to the acidic attack essentially concern the crystalline structure of hydroxyapatite, $Ca_{10}(PO_4)_6(OH)_2$ which represents the mineral phase in enamel and dentin. The prevention of such damages is of great importance, considering the dominant content of inorganic matter in enamel (96% as phosphates).

In previous Raman studies on teeth components mentioned above, changes in intensity of the $(PO_4)^{3-}$ band are related to the type of dentin, to its anatomical location, and to the age of the subject [6]. Significant spectral difference between coronal and root dentin were concluded by a quantitative statistical analysis [6], dentinal chemical structure and enamel-dentin junction [6-7] being under high research interest in the field.

The aim of this work is to verify the versatility of micro-Raman spectroscopy in differentiation human teeth specimens and evidencing the influence of F-treatment over the fluoride uptake by human enamel and dentin. Micro-Raman measurements were performed on F-treated milk tooth *vs.* non-F-treated milk and adult teeth, respectively.

2. Experimental

Three extracted teeth specimens from children of 5 and 6, and 31 years old adult, respectively, were acquired from the Private Stomatology Clinic "Statov", Cluj-Napoca, Romania. These teeth were collected from consenting patients who were undergoing extractions for orthodontic reasons.

The teeth were examined by one dental clinical investigator for signs of early caries at the proximal sites prior to extraction. Remaining soft tissue on extracted teeth was removed by scaling and the samples were thoroughly rinsed with water. After classical cleaning and disinfection, one of the samples was then preserved in sterile environment (medicinal alcohol- methylene blue) prior to measurement. Caries free teeth had no visible decalcification or demineralization with intact surfaces and opacity of enamel (white spots when teeth surfaces were dry). Te sample collected from the 5 years old child was subjected to F-treatment. A fresh cross section has been applied to each of them in order to investigate the dentin and enamel. These samples were used for spectroscopic measurements without further treatment.

Thin sections have been forward inspected using polarized optical microcopy with a Nikon OpricPhot 2-Pol microscope with digital camera. Additionally, a Dron 3 X-ray Difractometer (Cu anticathode) was used in order to perform the diffraction spectra of dentin and enamel, in the theta range between $5 – 50^{o}$.

FT-micro-Raman spectra have been recorded using a FT-IR Equinox 55 Bruker spectrometer with an integrated FRA-106 S Raman module, fiber optic coupled to the Raman microscope (Ramanscope II, Bruker) with a x50 Nikon objective. A Nd:YAG laser operating at 1064 nm line was used for excitation. The laser output power was set to 400 mW and 500 scans were collected for each spectrum. The detection of the Raman signal was carried out with nitrogen cooled Ge detector. The spectral resolution was 4 cm^{-1}. An attenuated total reflectance (ATR) module was used in order to record the FT-IR spectra of the enamel and dentin region of the samples without powdering them. The IR measurements were performed with less accuracy because of the encountered difficulties on achieving ATR crystal contact with the small desired region of the sample.

3. Results and discussions

As a general characteristic of the human teeth, the optical microscopy revealed the two distinct structural zones containing bioapatite. From the optical images (Fig. 1 a, b), one can observed that both dentin and enamel exhibit abundant crystalline matter.

Dentin consists of thin radial and fibrous crystallites with low birefringence generating a grayish interference color. The enamel presents shorter and thicker crystallites having similar optical properties, with a perpendicular oriented direction with respect to the dentin junction.

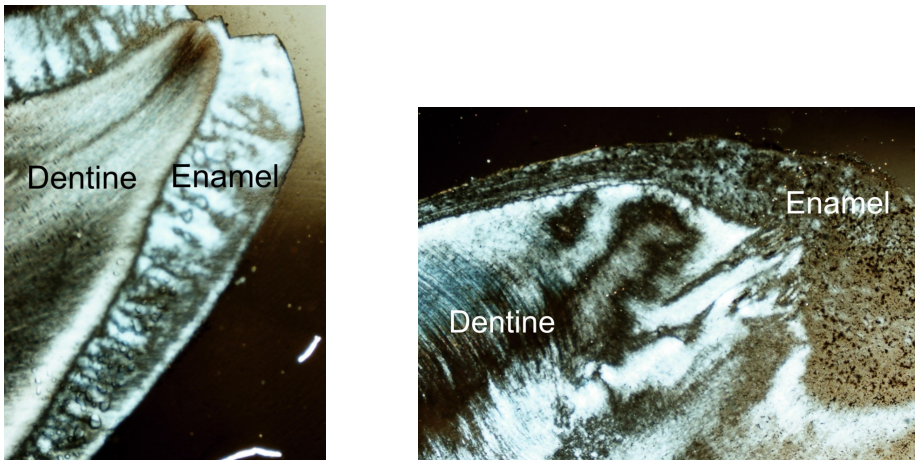

Fig. 1. Optical images of a children tooth (left) and adult molar (right) specimens, revealing the microscopy of the dentin and enamel.

Three samples were investigated, the adult non-treated tooth (**A**), the 6 years old child non-treated tooth (**C**) and 5 years old child F-treated tooth (**CF**), respectively. For all three samples, both enamel (**e**) and dentin (**d**) components were studied. FT- micro-Raman spectra of the above samples are displayed in Fig. 2, whereas Fig. 3 presents both vibrational (ATR-FT-IR, FT-Raman) spectra collected from adult enamel specimen (Ae) for a complete vibrational characterization and support in literature comparison and assignment.

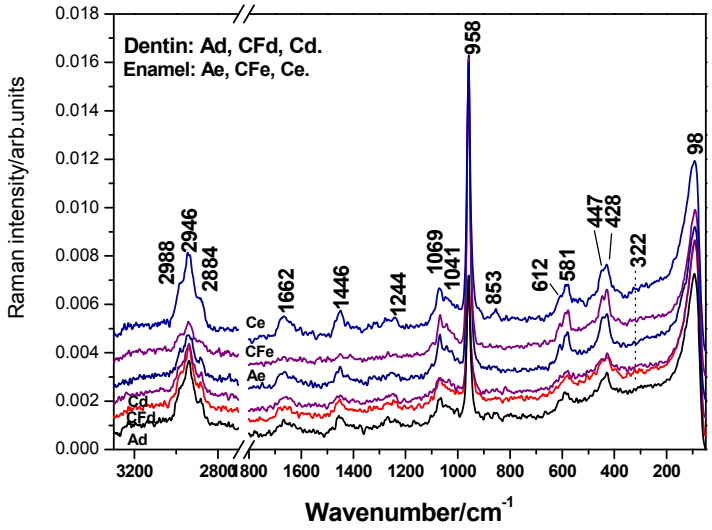

Fig. 2. Typical FT-micro-Raman spectra collected from the dentin (Ad, Cd, CFd) and enamel (Ae, Ce, CFe) teeth specimens. Excitation: 1064 nm, 400 mW.

As previously summarized [8, 9], the typical vibrational spectra of the teeth enamel are dominated by signal contributions from hydroxyapatite and proteins, the relative protein signal intensity (mostly due to collagen in the dentin) at the posterior side being higher than that of the anterior side [8]. Furthermore, the molecular components of the human tooth being reported [11, 12], the distributions of phosphate and carbonate were determined using their respective symmetric stretching vibrations, usually reported as $\nu_s(PO_4)^{3-}$ at 961 cm^{-1} and $\nu_s(CO_3)^{2-}$ at 1070 cm^{-1} [12]. Maps of the enamel-dentine junction at a high resolution of 10 μm showed that the amount of phosphate is lowest in this region. It was also shown [11] that the collagen component does not change its conformation with age. Several vibrational features arising from specific amino acid residues have been identified, especially proline and hydroxyproline, representing about 10% of the total collagen [11]. For the inorganic matrix components, quantitative estimations of carbonate content have been reported by measuring the relative intensities of the $\delta(PO_4)^{3-}$ modes at 590 and 430 cm^{-1}. A different crystalline orientation in the dental enamel and dentine hydroxyapatite components was concluded [11]. Micro-spectroscopy allowed acquisition of spatially resolved spectra, with micron scale resolution. Recently developed imaging modalities allow tissue imaging with chemical composition contrast [10-12].

The representative ATR-FT-IR spectrum collected from adult molar specimen (Fig. 3, a) exhibit prominent bands assigned to amide I, II and III from proteins at 1657, 1535 and 1236 cm^{-1}), respectively, a broad band at 2916 cm^{-1} arising from CH_3-, CH_2-stretchings, a higher and broaden band at 3270 cm^{-1} attributable to the OH-stretching, whereas the spectral pattern at 2360 cm^{-1} is due to the molecular CO_2 present along the ATR-FT-IR measurement. The phosphate ions exhibit large and complex IR stretching modes (1036, 1236, 962 cm^{-1}), whereas the bending modes region (bellow 650 cm^{-1}) is limited by the ATR system. Therefore, IR spectroscopy was less efficient for the present aim and difficult for mineral content monitoring. Noteworthy, the difficulties in obtaining spectra from dentin or enamel, due to the poor control of the crystal contact with the desired point on the sample.

The micro-Raman spectrum of adult (A) enamel (Fig. 3, b) is dominated by bands that can be unambiguously attributed [10-12] to the apatite mineral at 428, 581, 958, and 1069 cm^{-1}, together with the weaker bands attributable to the proteins from collagen (Figs. 2, 3). The presence of carbonate can be monitored following its representative modes, ν_1 at 1070 cm^{-1} (phosphate overlapped), 880 (only in samples with CO_2 content), 715, 689 (absent in our Raman spectra) and 1430-1455 cm^{-1} (overlapped with CH_2 bending modes from proteins).

In our spectra, the band at 1069 cm^{-1} is more prominent in the spectra of enamel than those of dentin and presents a complex shape, as showed above, being however, unaffected by the F-treatment. The enamel from children teeth (C and CF) studied here revealed significant similarities in band positions and relative intensities. The F-treated sample (CF) (Fig. 2) shows however prominent band intensities assigned to mineral and weaker intensities relative to proteins.

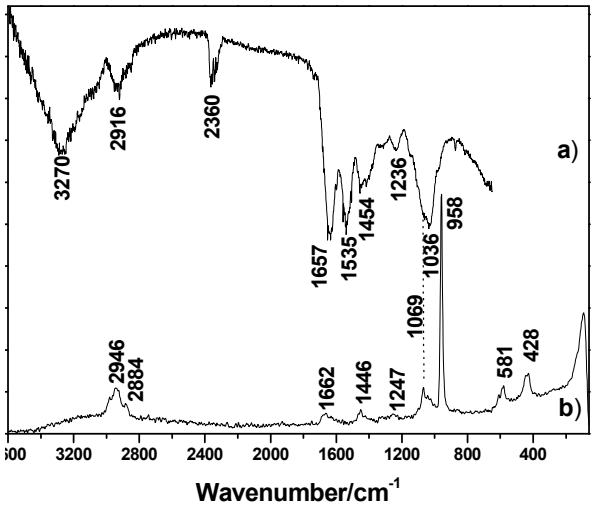

Fig. 3. ATR-FT-IR (a) and FT- micro-Raman (b) spectra of the enamel from extracted tooth (molar, adult, 38 years old). Excitation: 1064 nm, 400 mW.

As expected, the spectra collected from dentin (denoted "d" in Fig. 2) suggest the presence of much larger proportions of organic material. Again, the spectra collected from adult or children teeth revealed similar Raman spectral shape, in contrast to the previous reports, claiming spectral particularities of the phosphate modes depending on the specific characteristics of the specimen.

Previously reported Raman spectra [6] suggested that the changes in intensity of the $(PO_4)^{3-}$ marker band are linked to the type of dentin, to its anatomical location, and to the age of the subject. The variability of the dentinal chemical structure was confirmed by a quantitative statistical analysis [6], revealing a significant spectral difference between coronal and root dentin. The present reported micro-Raman spectra refer to the coronal region of adult or children teeth specimen, where the phosphate stretching mode position was unaffected either in the enamel or dentin spectra (Fig. 2). Moreover, these data are consistent with the 3D-Raman imaging of the enamel-dentin junction [15] with respect to the phosphate/C-H mode distribution [15] in human molars.

The organic matter exhibits representative Raman signal at higher wavenumbers. The C-H stretching bands between 2850 and 3000 cm^{-1} are more intense for dentin relative to those from enamel. The band shape in this region indicate multiple contributions, however, a shift tendency of the C-H stretching mode was clearly seen (Fig. 4) for the enamel (2946 cm^{-1}) compared to that the dentin (2938 cm^{-1}).

The Raman bands of amide I and III have been identified at 1670 and 1244 cm^{-1}. These bands, which correlate with those found in the FT-Raman spectra for bone, may indicate a similar protein composition in the two materials [10].

In order to monitor the balance between mineral/organic content in the studied teeth, the intensity ratio $I(PO_4)^{3-}$ / I(C-H) and $I(PO_4)^{3-}/I(CO_3)^{2-}$ modes were analyzed. The distributions of phosphate and carbonate were compared using their symmetric stretching modes, $\nu_s(PO_4)^{3-}$ at 958 cm^{-1} and $\nu_s(CO_3)^{2-}$ at 1449 cm^{-1}. The (C-O) mode at 1069 cm^{-1} previously suggested as appropriate for the carbonate content estimation [14-17], being actually a combination of the carbonate ν_1 mode at 1069 cm^{-1} with a phosphate ν_3 mode at 1076 cm^{-1}as discussed above, was not considered for this evaluation. The relative intensity ratios for the three enamel and dentin species are summarized in the Table 1.

Table 1.

Band positions and relative intensity ratios of the phosphate/C-H and phosphate/ $(CO_3)^{2-}$ stretching modes.

Specimen	$\nu(PO_4)^{3-}$ (cm^{-1})	ν(C-H) (cm^{-1})		Intensity Ratio $I(PO_4)^{3-}$ / I(C-H)		Intensity Ratio $I(PO_4)^{3-}/I(CO_3)^{2-}$	
		Enamel	Dentin	Enamel	Dentin	Enamel	Dentin
Adult (A)	**958**	**2939**	**2946**	**5.29**	**2**	**4.70**	**5.25**
Child, F-treatment (CF)	**958**	**2938**	**2940**	**10.06**	**1.75**	**4.10**	**3.33**
Child (C)	**958**	**2938**	**2944**	**2.74**	**1.96**	**2.80**	**2.90**

The highest (10.06) intensity ratio **$I(PO_4)^{3-}/I(C-H)$** has been obtained for the enamel of the fluoride treated children tooth (Table 1), whereas in the case of dentin, the two ratio values corresponding to the spectra from children teeth, are slightly different (1.75 - for F-treated, 1.96–without treatment) to suggest a small influence of the F-treatment on dentin.

The most significant variation of this ratio, between 2.74 and 10.06, was observed for the enamel, the untreated dentin of child or adult presenting comparable values. These values clearly showed that enamel had a different average composition than the adjacent hard tissues and suggest an increased mineral content upon F-treatment.

The phosphate/C-H intensity ratio for dentin exhibits comparable values for the three species, being approximately 6 times lower than that of enamel only in the case of F-treated specimen. Comparing the phosphate/carbonate intensity ratios, the CF sample presents higher values than C sample, but lower than those from adult A specimen. Particularly, the F-treated case exhibits higher phosphate/carbonate ratio in enamel, whereas the untreated species showed higher values in dentin.

The in vitro action of fluorinated treatment applied to the sample CF was expected to generate the characteristic CaF_2 Raman band [5] on enamel from children teeth. In our spectra collected from both enamel and dentin of F-treated tooth, its presence was hardly evidenced as a very weak and width band at 322 cm^{-1}, not observable in the spectra of the child untreated tooth, suggesting that the diffusive OH<—>F exchange into the expected fluorapatite was less effective. Assuming the

limits of detection and quantification of the strongest Raman band of CaF_2 at 322 cm^{-1} previously investigated by Tsuda and Arends, (1993) [5], despite its rather poor detection sensitivity of 3% or higher, CaF_2 (localized near the surface) was measurable. The micro-Raman technique was successfully applied if fluoridated enamel samples were prepared in a thin wedge shape. Surprisingly, the Raman band of CaF_2 formed by fluorapatite on/in enamel was found to exhibit a wider bandwidth than that of pure synthetic CaF_2, while the band position remained unchanged [14, 18]. It was therefore concluded that the lattice dynamics of CaF_2 formed by fluorapatite differs from that of pure CaF_2. This difference might be caused by the incorporation of $(PO_4)^{3-}$ or $(HPO_4)^{2-}$ into the CaF_2 lattice.

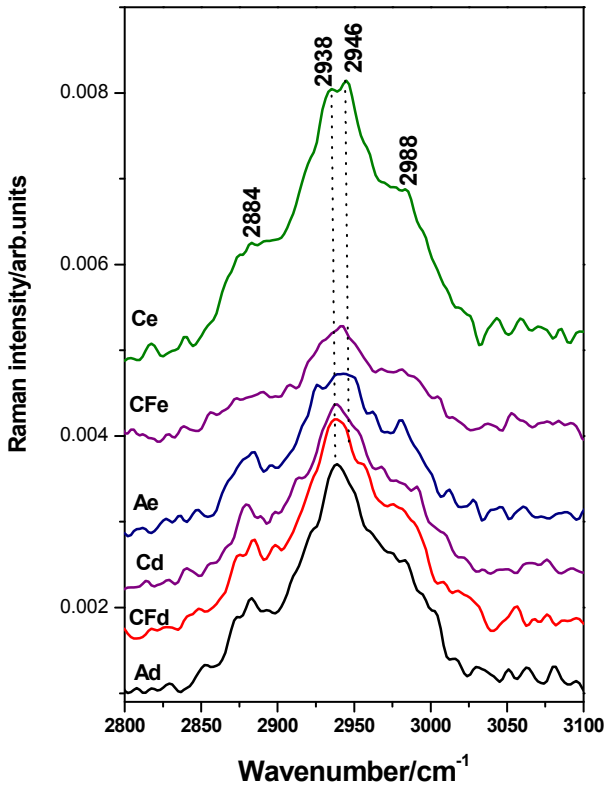

Fig. 4. High wavenumber range of the micro-Raman spectra collected from the three teeth specimens, as denoted on each spectrum; "d"referees to dentin and "e" to enamel, respectively. Excitation: 1064 nm, 400 mW.

Complementarily, the X-ray diffraction patterns (not given here) present well-defined X-ray peaks, more suitable of hydroxyapatite. The acicular grains of apatite forming aggregate of 50-100 μm are defined by the d(Å) values for dentin

at 8.185; 4.695; 3.476; 3.234, 2.842 (100); 2.222; 2.130, 2.051; 1.743 or enamel, at 4.695; 3.537, 3.129, 2.842 (100), 2.526, respectively. However, the corresponding values for the fluorapatite are close enough for rigorously differentiation of the two species.

4. Conclusions

Micro-Raman analysis has been applied in order to characterize different teeth specimens from human and to evaluate the possibility to detect the influence on the F-treatment. It was shown that the three different teeth specimens revealed the phosphate stretching Raman fingerprint at 958 cm^{-1} unaffected in position or shape, independent on the age, minerality degree of specimen or the preserving samples's factors, in both enamel and dentin. Changes in intensity of the $(PO_4)^{3-}$ bands are linked to the type of dentin, to its anatomical location, and to the age of the subject, in agreement with the previously reported results. Subtle differences between the Raman spectra of enamel and dentin from children versus adult have been also observed and linked to the inorganic/organic distribution matter.

The fluoride treatment applied to the children teeth revealed weak differences in the Raman spectra of enamel or dentin. However, the highest mineral/protein ratio was found in the fluoride treated children tooth. Therefore, the fluoride treatment monitored by micro-Raman spectroscopy could be successfully optimized within a non-invasive and high sensitivity technique applied in dentistry. A better preventive effect on enamel demineralization through reducing carbonate content in the enamel hydroxyapatite crystals and increasing crystallinity could be monitored.

REFERENCES

1. http://www.nutrition.org.uk
2. D. Fried, M. Zuerlein, J. D. B. Featherstone, W. Seka, C. Duhn and S. M. McCormack, Appl. Surf. Sci. 127-129, 852 (1998).
3. Y. H. Kwon, J.-S. Lee, Y.-H. Choi, J.-M. Lee, Photomed. and Laser Surgery, 23, 4, 389 (2005).
4. P Fattibene, A Carosi, V De Coste, A Sacchetti, A Nucara, P. Postorino, P. Dore, Phys. Med. Biol. 50 1095 (2005).
5. H. Tsuda, J. Arends, Caries Res. 27(4):249 (1993).
6. P. Tramini, B. Pelissier, J. Valcarcel, B. Bonnet, L. Maury, Caries Res. 34(3):233 (2000).
7. J. Sally. Marshall, M. Balooch, S. Habelitz, G. Balooch, R.Gallagher, G.W. Marshall, J. Eur. Ceramic Soc. 23, 2897 (2003).
8. I. R. Lewis, H. G. M. Edwards, Handbook of Raman Spectroscopy, Marcel Dekker Inc., New York, Basel, p. 563 (2001).

9. G. Socrates, Infrared and Raman Characteristic Group Frequencies, Third. Eds., John Wiley, Chichester, New York, p. 339 (2001).

10. P. Hendra, C. Jones, G. Warnes. Fourier transform Raman spectroscopy: Instrumentation and chemical applications. Ellis Horwood series in analytical chemistry. New York: Ellis Horwood; p 311 (1991).

11. M. T. Kirchner, H. G. M. Edwards, D. Lucy , A. M. Pollard, J. Raman Spectrosc., 28, 2-3, 171 (1997).

12. E. Wentrup-Byrne, C. A. Armstrong, R. S. Armstrong, B.M. Collins, J. Raman Spectrosc. 28, 2-3, 151 (1997).

13. A. Carden and M. D. Morris, J. Biomed. Opt.,5, 3, 259 (2000).

14. A. Awonusi, M. D. Morris and M. M. J. Tecklenburg, Calc. Tissue Int., 81, 1, 46 (2007).

15. K. A. Schulze, M. Balooch, G. Balooch, G. W. Marshall, S. J. Marshall, http://www.ucsf.edu/ocsci/pdf/jbmr2004karen.pdf, accesed Oc. 25, 2007, DOI: 10.1002/jbm.a.20130.

16. H. Tsuda and J. Arends, J. Dental Res., 73, 1703, (1994).

17. R. V. Santos., R. N. Clayton, Am. Min. 80, 336 (1995).

18. P. C. Ricci, A. Casu, G. De Giudici, P. Scardi and A. Anedda, Chem. Phys. Lett. 444, 1-3, 145 (2007).

STUDIA UNIVERSITATIS BABEŞ-BOLYAI, PHYSICA, LIV, 2, 2009

NEUTRON DOSIMETRY BY FISSION TRACKS METHOD

B. L. COROIAN[1] AND L. DARABAN

ABSTRACT. Nuclear tracks detectors have been applied to neutron dose determination at an isotopic neutron sources irradiation blocks. We have chosen the optimal conditions for tracks relevation in polycarbonate foils from uranium fission. The neutron doses have been theoretical calculated and experimentaly determinated.

Keywords: fission tracks, neutron dosimetry, uranium.

1. Introduction

The fission tracks method is a particulary case of the detection of elementary particles by using solid state detectors. The detector is a plastic foil of polycarbonate type in wich charged fission fragments are captured in course of neutron activation [1].

The fission fragments with a total energy of 200 MeV will be registered as particles tracks in solid state detector, producing craters in dielectric carbonate. Obvious the number of tracks in the area are proportional with the concentration of the fissionable uranium-235 from the target [2] and also with the neutron fluence at wich the sample-detector sandwich was iradiated.

Of course, the fluence determination will give information about the neutron doses. [3]

1a). The tracks production mechanism and materials

The tracks produced by ionized particles in polycarbonate foils was studied in the literature [4], identified three models for the tracks production.

The materials used as nuclear tracks detectors are: quartz, olivin, mica, phosphate-based glasses and polycarbonates such as: cellulose acetate, cellulose nitrate, cellulose triacetate.

In order to determinate the tracks densities an optical microscope coupled with digital systems will be used for automatic measurement of the number of tracks. The size of these tracks is from 25 to 50 Å to some microns length, but after a chemical treatment the dimension will be increased dramatically and will be observed with a normal optical microscope.

[1] *Babes-Bolyai University, Faculty of Physics, Kogălniceanu 1, RO – 400084 Cluj-Napoca, Romania*

1b). The relevation methodology

Mostly the latent tracks which are produced by charged particles relevated are very simple by chemical treatments. These produce a corrosion of the detector foil. The speed of decapation depends on: the type of the charged particles, composition, concentration and temperature of the corrosion solutions used.

The time t_i of chemical attack is a very important parameter and in practice will be used for obtaining a clear observed tracks. In accord with the Fig.1,[4], the parameters v_B (speed of corosion) and h_c (the depth of the tracks) time of the corrosion will be calculated with the formula $\text{ti} = \frac{h_c}{v_B}$,

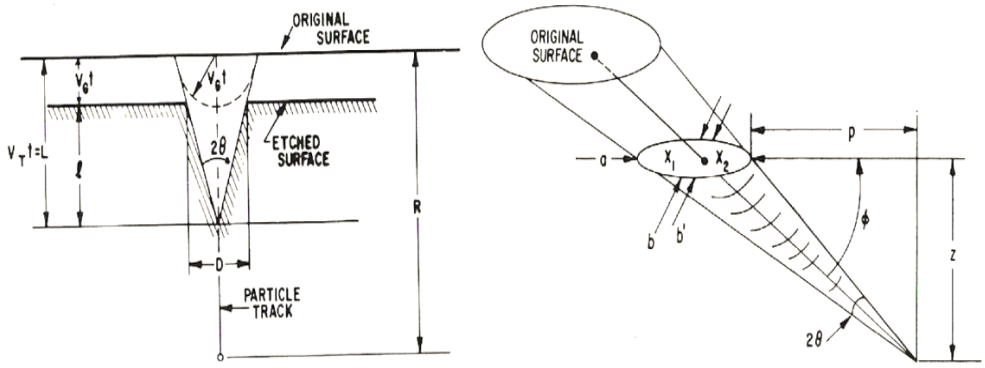

Fig. 1. Formation of the crater

The relevation solutions used for organic polymers are: KOH and NaOH water based. The chemical corrosion is produced usually in a thermostatic controled bath at 40-70˚C and a molar concentration from 2 to 6 M. The time of revelation is ussually between 2 and 6 hours at this temperature range as shown in Table nr. 1.[5]

Table nr. 1

The time of revelation at different materials and temperatures

Detector materials	Concentration of solutions, temperature and relevation time
Cellulose acetate- Triafol A	20% NaOH, 70˚C, 12 min
Cellulose nitrate	28% NaOH, 50˚C, 15 min

After corrosion the detectors will be washed with clear water and dried. The diamter of the tracks will be 50 μm at optical microscope.

Because the detector material is usually transparent, it is very easy to count the number of tracks with a normal microscope, by regulating the depth of the microscope field between 1μm up to 10-15μm and a magnification of 10x to 100x.

2. Experimental procedure

For the preparation of the technique used for fission tracks determination we have chosen thin uranium foils such as a ribbon and policarbonate foils made from cellulose triacetate received from Azomureş. We worked with transparent foils having: 98-99 μm width and a blue type foils having a width of 178-180 μm. Sandwiches made of 6 types of samples were prepared from polycarbonate and uranium foils consolidated with duct tape irradiated at neutrons.

We used a neutron source block (Fig. 2) composed by 2 isotopic neutron source: ^{241}Am-^{9}Be of 5 Ci and ^{239}Pu-^{9}Be of 33 Ci included in a paraffin moderator. In the lateral channels apear 60% thermal neutrons at a density flux of $2 \cdot 10^5$ n/s·cm^2.

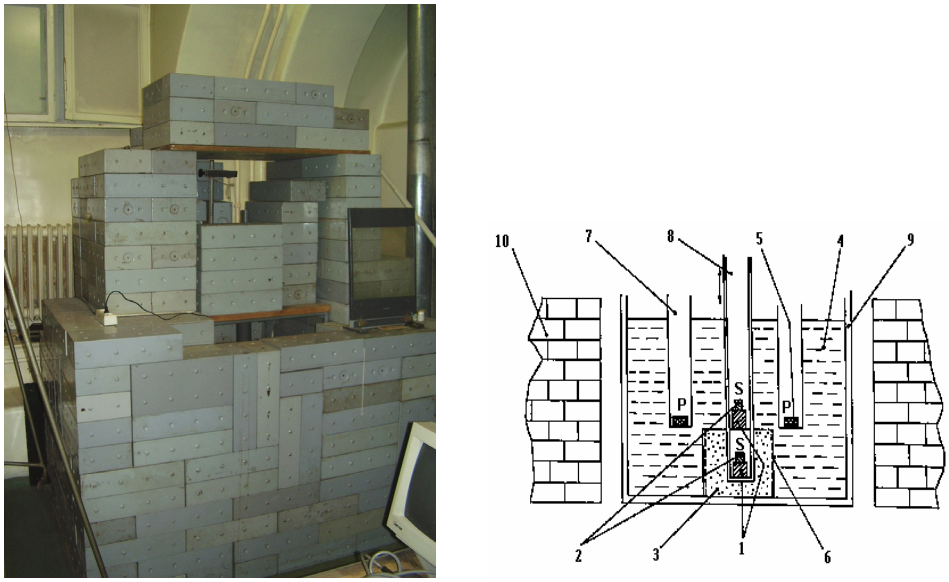

Fig. 2. The irradiation block containing the Am-Be and Pu-Be neutron sources.
1) Am-Be source, 2) Pu-Be source, 3) Borate paraffin, 4) Pure paraffin for the thermalization, 5) Sample for irradiation, 6) Cd protection, 7) Channel for irradiation, 8) Central channel for irradiation with fast neutrons, 9) Walls of paraffin moderator, 10) Borated paraffin bricks for protection.

The thermal neutrons will be capturated in the metalic uranium foil in wich ^{235}U (natural abundance 0,71%), having a capture cross section of 200 barns produce

the fission. After this process the nuclear fragments with a total energy of 200 MeV will penetrate the polyestere foil producing micro-craters during an irradiation time of 8 days due to lower thermal neutron fluence.

After irradiation the uranium sample will be extracted from the foils. After that, these foils are introduced in a NaOH 20% solution at ambient temperature of the laboratory durring 24 hours. After this relevation time the fission tracks will be observed at an optical microscope.

3. Results

We used an optical microscope, model Premiere, having 4 obiective with a magnification of: 4x, 10x, 40x and a magnification of 100x (with silicon oil).

A representative image of these fission tracks is illustrated in Fig. 3.

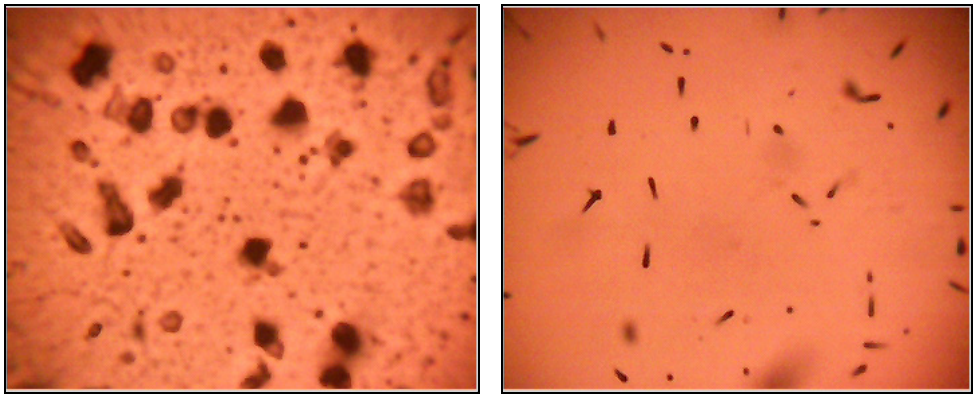

Fig. 3. Fission tracks seen on foils at different magnification

In all images we observed nuclear tracks as conical craters. The number of these tracks are proportional with thermal neutron doses.

4. The estimation of neutron doses

In order to estimate the dose inner irradiation channels we adopte a method illustrated in literature[6]:

The radiation dose absorbed by the foils is estimated by the method which consider the irradiation effects on human body due to neutron capture in nitrogen atoms by nuclear reaction $^{14}N(n,p)^{14}C$.

The dose fluence has been calculated with the formula:

$$d\left(\frac{rad}{s}\right) = \frac{1}{100} N_N o_N \Phi' Q = 22.9 \frac{\mu Sv}{h} \quad (1)$$

where $N_N = 1.3 \cdot 10^{21} \frac{nucleus}{cm^3}$, σ_N = 1,8 barns, Q = 0,56 MeV, and the neutron flux inner the irradiation channel has been determined by:

$$\Phi = \frac{S_n}{4\pi r^2} = 2.1 \cdot 10^5 \, n/s \cdot cm^2 \tag{2}$$

in which the fluence is S_n = 6,6·10^7 n/s and r = 5 cm. Because only 60% from the total neutron flux is thermally, results: $\Phi' = 1,2 \cdot 10^5$ n/s·cm^2.

After this calculations and at an irradition time of 192 hours we deduced a dose of 4396 μSv or 439.6 mrem, knowing that the professional dose admited in Romania is 100 mrem/week.

If N_1 is the number of nuclear tracks counted by us on microscop ocular coresponding to a dose of D_1= 4396 μSv, and N_2 is the number of tracks from the other foil for an unknown doses D_2, this will be calculated with the formula above:

$$\frac{N_1}{N_2} = \frac{D_1}{D_2} \tag{3}$$

The errors were deduced from many countings with the formula :

$$\sigma = \sqrt{\frac{\sum_{i=1}^{N} \left(N_i - \overline{N}\right)^2}{n(n-1)}} \tag{4}$$

where: n - the number of countings;

N_i – the number of tracks/ocular;

$\overline{N}$ - the average value of the numbers of tracks.

The result will be done as $\overline{N} \pm \sigma$ or relative error: $\varepsilon = \frac{\sigma}{\overline{N}}$.

In this mode we obtained the unknown dose D_2.

5. Conclusions

For neutron dose measurements this method is useful to determine the doses in small spaces of the installation comparable with electronic dosimeters. It is a simple and precise method for neutron dose measurement.

Also this method is applied to dose determination in Bohr Neutron Capture Therapy (BNCT) [7] in nuclear medicine for dose estimation at neutron irradiation facilities. In geophysics this method is very useful for uranium determination in rocks.

REFERENCES

[1] Ana Daniş, D. Dociorman, *Metoda urmelor de fisiune-metoda fizică de analiză a elementelor fisionabile (U,Th)*, Partea 1. Descrierea metodei, domenii de aplicabilitate, St. Cerc. Fiz., 39,4, 1987.

[2] S.R. Hashemi-Nezhada, I.V. Zhukb, A.S. Potapenkob, M.I. Krivopustovc, W. Westmeierd, R. Brandtd, *Determination of uranium fission rate in an arbitrary neutron field using fission track detectors,* Radiation Measurements 43, S204–S209, 2008.

[3] N. M. Borisov, O. A. Kochetkov,V. N. Yatsenko, D. Franck,L. de Carlan, S. Ts. Tsédish; *Modern internal – irradiation dosimetry*; Atomic Energy, Vol. 97, No. 4, 2004.

[4] R.L. Fleischer, B.P. Price, R.M. Walker, *Nuclear Tracks in Solids*, University of California Press, Bearkeley, 51-60, 1975.

[5] G. Somogyi, I. Hunyadi, *Etching properties of CR-39 plymeric nuclear track detector*, Pergamon Press, Oxford, 443-452, 1980.

[6] Al. Berinde, M. Grecescu, E. Ionescu, G. Ionescu, D. Iorcacge, I. Luchian, S. Meitert, Al. Ştefănescu, *Probleme rezolvate de tehnică nucleară*, Ed. Tehnică, Bucureşti, pp. 345-352, 1975.

[7] T. Yamamoto, K. Nakai, T. Tsurubuchi, M. Matsuda, M. Shirakawa, A. Zaboronok, K. Endo, A. Matsumura, *Boron neutron capture therapy for newly diagnosed glioblastoma: Apilot study in Tsukuba*; Applied Radiation and Isotopes 67, S25–S26, 2009.

STUDIA UNIVERSITATIS BABEŞ-BOLYAI, PHYSICA, LIV, 2, 2009

INTERACTIONS OF EIT WAVES WITH GRAVITATIONALLY STRATIFIED CORONAL LOOPS

G. MOCANU[1], B. ORZA, A. MARCU

ABSTRACT. In this paper we studied the effect of interactions of EIT waves (global waves observed in the solar corona in the extreme ultraviolet band filter) with gravitationally stratified coronal loops, considering a particular analytical form for the density variation along the loop. We investigated how the transverse and longitudinal generated oscillations depend on the nature of the EIT wave and the parameters characterizing the coronal loop.

The coronal loop was approximated with a straight magnetic flux tube with fixed ends and the EIT wave with a pulse in space. The medium inside the magnetic flux tube was described by a cosecant profile of the density. The basic mathematical tool used was linear MHD.

Both analytical and graphical results show a strong connection between EIT periods and normal modes of oscillations of the flux tube. HeunC functions appear as ingredients for describing both the longitudinal and transversal oscillations. The amplitudes of these oscillations depend both on the energy of the incident wave as well as on the gravitational constant.

***Key words**:* EIT waves, MHD equations, coronal loops.

1. Introduction

Multi-satellite observations (SOHO, TRACE/EUVI, STEREO/EUVI) of the solar atmosphere showed the presence of oscillations and waves in the coronal structures due to the interactions between EIT waves and coronal loops.

Present theoretical models used to describe this kind of interactions take into consideration some assumptions: the coronal loop can be approximated to a straight magnetic flux tube, embedded in a magnetic-free isothermal environment; the plasma inside the flux tube is in thermal equilibrium with its surroundings and the presence of a background flow [1].

One of the most important problems for the mathematical model is how to simulate the interactions between coronal loops and the external driver, to obtain observed oscillatory patterns. Musielak and Ulmschneider (2003) [2], using a pulse driver to shake the base of the stratified loops, obtained that the longitudinal modes will decay in time as $t^{3/2}$. Ballai et al (2008) [3] focused on the connection between

[1] *Department of Theoretical and Computational Physics, Babes-Bolyai University, Cluj Napoca, Romania*

the normal period of the loop and the period of the EIT wave in the presence of gravity, but considered a constant density. They obtained that in the case of a pulse driver the resulting signal will not have a well defined standing mode pattern. In this case oscillations are found to be a superposition of modes.

The paper is organized as follows: in the next section we introduce the fundamental equations and discuss the main assumptions. Section 3 is devoted to numerical results and conclusions and finally we point out a few future analytical approaches of the phenomena.

2. Model and basic equations

Our proposed 2D working model is shown in Figure 1. The flux tube is in thermal equilibrium with its surrounding atmosphere which is field free and which exhibits the longest time scale in the model, such that $\partial p_e / \partial t = 0$.

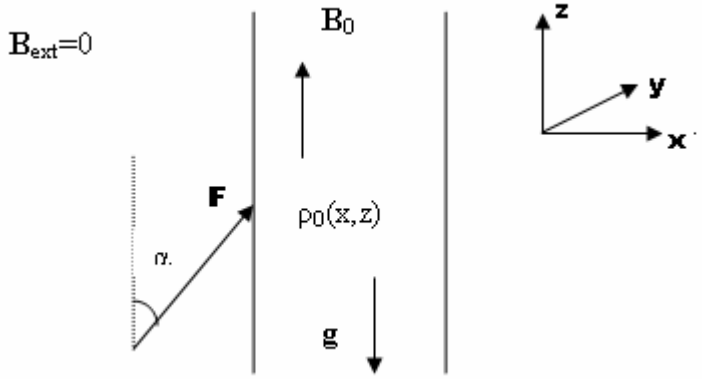

Figure 1. Basic model

An important characteristic of the model is the density profile, chosen so that it fits the observational data: higher density in the chromosphere and in the lower corona and decreasing density towards the apex of the loop:

$$\rho_0(z) = \rho_0(0)\csc^{-4}\left(\frac{z}{L}\right). \tag{1}$$

Other authors have chosen different density profiles such as exponential decay with height (most used in literature) [5], variation of density due to an inhomogeneity parameter [6], or considered the length scale of the studied phenomena small enough to have constant density. However, in studying the full effects of macroscopic interaction of the loops with EIT waves, typical dimensions of loops are larger than coronal length scales and taking into account gravity and variation of density is crucial.

The action of EIT waves is modeled as a pulse in position and periodical in time. We will focus in obtaining an analytical form for the parallel and transverse amplitude of the propagating disturbances. For the mathematical analysis, consider all physical quantities describing the loop written as $f(x,z,t) = f_0(z) + \widetilde{f}(x,z,t)$, with the exception of $v_0 = 0$ and $B_0 = const.$, where the $\widetilde{f}$ s represent the perturbations following the impact with the EIT wave. The fundamental equations used are ideal MHD in a linear approximation:

$$\frac{\partial \widetilde{\rho}}{\partial t} + \rho_0 \frac{\partial \widetilde{v}_\perp}{\partial x} + \rho_0 \frac{\partial \widetilde{v}_\parallel}{\partial x} + \widetilde{v}_\parallel \frac{d\rho_0}{dz} = 0, \tag{2}$$

$$\rho_0 \frac{\partial \widetilde{v}_\parallel}{\partial t} = -\frac{\partial \widetilde{p}}{\partial x} + F_{EIT} \sin\alpha + \frac{1}{\mu} B_0 \left(\frac{\partial \widetilde{b}_\perp}{\partial z} - \frac{\partial \widetilde{b}_\parallel}{\partial x} \right), \tag{3}$$

$$\rho_0 \frac{\partial \widetilde{v}_\perp}{\partial t} = -\widetilde{\rho} g - \frac{\partial \widetilde{p}}{\partial z} + F_{EIT} \cos\alpha, \tag{4}$$

$$\frac{\partial \widetilde{b}_\perp}{\partial t} = B_0 \frac{\partial \widetilde{v}_\perp}{\partial z}, \tag{5}$$

$$\frac{\partial \widetilde{b}_\parallel}{\partial t} = -B_0 \frac{\partial \widetilde{v}_\perp}{\partial x}, \tag{6}$$

$$\frac{\partial \widetilde{p}}{\partial t} = c_s^2 \frac{\partial \widetilde{\rho}}{\partial t}, \tag{7}$$

$$\frac{\partial \widetilde{b}_\perp}{\partial x} + \frac{\partial \widetilde{b}_\parallel}{\partial z} = 0, \tag{8}$$

the horizontal pressure equilibrium in the unperturbed medium $p_0 + B_0^2/(2\mu) = p_e$ and in the perturbed medium $\widetilde{p} + B_0 \widetilde{b}_\parallel / \mu = p_e$.

After equating out all perturbed quantities except the velocities, we employ Fourier analysis by taking:

$$\widetilde{v}_\perp = e^{i\omega t} \hat{v}_\perp(z), \tag{9}$$

$$\widetilde{v}_\parallel = e^{i\omega t} \hat{v}_\parallel(z), \tag{10}$$

$$F_{EIT} = \hat{F}_{EIT}(z) e^{i\omega_{EIT} t}. \tag{11}$$

Observational data of EIT waves indicate that the spatial part of the force it exerts on the loop should be modeled as a pulse, so we considered [3]:

$$\hat{F}_{EIT}(z) = E_{EIT} \lambda_e \frac{\delta(z - z_0) e^{-\lambda z}}{\rho_0(z)}, \tag{12}$$

where E_{EIT} is the energy of the EIT wave, estimated at $10^{16} - 10^{19} J$ [3] and λ_e and λ are constants characteristic for the loop and its coupling to the external medium, in terms of sound and Alfven speeds.

Using (9-11) and solving equations (2-8) for $\hat{v}_{\parallel}$ and $\hat{v}_{\perp}$ leads to interesting analytical results. Both amplitudes are equal to linear superposition (with different coefficients) of HeunC functions modulated by sinusoids with argument $t(\omega_{EIT} - \omega)$ and multiplied by the energy of the EIT wave. The component of the velocity parallel to the equilibrium magnetic field also has the particular feature of being dependant on the gravitational constant.

These results give an analytical expression for computing transversal displacements in coronal loops due to the impact of EIT waves as a function of the impact point, z_0, angle of impact, α, normal mode vibration frequency of the loop, ω and the frequency of the EIT wave, ω_{EIT}. Also, they quantify the energy transfer between different degrees of freedom of the plasma inside the flux tube.

3. Results and conclusions

In our numerical simulation we considered the length of the loop $200 Mm$ and that the apex of the loop ($z_0 = L/2$) is the point of perpendicular energy transfer between the EIT wave ($10^{17} J$) and the loop. We studied the effect of this energy transfer on the amplitudes of loop perturbations. This was done by plotting the transversal and parallel velocity amplitudes as a function of ω with ω_{EIT} as a parameter (Figure 2).

The transversal velocity decreases with the decrease of the EIT wave frequency. The behavior of the longitudinal mode indicates a resonance on the same intervals $\Delta\omega$ and $\Delta\omega_{EIT}$. The rescaled representation of the transversal velocity (Figure 3) shows that, although different values of ω_{EIT} lead to different numerical values for the amplitude of the velocity, the behavior of the transversal movement does not change.

It is shown that the presence of gravity and longitudinal stratification changes the results obtained for a homogeneous loop, which has resonances in well defined, small intervals. Our model shows that displacements in transversal direction have a global maximum in the same interval, but present two other well defined local maxima. This means that the transfer of energy from the EIT wave to the loop can be realized for two additional configurations of the loop, although at decreased efficiency. This is not surprising, since the frequency of normal modes depends on the intrinsic characteristics of the flux tube, and changing these characteristics to allow for a more accurate representation of observed data will also change the way the coronal loop interacts with external factors in the corona, such as an incoming EIT wave.

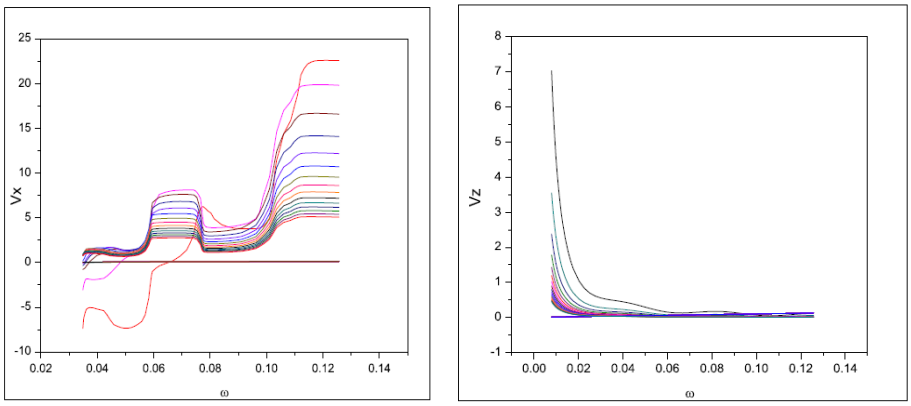

Figure 2. a)Velocity amplitude in the perpendicular direction.
b) Velocity amplitude in the parallel direction

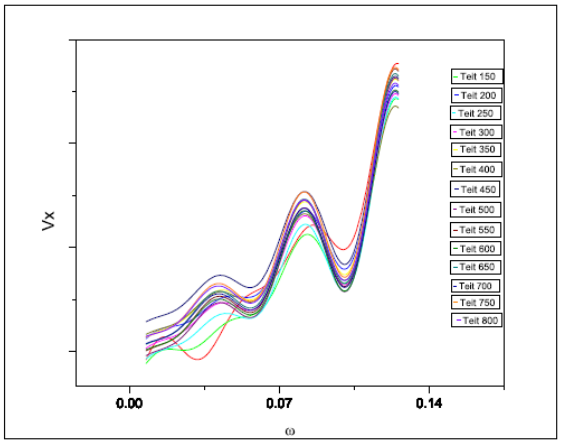

Figure 3. Re-scaled velocity amplitude in the perpendicular direction

4. Future work

Keeping in mind that the underlying physics of the phenomenon is complex and has features that we are unable to account for analytically (e.g. the nature of the EIT waves is still unknown), further steps can be made to bring the model closer to reality. Including dissipative mechanisms might give a reason for the observed damping following the impact and external magnetic field will lead to a higher degree of coupling between the loop and its external medium. A realistic model will also have to include the elasticity of the tube and its curvature at the apex.

Acknowledgements

The authors acknowledge the financial support by the Romanian National University Research Council (CNCSIS-PN-II/531/2007).

REFERENCES

1. R. Erdelyi, J. Hargreaves, A&A, 483, 285-295, (2008)
2. Z.E. Musielak, P. Ulmschneider, A&A 400, 1057 (2003)
3. I. Ballai, M. Douglas, A. Marcu, A&A, 488 , 1125, (2008)
4. M.J. Aschwanden "Physics of the Solar Corona", Springer Praxis Books, Subseries "Astronomy and Planetary Science", (2006)
5. A.J. Diaz, G.R. Donnelly, B. Roberts, A&A, 476, 359-368 (2007)
6. M. Gruszecki, K. Murawski, A&A, 478, 717G (2008)
7. I. Ballai, R. Erdelyi, J. Hargreaves, Physics of plasmas, 13, 042108, (2006)

STUDIA UNIVERSITATIS BABEŞ-BOLYAI, PHYSICA, LIV, 2, 2009

EFFECT OF TiO_2 NANOPARTICLES ON STRUCTURE AND MORPHOLOGY OF Zn ANTICORROSIVE COATINGS

A.V. POP[1*], C. BULEA[2], B. DAVID[1], DORINA CIOMOS[1] AND LIANA MURESAN[3]

ABSTRACT. Zn-TiO_2 nanocomposite coatings were obtained by electrolytic co-deposition of zinc with TiO_2 nanoparticles, on steel substrate. Morphological (atomic force microscopy-AFM), chemical composition (by using EDAX) and structural analysis (X-ray diffraction -XRD) of the coatings was carried out. The influence of TiO_2 nanoparticles concentration in the plating bath on structure, phase content and morphology is discussed in relation with the corrosion resistance.

***Keywords*:** Zn-TiO_2 composite coatings, AFM, XRD, corrosion

1. Introduction

Nanostructured materials have gained importance in recent years due to their significantly enhanced properties [1]. A novel method of transforming a material to a metastable state is to reduce its grain size to a few nanometers, at which the proportion of atoms in the grain boundaries is equivalent to or higher than those inside the grains. Nanostructured coatings offer great potential for various applications due to their superior characteristics that are not typically found in conventional coatings.

The fact that electrochemical deposition, also being an atomic deposition process, can be used to synthesize nanocomposites, has generated a great deal of interest in recent years. The final size distribution of the electrodeposited material, however, strongly depends on the kinetics of the nucleation and growth.

The process for anticorrosive protecting steel materials is generating good zinc composite coating on its surface.

In order to make the composite coatings still more corrosion resistance and possessed better tribological properties, nowadays there is growing interest in the co-deposition of the nanoparticles because of their increasing availability. Among the nanomaterials, the TiO2 is in great demand for the generation of composite coating on steel with other metals and alloys. The TiO2 nano-materials are co-deposited

[1] *Department of Physics, "Babes-Bolyai" University, 400084 Cluj-Napoca, Romania*
** E-Mail: avpop@phys.ubbcluj.ro*
[2] *BETAK S.A., Str. Industriilor, 4 Bistriţa, Romania*
[3] *Department of Physical Chemistry, "Babes-Bolyai" University, 400028 Cluj-Napoca, Romania*

successfully with Ni, Cu, Ag and Zn metal [2-4]. Zinc composites containing occluded TiO_2 particles offer an interesting solution to this problem, due to their improved corrosion and wear resistance, increased hardness and better tribologic properties as compared to pure zinc coatings [5].

The electrolytic codeposition of zinc with TiO_2 particles by using micron or submicron size particles suspended in a classical zinc electroplating bath has been already reported [6-8]. A lot of parameters, such as current profile, bath composition, pH, particle concentration, temperature, stirring rate, presence of additives strongly influence the properties of the resulting composite coatings [9]. Due to the complexity of the process, there are still many unknown aspects to be considered.

The aim of this work is to investigate the influence of TiO_2 nanoparticles concentration on the properties of Zn-TiO_2 composite films plated on steel substrate, by using X ray diffraction and atomic force microscopy methods.

2. Experimental

TiO_2 nanoparticles (Degussa, D, 99,5%, 21 nm) were suspended in an aqueous electrolyte containing 75 g/l $ZnCl_2$, 230 g/l KCl, 20 g/l H_3BO_3 and brightening agents. The concentration of TiO_2 nanoparticles in the plating bath was 3 g/l, 5g/l and 10 g/l, respectively.

For corrosion tests a solution of 0.2 g/l $(NH_4)_2SO_4$ (Riedel –de Haën, Germany) (pH 3) was used. All other reagents were analytical grade and used as received. The corrrosion measurements (open circuit potential and polarization curves) were performed with a potentiostat Autolab-PGSTAT 10, (Eco Chemie BV, Utrecht, Netherlands). Open-circuit potential (*ocp*) measurements were carried out as a function of time, during 1 hour. Anodic and cathodic polarization curves were recorded in a potential range of $E = E_{corr} \pm 200$ mV for kinetic parameters determination and in a potential range of $E = E_{corr} \pm 20$ mV for polarization resistance determination, with a scan rate of 0.25 mV s^{-1}. The corrosion behavior of the composite coatings depends both on the concentration and on the nature of the TiO_2 nanoparticles.

The microstructures of the as-electrodeposited Zn-TiO_2 nanocomposite films were analyzed by atomic force microscope(AFM). The chemical composition of the Zn-TiO_2 nanocomposite films was determined using an EDAX NEW XL30 X-ray dispersive energy analyzer attached to the Philips XL-30 scanning electron microscopy (SEM). The phases present in the deposits and the preferred orientation of the deposits were determined by X-ray diffraction (XRD) analysis, using a Brucker X-ray diffractometer with a Cu K_α (λ = 0,15406 nm) at 45 kV and 40 mA. The 2θ range of 20–100º was recorded at the rate of 0.02º and 2θ /0.5 s. The crystal phases were identified comparing the 2θ values and intensities of reflections on X-ray diffractograms with JCP data base using a Diffrac AT-Brucker program.

3. Results and discussions

In the investigated experimental conditions, the highest corrosion resistance was observed in the case of the composite coatings obtained from electrolytes containing 5 g/l TiO_2 , [10,11].

The X-ray diffractograms of Zn-TiO_2 nanocomposite for TiO_2 nanoparticles in the plating bath was 0 g/l (sample 0), 5g/l (sample 5) and 10 g/l (sample 10), respectively are shown in Fig. 1. The diffraction pattern of zinc phase and the substrate (iron) are present in all investigated nanocomposite.

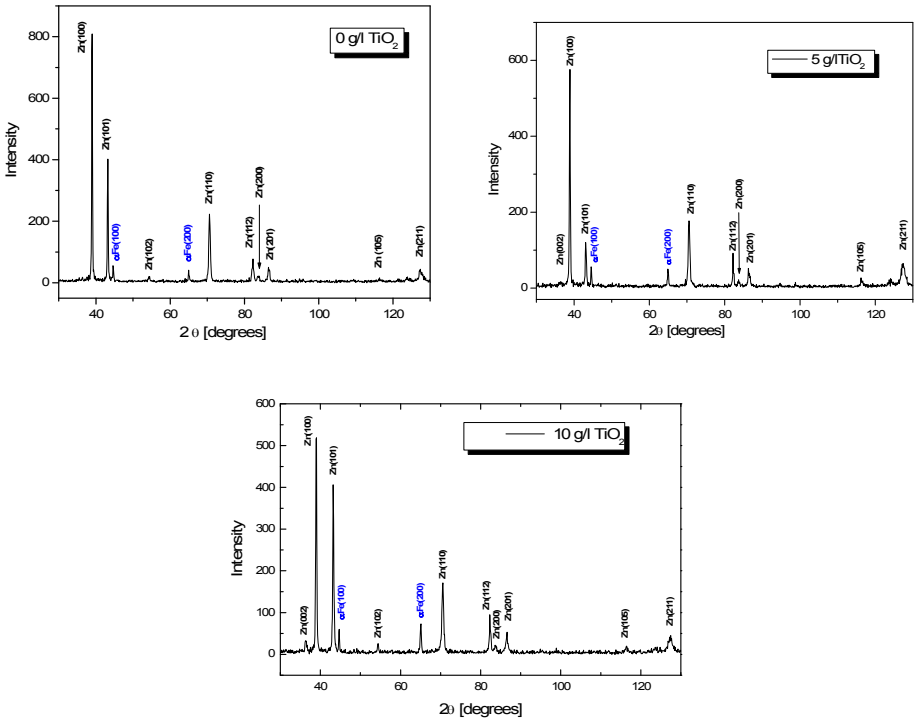

Figure 1. XRD for Zn-TiO_2 nanocomposite for TiO_2 nanoparticles in the plating bath was 0 g/l, 5g/l and 10 g/l.

In all samples the diffraction pattern attributed TiO_2 are absent.By increasing TiO_2 concentration, the intensity of some peaks in diffraction pattern of Zn changes.

The diffraction pattern of zinc phase and the substrate (iron) are present in all investigated nanocomposite. In all samples the diffraction pattern attributed TiO_2 are absent. By increasing TiO_2 concentration, the intensity of some peaks in diffraction pattern of Zn changes.

When TiO_2 concentration increases from 0g/l to 5g/l, the intensity peak (101) of Zn decrease and the intensity of peak (100) increase. In sample 10 (10g/l), the intensity of (101) peak increase and become comparable with intensity of peak (110). These observed textural modifications of composite coatings in Figure 1 are associated with specific structural modifications of Zn crystallites provoked by the adsorption - desorption phenomena occurring on the metal surface [12], induced by the presence of TiO_2 nanoparticles.

Crystallite size was performed by measuring the broadening of a particular peak in a diffraction pattern associated with a particular planar reflection from within the crystal unit cell. It is inversely related to the FWHM (full width at half maximum) of an individual peak - the more narrow the peak, the larger the crystallite size [13-15].

If the crystals are randomly arranged or have low degrees of periodicity, the result is a broader peak. To measure the crystallite size, the diffraction peak (110) of Zn was collected. A background is applied and the peak is profile fit to measure the area under the curve and the FWHM. All the crystallite size calculations are determined using the Scherrer equation once the corrected (instrumental broadening) FWHM is known [10]:

$$D = \frac{0,9\lambda}{B\cos\theta}$$

where, D is the grain size [nm], $\lambda = \lambda_{CuK\alpha 1} = 0,15406$ nm), B este linewidth, θ is the position for (110) reflection. The linewidth is $B = B_m - B_e$ where B_m is the measured linewidth and $B_e = 0,063^o$ is the correction of FWHM.

Figure 2 show that the profile of (110) reflection and is described by Lorentz behavior.

Table 1 show the experimental parameters used to obtain the grain size The calculated value for D show that the increase of TiO_2 concentration lead to the decrease of grain size.

Table 1

Sample	B_m [degrees]	Θ [degrees]	B [rad]	D[nm]
0g/l	0,40147	35,306	0,00591	**28,70**
5g/l	0,46474	35,266	0,00701	**24,20**
10g/l	0,46824	35,274	0,00707	**24**

Localized EDAX analysis carried out on the coating cross sections indicated that there is no significant difference in the chemical composition of studied samples (Table 2). The results in Table 1 show that along the cross section, there is no presence of Ti atoms. In order to emphasize if Ti or TiO_2 nanoparticles are distributed over the surfaces, Phase Imaging-AFM was recorded.

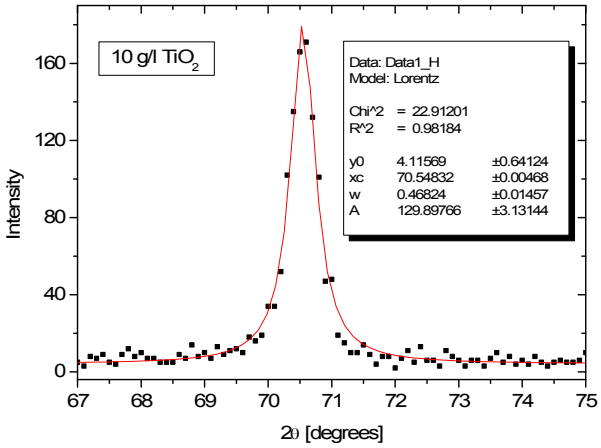

Figure 2. The profile of (110) peak of Zn film. The smooth curve show the Lorentz fit of data.

Table 2

Element	O	Cl	K	Ti	Fe	Zn
Weight%	3.78	0.35	0.08	0.00	2.76	93.02
Atomic%	13.75	0.57	0.13	0.00	2.88	82.68

Phase Imaging, an extension of Tapping Mode Atomic Force Microscopy (AFM), is a powerful tool for mapping variations in the sample's properties at very high resolution, especially for characterizing the components of composite materials. By mapping the phase of the cantilever oscillation during the Tapping Mode scan, phase imaging goes beyond simple topographical mapping by detecting variations in composition, and perhaps other properties.

Figure 3 shows the phase imaging for samples 0, 5 and 10. It is obvious that there is a variation of chemical distribution of phases on the surface of samples 5 and 10, as a function of TiO_2 nanoparticles concentration. The small dots uniform distributed on the surface of sample 5, and the darker elongated islands on the surface of sample 10 may be attributed to nanoparticles. Supplementary, on the surface of 10 sample, the darker elongated islands may be due to nanoparticles agglomeration, and the lighter islands parts suggest an additional phase. It is obvious that sample 5 has a better surface chemical homogeneity than sample 10.

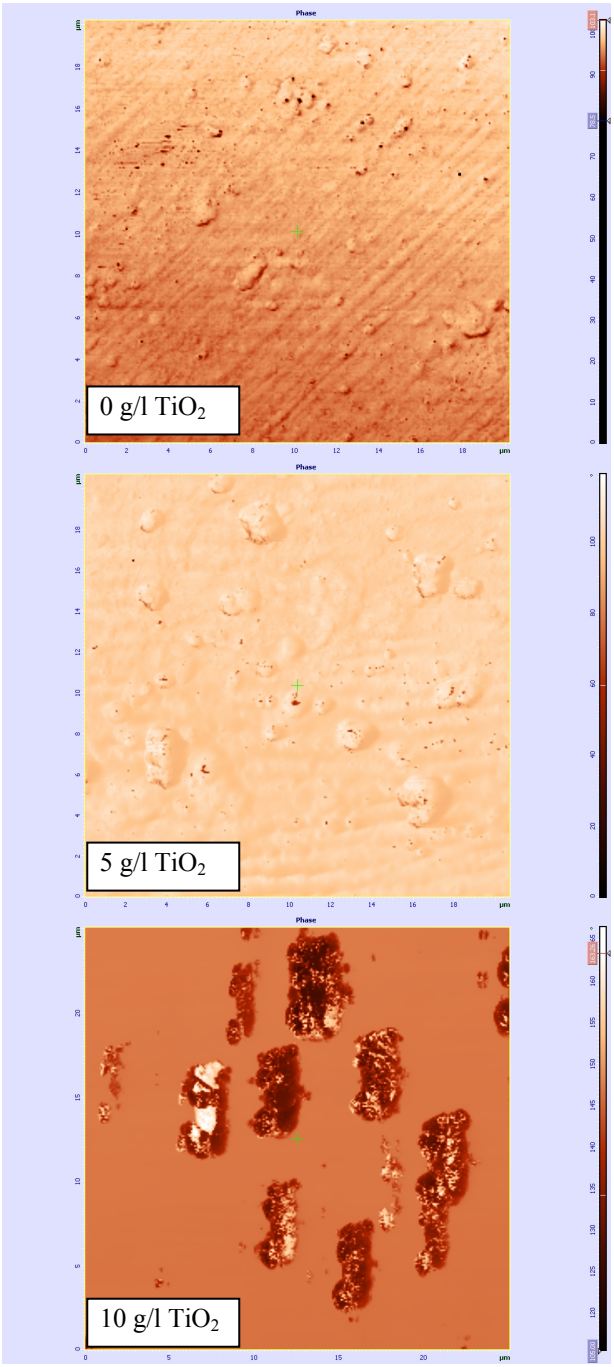

Figure 3. AFM phase imaging for samples: 0 g/l TiO2, 5 g/l TiO_2 and 10 g/l TiO_2.

Morphological observation of the coating nanocomposite was also carried out by AFM analyses. Figure 4 show a three-dimensional image for samples 5 and 10. These images suggest that that the TiO2 concentration lead to changes in morphologies present on sample 5 and sample 10 surfaces. The surface of film 5 is more uniform that for film 10.

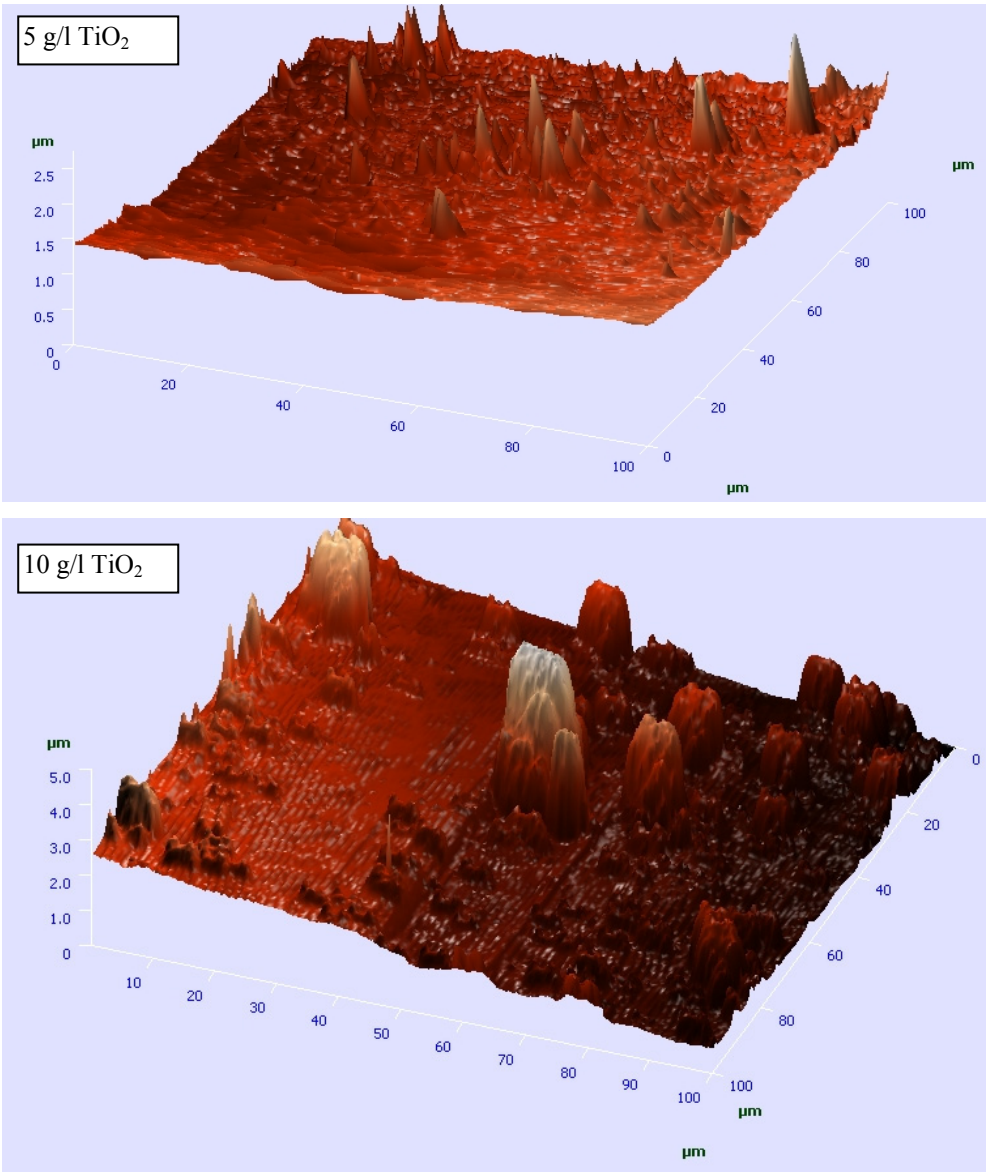

Figure 4. A three-dimensional image for samples: 5 g/l TiO_2 and 10 g/l TiO_2.

4. Conclusions

(i) The corrosion behavior of the composite coatings depends on the concentration of the TiO_2 nanoparticles. The optimum concentration of TiO_2 for anticorrosion properties of composite coatings is 5g/l, [10,11].

(ii) XRD shows only reflections from Zn film and substrate (steel).The absence of TiO_2 reflections suggest a concentration below the sensibility of XRD system.

(iii) The increase of TiO_2 concentration in electrolite solution up to 5g/l lead to change of the preferential orientation from (100) to (101) and to the decrease of grain size.

(iv) AFM phase imaging show a different distribution on coating surface of TiO_2 nanoparticle clusters. The better chemical and morphological homogeneity for nanocomposite coating obtained for 5g/l TiO_2.

Acknowledgments

The authors gratefully acknowledge the financial support from project NANOTECH 97/28.09.2007.

REFERENCES

[1] 1. Injeti Gurrappa1 and Leo Binder,Sci. Technol. Adv. Mater. **9,** 043001(2008).

[2] S. Ito, T. Deguchi, K. Imai, M. Iwasaki, H. Tada, Electrochem. Solid State Lett. **2**, 440(1999).

[3] N.R. De Tacconi, A.A. Boyles, K. Rajeshwar, Langmuir **16**, 5665 (2000).

[4] T. Deguchi, K. Imai, H. Matsui, M. Iwasaki, H. Tada, S. Ito, J. Mater. Sci. **36**, 4723(2001).

[5] T.T. Tuaweri, G.D. Wilcox, Surface Coat. Technol. **200**, 5921 (2006).

[6] P.B. Mokshanatha, V.T.Venkatarangaiah, N.Y. Arthoba, P. Kalappa, Synthesis and Reactivity in Inorganic, Metal-Organic and Nano-Metal Chemistry **37** (6), 461 (2007).

[7] L. Muresan, M. Gherman, I. Zamblau, S. Varvara, C. Bulea, Studia Universitatis Babes-Bolyai, Chemia, LII, 3, 97 (2007).

[8] T. Deguchi, K. Imai, H. Matsui, M. Iwasaki, H. Tada, S. Ito, J. Mat. Sci**. 36**, 4723 (2001).

[9] C.T.J. Low, R.G.A. Wills, F.C. Walsh, Surface Coat. Technol. **201**, 371 (2006).

[10] A.V. Pop, Adriana Vlasa, Simona Varvara, B. David, C. Bulea and Liana Muresan, JOAM-RC 12, (2009) - in press.

[11] Adriana Vlasa, Simona Varvara, Liana Muresan, Corrosion and Anicorosive Protection, vol. IV, no. 3, 33-39 (2009).

[12] J. Amblard, M. Froment, N. Spyrellis, Surf. Technol. **5** (1977) 205.

[13] H. P. Klug and L. E. Alexander, *X-ray Diffraction Procedures*, 2nd edition (John Wiley, New York, 1974).

[14] D. Balzar, *J. Appl. Cryst.* **25** (1992) 559-570.

[15] Th. Kehagias, Ph. Komninou, G. Nouet, P. Ruterana, and Th. Karakostas,Phys. Rev. B **64**, 195329 (2001).

STUDIA UNIVERSITATIS BABEŞ-BOLYAI, PHYSICA, LIV, 2, 2009

CALCULATED TOTALLY DIFFERENTIAL CROSS SECTIONS FOR THE IONIZATION OF HELIUM BY ELECTRON IMPACT

A. TÓTH[1], I. TÓTH, L. NAGY

ABSTRACT. Totally differential ionization cross sections for the helium in impact with electron projectiles have been calculated. The distorted-wave Born approximation was applied, which is suitable for moderate velocity electron projectiles. Results are presented in the scattering plane, and are compared to the experimental data. Both the binary and recoil peaks are obtained in fair agreement with the experiments.

***Keywords*:** ionization, helium, differential cross section

1. Introduction

In the last years there was a considerable development in the theoretical description and experimental measurement of differential cross sections for charged particle impact ionization of atoms and molecules [1-4]. Nowadays, the interest is focused on the in-detail analysis of the electron ejection from atomic or molecular targets [5-10]. These analyzes may be performed by measuring and calculating fully differential cross sections which gives us the most complete information about an ionization process. These quantities describe the entire energy and angular distribution of the ionized electron, residual ion and projectile.

Beside the study of the ionization of atoms by fast ions, there has been much interest in measuring and calculating fully differential cross sections for the ionization of atoms by slower electrons [11,12]

Previously, based on the semiclassical impact parameter method we have constructed a theoretical model to calculate fully differential cross sections for single ionization of light atoms.

This model takes into account the projectile–target nucleus interaction classically. The method was tested in case of single ionization of helium produced by C^{6+} ion projectile with an energy of E = 100 MeV/u and good agreement with the experiments was achieved in the scattering plane, while in the perpendicular plane a structure similar to that observed experimentally was obtained [13,14].

While for fast ion projectiles the impact parameter method is suitable, it cannot be applied if the atom is bombarded by slow or moderate velocity electrons. In this case the associated wavelength to the projectile becomes comparable to the atomic dimensions, and a fully quantum mechanical treatment is required.

[1] *Faculty of Physics, Babeş-Bolyai University, 400084 Cluj-Napoca, Romania*

In the present work we apply the quantum mechanical Born approximation (BA) and the improved, distorted wave Born approximation (DWBA) for calculating the totally differential ionization cross sections of the helium by electron impact. We compare our results with the experimental data in the scattering plane. This plane is determined by the initial and final momentum vectors of the projectile, and in our calculations we have taken into account the electrons ejected from the atom in this plane. Usually two maxima are obtained in the ejected electron spectrum represented as a function of the ejection angle: the binary peak, which is determined by the projectile-electron two-body collision, and the recoil peak, which is caused by the rescattering of the ejected electron by the target nucleus. In the framework of the Born approximation the binary peak is obtained exactly in the direction of the momentum transfer from the projectile to the target. The post-collision interaction between the two continuum electrons usually modifies the position of this peak.

2. Experimental

The triple differential cross section for the ionization of a helium atom by electron impact may be written as

$$\frac{d^3\sigma}{d\hat{\mathbf{k}}_f d\hat{\mathbf{k}}_e dE_e} = 2(2\pi)^4 \frac{k_f k_e}{k_i} |t|^2, \tag{1}$$

where $\mathbf{k}_f$, $\mathbf{k}_e$ and $\mathbf{k}_i$ are the wave-vectors of the scattered, ejected and incident particles, respectively. Here, the energy of the ejected electron is denoted by E_e, while t stands for the transition matrix element of the system. The factor 2 in the expression above reflects the fact that each of the two electrons from the target can be active. The transition matrix element is given by the following expression

$$t = \left\langle \phi_f(\mathbf{r}_1)\phi_e(\mathbf{r}_2) \left| -\frac{Z}{r_{12}} \right| \phi_b(\mathbf{r}_2)\phi_i(\mathbf{r}_1) \right\rangle. \tag{2}$$

In the above equation ϕ_f, ϕ_e and ϕ_i are the wave functions of the scattered, ejected and incident particles, while ϕ_b denotes the bound state of the active electron. The position vector of the projectile and the ejected electron is $\mathbf{r}_1$ and $\mathbf{r}_2$, respectively, while r_{12} stands for the projectile-ejected electron distance. Z stands for the charge of the projectile, which in our case is –1. Equation .

(2) may also be expressed as:

$$t = \iint \mathrm{d}\mathbf{r}_1 \mathrm{d}\mathbf{r}_2 \phi_f^*(\mathbf{r}_1)\phi_e^*(\mathbf{r}_2) \left| -\frac{Z}{r_{12}} \right| \phi_b(\mathbf{r}_2)\phi_i(\mathbf{r}_1). \tag{3}$$

In order to calculate the matrix element, the wave functions of the scattered, ejected and incident particles are expanded in terms of the partial waves, according to the following expressions

$$\phi_f^*(\mathbf{r}_1) = \sum_{l_f} i^{l_f} \mathrm{e}^{i\sigma_{l_f}} R_{l_f}(k_f, r_1) \sum_{m_f} Y_{l_f m_f}(\hat{\mathbf{r}}_1) Y^*_{l_f m_f}(\hat{\mathbf{k}}_f) \tag{4}$$

$$\phi_e^*(\mathbf{r}_2) = \sum_{l_e} i^{l_e} \mathrm{e}^{i\sigma_{l_e}} R_{l_e}(k_e, r_2) \sum_{m_e} Y_{l_e m_e}(\hat{\mathbf{r}}_2) Y^*_{l_e m_e}(\hat{\mathbf{k}}_e) \tag{5}$$

$$\phi_i(\mathbf{r}_1) = \sum_{l_i} (-i)^{l_i} \mathrm{e}^{-i\sigma_{l_i}} R_{l_i}(k_i, r_1) \sum_{m_i} Y^*_{l_i m_i}(\hat{\mathbf{r}}_1) Y_{l_i m_i}(\hat{\mathbf{k}}_i), \tag{6}$$

where R_{l_x}, $Y_{l_x m_x}$ and σ_{l_x} ($x = f, e, i$) are the radial wave functions, the spherical harmonics and the phase shifts, respectively. Here, the radial wave functions are energy-normalized

$$R_{l_x}(k_x, r_n) = \frac{1}{r_n} \sqrt{\frac{2}{\pi k_x}} y_{l_x}(r_n), \qquad n = 1, 2. \tag{7}$$

The potential present in equation (3) may be expanded into a series of Legendre polynomials

$$\frac{1}{r_{12}} = \sum_{\lambda} \frac{4\pi}{2\lambda + 1} \frac{r_<^\lambda}{r_>^{\lambda+1}} \sum_{\mu} Y_{\lambda\mu}(\hat{\mathbf{r}}_1) Y^*_{\lambda\mu}(\hat{\mathbf{r}}_2). \tag{8}$$

Here, $r_<$ ($r_>$) are the smaller (larger) of r_1 and r_2. We separate the radial and the orbital part of the initial state of the active electron

$$\phi_b(\mathbf{r}_2) = R_{l_b}(r_2) Y_{l_b m_b}(\hat{\mathbf{r}}_2). \tag{9}$$

For $l_b = m_b = 0$, equation (9) becomes:

$$\phi_b(\mathbf{r}_2) = R_0(r_2) Y_{00}(\hat{\mathbf{r}}_2); \qquad Y_{00} = \frac{1}{\sqrt{4\pi}}, \tag{10}$$

where

$$R_0(r_2) = \frac{1}{r_2} y_0(r_2). \tag{11}$$

By inserting equations (4)-(11) into (3), the matrix element is expressed as follows:

$$\begin{aligned} t \;=\; & (-Z) \sum_{l_f l_e l_i \lambda} i^{l_f} \mathrm{e}^{i\sigma_{l_f}} i^{l_e} \mathrm{e}^{i\sigma_{l_e}} (-i)^{l_i} \mathrm{e}^{-i\sigma_{l_i}} \\ & \times \iint \mathrm{d}r_1 \mathrm{d}r_2 r_1^2 r_2^2 R_{l_f}(k_f, r_1) R_{l_e}(k_e, r_2) \frac{r_<^\lambda}{r_>^{\lambda+1}} R_0(r_2) R_{l_i}(k_i, r_1) \\ & \times \frac{\sqrt{4\pi}}{2\lambda + 1} \sum_{m_f m_e m_i \mu} \int \mathrm{d}\hat{\mathbf{r}}_1 Y_{l_f m_f}(\hat{\mathbf{r}}_1) Y_{\lambda\mu}(\hat{\mathbf{r}}_1) Y^*_{l_i m_i}(\hat{\mathbf{r}}_1) \\ & \times \int \mathrm{d}\hat{\mathbf{r}}_2 Y_{l_e m_e}(\hat{\mathbf{r}}_2) Y^*_{\lambda\mu}(\hat{\mathbf{r}}_2) \\ & \times Y^*_{l_f m_f}(\hat{\mathbf{k}}_f) Y^*_{l_e m_e}(\hat{\mathbf{k}}_e) Y_{l_i m_i}(\hat{\mathbf{k}}_i). \end{aligned} \tag{12}$$

Performing the integration over the angles of $\mathbf{r}_1$ and $\mathbf{r}_2$, the triple differential cross section may be written as:

$$\frac{d^3\sigma}{d\hat{\mathbf{k}}_f d\hat{\mathbf{k}}_e dE_e} = 2\frac{64\pi}{E_i} \times \left| \sum_{l_f l_e l_i} A(l_f l_e l_i) \sum_{m_f m_e m_i} M(l_f l_e l_i; m_f m_e m_i) \right|^2, \tag{13}$$

where

$$A(l_f l_e l_i) = i^{l_f} \mathrm{e}^{i\sigma_{l_f}} i^{l_e} \mathrm{e}^{i\sigma_{l_e}} (-i)^{l_i} \mathrm{e}^{-i\sigma_{l_i}} \tag{14}$$

$$E_i = \frac{k_i^2}{2}. \tag{15}$$

and

$$M(l_f l_e l_i; m_f m_e m_i) = \iint \mathrm{d}r_1 \mathrm{d}r_2 y_{l_f}(r_1) y_{l_e}(r_2) \frac{r_<^{l_e}}{r_>^{l_e+1}} y_0(r_2) y_{l_i}(r_1) \times \sqrt{\frac{(2l_f+1)(2l_i+1)}{2l_e+1}} \begin{pmatrix} l_f & l_e & l_i \\ 0 & 0 & 0 \end{pmatrix} \times (-1)^{m_i} \begin{pmatrix} l_f & l_e & l_i \\ m_f & m_e & -m_i \end{pmatrix} \times Y^*_{l_f m_f}(\hat{\mathbf{k}}_f) Y^*_{l_e m_e}(\hat{\mathbf{k}}_e) Y_{l_i m_i}(\hat{\mathbf{k}}_i). \tag{16}$$

Here, E_i is the impact energy of the projectile, while the mathematical entities in the brackets are called the Wigner 3j-symbols.

The expressions above give only the direct ionization cross section, which do not contain the exchange effect due to the indistinguishability of the projectile and target electrons. In order to take into account the exchange effect, we have to add to the *t* direct amplitude (2) the exchange amplitude, in which we exchange the coordinates of the scattered and ejected electrons relative to the direct amplitude. In our calculations we have taken into account this exchange effect.

Based on the formulae above one can calculate numerically the differential cross section, if the radial wave functions (7) are known. We have adopted two types of approximations for these wavefunctions. In the Born approximation (BA) the wavefunctions of the incident and scattered electron are plane waves. After the partial wave expansion the radial part of these plane waves is given by the spherical Bessel functions. In the BA the radial wavefunctions of the ejected electron are given by the Coulomb waves calculated in the field of the residual ion taken as a point like charge.

In the distorted-wave Born approximation (DWBA) every continuum wavefunction is calculated numerically in the field created by the nucleus and the bound electrons of the target. For the incident and scattered electron two bound electrons are taken into account, while for the slower ejected electron just the one electron of the residual ion creates the screening field.

The bound state of the helium (10) is described by a Hartree-Fock wavefunction.

3. Results and discussions

We have performed calculations for the ionization of helium by low and moderate velocity electrons. The obtained totally differential cross sections (TDCS) in the scattering plane are compared to the experimental data. Because usually experimental TDCS are not on the absolute scale, we have normalized our results and the experimental data at the binary peak to the unity.

Figures 1-3 represent our results obtained with the BA and DWBA compared to the experimental data of [9] as a function of the electron ejection angle. The incident electron energy is 250 eV, while the ejected electron has the energies 10, 20 and 50 eV. The scattering angle is taken to be -15°.

Figures 4-6 represent the results obtained with the same approximations compared with the experimental results of [10]. In this case the energy of the scattered electron is 500 eV, while the ejected electron has the energies 37, 74 and 205 eV. The incident energy is adjusted to fulfill the energy conservation requirement. The scattering angle is taken to be -6°.

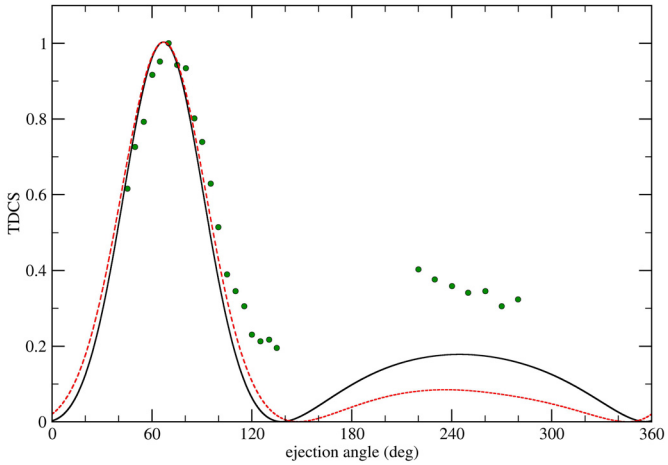

Figure 1. FDCS in arbitrary units for the ionization of helium by electron impact as a function of electron ejection angle. The projectile energy is 250 eV, while the ejected electron energy 10 eV and the scattering angle is -15°. Our results (BA – solid line, DWBA – dashed line) are compared to the experimental data [9] (dots).

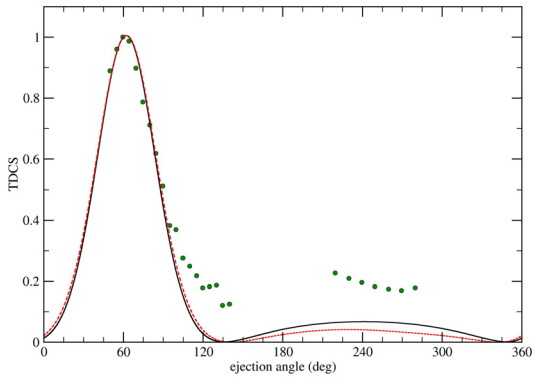

Figure 2. Same as Figure 1**.** except the ejected electron energy is 20 eV.

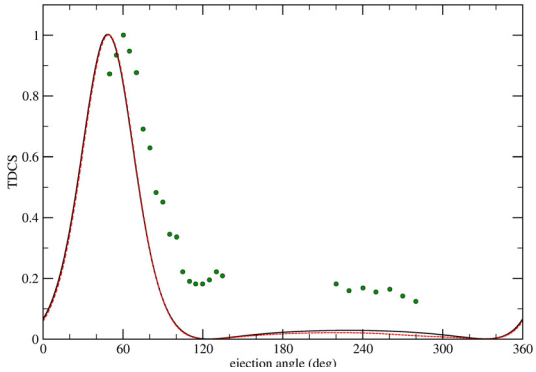

Figure 3. Same as Figure 1. except the ejected electron energy is 50 eV.

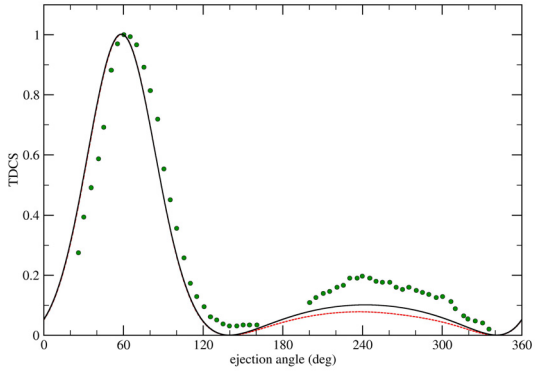

Figure 4. FDCS in arbitrary units for the ionization of helium by electron impact as a function of electron ejection angle. The energy of the scattered electron is 500 eV, while the ejected electron energy 37 eV and the scattering angle is -6°. Our results (BA – solid line, DWBA – dashed line) are compared to the experimental data [10] (dots).

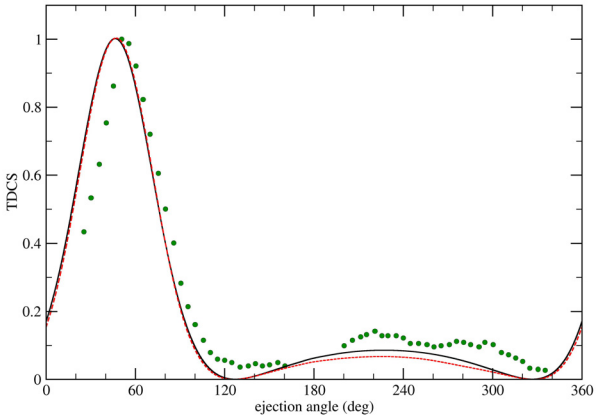

Figure 5. Same as Figure 4. except the ejected electron energy is 74 eV.

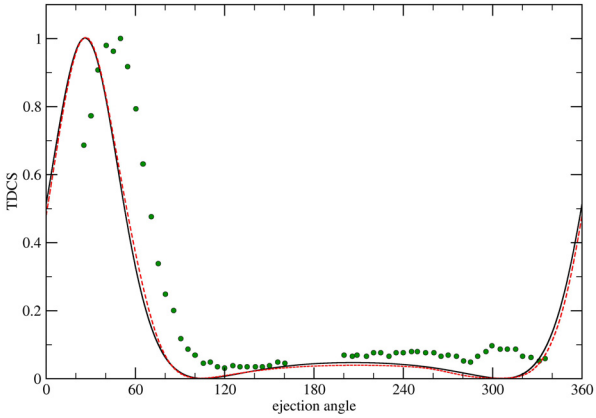

Figure 6. Same as Figure 4. except the ejected electron energy is 205 eV.

As one may observe, our results are in fair agreement with the experimental data. We obtain in all cases both the binary peak and the recoil peak. Because our method is not exact, there is a shift of the position of the binary peak between our results and the experiments. Also, we do not reproduce exactly in all cases the relative height of the recoil peak.

The two applied methods give very similar results. One may conclude, that in order to obtain results in better accordance with the experiments, is not enough to take into account the static distortion of the electron waves.

In order to obtain the position of the binary peak in accordance with the experimental data, and not at the direction of the momentum transfer, one should take into account the post collision interaction between the emerging electrons. This will be the topic of our further investigations.

4. Conclusions

We have investigated the ionization of the helium by slow and moderate velocity electron impact. Fully differential cross sections were calculated within the framework of the BA and DWBA. Our results are in fair agreement with the experiments. In order to improve this agreement, one should take into account the post collision interactions of the emerging electrons.

Acknowledgment

The present work has been supported by the Romanian National Plan for Research (PN II), contract No. ID 539.

REFERENCES

1. Ehrhardt H, Jung K, Knoth G and Schlemmer P 1986 *Z. Phys. D* 1 3
2. Ullrich J, Moshammer R, Dorner R, Jagutzki O, Mergel V, Schmidt-Bocking H and Spielberger L 1997 *J. Phys. B: At. Mol. Opt. Phys.* 30 2917
3. Roder J, Erhardt H, Pan C, Starace A F, Bray I and Fursa D V 1998 *J. Phys. B: At. Mol. Opt. Phys*. 31 L525
4. Dorner R, Mergel V, Jagutzki O, Spielberger L, Ullrich J, Moshammer R and Schmidt-Bocking H 2000 *Physics Reports* 330 95
5. Ullrich J, Moshammer R, Dorn A, Dorner R, Schmidt LPH, Schmidt-Bocking H 2003 *Rep. Prog. Phys.* 66 1463
6. Schulz M, Moshammer R, Fischer D, Kollmus H, Madison D H, Jones S and Ullrich J 2003 *Nature* 422 48 and references therein
7. Schulz M, Moshammer R, Fischer D and Ullrich J 2004 *J. Phys. B: At. Mol. Opt. Phys.* 37 4055
8. Dimopoulou C *et al* 2004 *Phys. Rev. Lett* 93 123203
9. Milne-Brownlie D S, Foster M, Junfang Gao, Lohmann B, Madison D H 2006 *Phys. Rev. Lett* 96 233201
10. Staicu Casagrande E M *et al* 2008 *J. Phys. B: At. Mol. Opt. Phys.* 41 025204
11. Baran J L, Das S, Jarai-Szabo F, Pora K, Nagy L, and Tanis J A 2008 *Phys. Rev. A* 78 012710
12. Jarai-Szabo F, Nagy L 2007 *J. Phys. B: At. Mol. Opt. Phys.* 40 4259
13. Jarai-Szabo F, Nagy L 2009 *Nucl. Instr. Meth. B* 267 292

STUDIA UNIVERSITATIS BABEŞ-BOLYAI, PHYSICA, LIV, 2, 2009

MAGNETIC STATES IN Co RICH FCC CoMn ALLOYS

A. NEDELCU[1], V. CRISAN

ABSTRACT. We report on the results of the ab initio calculations on the $Co_{0.95}Mn_{0.05}$ alloy in chemically disordered state. Calculations are carried out within density-functional theory and the coherent potential approximation (CPA). We show that the magnetic coupling between the Co and Mn atoms are of ferromagnetic (FM) type for large lattice parameters while for lower ones are antiferromagnetic (AF). The coupling between Mn atoms is found to be FM for all lattice parameters. No chemically ordering is seen, all sites in the fcc unit cell being magnetically equivalent. The results are discussed in the framework of the disordered local moment (DLM) model.

Keywords: alloys, transition-metal KKR, CPA, DLM

1. Introduction

The 3d transition metal impurities in Co produce a magnetic moment disturbance localized near the impurity atoms as well as on the impurity magnetic moment itself. For CoMn alloy system the average magnetic moment shows a sharp departure from the Slater-Pauling curve with moment decrease of 4.5 μ_B/Mn atom [1] In hcp Co the Mn impurities induce negative magnetic moment disturbances at least to the second neighbor shell of the impurity atom, [2].

Because of the very low Mn concentration we expect a very small interaction between the impurities at least at large lattice parameters.The magnetic coupling between Mn and Co atoms in CoMn system is still a mater of controversy. In bulk CoMn alloys no chemical ordering is seen while the surface alloy has c(2X2) ordering.

2. Experimental

In order to study the degree of chemical and/or spin ordering we used the KKR-CPA-MS, [3] method in the framework of density functional theory and LSDA in the parameterization of Moruzzi-Janak-Williams [4]. The single-site effective medium theory as CPA works satisfactorily with the exception of systems with large magnetic moments which can have some different but energetically almost degenerate orientations. The use of multisublsttice (MS) form of the KKR-CPA method allow to split the lattice in many sublattices with sites having different concentration of the alloy components. The spin ordering of local magnetic moments was found by imposing

[1] *Faculty of Physics, Babeş-Bolyai University, Kogălniceanu 1, 400084 Cluj-Napoca, Romania*

to different sublattices the same chemical compositions while considering sublattices as being different. The fcc lattice decomposition in our calculations is shown in Figure 1. The atoms located in the corners of the fcc cell form the sublattice I, while the atoms from the faces of the cube the sublattice II. The composition of each sublattice is given actually by the alloy formula. This way the binary alloy A_xB_{1-x} is substituted by a pseudoternary alloy$A^I_sA^{II}_uB^I_tB^{II}v$ with s+u = x and t+v = 1-x. The Figure 1 describes the $L1_0$ type of ordering. This type of chemical ordering was found in the FeNi alloys [5] but is not present in this alloy system. However, considering the two sublattices as different sublattices we allow the spins to have different behaviors.

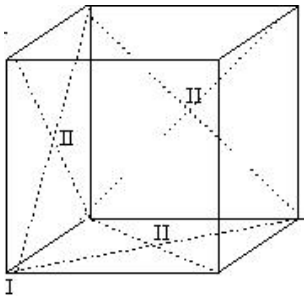

Figure 1. The sublattice $L1_0$ decomposition of the MnCo fcc lattice.

The LSDA usually overestimate the bonding which leads to lower lattice parameters than the experimental ones. We expect the magnetovolume effect to appear at lower lattice parameter than the experimental one.

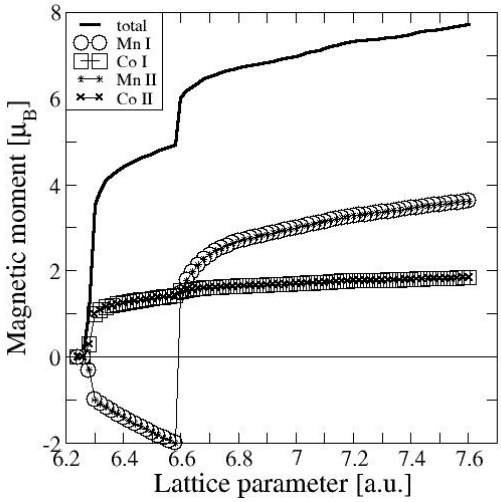

Figure 2. Total and atomic magnetic moments vs. lattice parameter for $Mn_{0.05}Co_{0.95.}$ Open symbols are for atoms located in the sublattice I, while small triangle and full small circle are for atoms located in sublattice II.

3. Results and disscutions

The total and local magnetic moments for $Mn_{0.05}Co_{0.95}$ as function of the lattice parameter is shown in Figure 2. For large lattice parameter the coupling between Mn and Co atoms are of FM type. For intermediate lattice parameter the Mn moments are oriented opposite of the total moment which produced an jump in the total magnetic moment. At lower lattice parameter the sublattice average moment for Mn atoms as well as for Co atoms vanish. While at large lattice parameters the DLM is not valid at lower lattice parameter the average magnetic moment can indicate an AF ordering between atoms. Because of the small interatomic distances the interaction between Mn atoms increases and the DLM model seems to be valid. In that case the coupling between the Mn and Co atoms can fluctuate function of local environment.

REFERENCES

[1] Cable, Hicks Phys. Rev. B2, 176 (1970)

[2] J. B. Cowly, J. Phys. C 1,428 (1968)

[3] H. Akai, P. H. Dederichs, Phys. Rev., 47, 8739, (1993)

[4] V.L. Moruzzi, J.F. Janak, A.R. Williams, Calculated Electronic Properties of Metals (Pergamon, New York, 1978)

[5] V. Crisan, P. Entel, H. Ebert, H. Akai, D. D. Johnson, J. B. Stauton, Phys. Rev. B66, 014416, (2002)

STUDIA UNIVERSITATIS BABEŞ-BOLYAI, PHYSICA, LIV, 2, 2009

DETERMINATION OF THEOPHYLLINE IN BIOLOGICAL FLUIDS BY ISOTOPIC DILUTION MASS SPECTROMETRY

ANDREEA IORDACHE, CORNELIA MESAROS, ONUC COZAR, MONICA CULEA[1]*

ABSTRACT. A sensitive analytical method for theophylline determination in biological samples was developed by isotopic dilution mass spectrometry. Quantitative determination of the drug from the resultant tracer spectrum requires deconvolution of the enrichment of the isotopomers. Deconvolution of the ion abundance ratios to yield tracer-to-tracee ratios for each isotopomer was done using Brauman's least squares approach. Comparisons with other other calculation method is presented.

Keywords: Drug, biological fluids, isotopic dilution, mass spectrometry, deconvolution

1. Introduction

Accurate measurements of isotopic abundances need careful preparation of standard mixtures and careful attention to the analytical parameters of the system to be studied. Many mass spectrometric methods for drug determination in biological fluid have been described [1-13].

Theophylline is a drug frequently used in the neonatal intensive care units for infants with apnea of prematurity or in asthma treatment. The therapeutic level of the drug in plasma is between 5-15 μg mL^{-1}. Quantitative determination was performed by addition to the sample, before extraction, of known amounts of internal standard, the isotopic labelled analogue. The method will compensate the sample losses in the clean-up stage, assuming that the losses of the standard are identical with those of the analyte. The use of isotopic tracers demands accurate measurements of the isotopic abundances of each tracer in order to construct a design matrix of simultaneous linear equations. The system of equation may be solved by standard matrix algebraic techniques [14,15].

The aim of this study was to compare two calculation methods for drug determination in biological fluids. The method was applied for the treatment optimization in clinic.

[1] *Babes-Bolyai University, Biomedical Physics Dept., 1 Kogalniceanu str, 3400 Cluj-Napoca, Romania*
** E-mail: mculea@phys.ubbcluj.ro*

2. Materials and method

A gas chromatography-mass spectrometry method is presented to measure the isotopic enrichment of theophylline isotopomers. The method had good analytical linearity between 0 and 40 $\mu g.mL^{-1}$ and both precision and accuracy were 5% for plasma amino acids. Sensitivity permitted analysis of 100 pg drug on column. Plasma and saliva concentrations of the drug were determined after addition of (^{15}N)theophylline as internal standards to 500 microL of plasma or saliva. The resultant tracer spectrum requires deconvolution of the enrichment of the isotopomer of the drug. Deconvolution of the ion abundance ratios to yield tracer-to-tracee ratios for each isotopomer was done using Brauman's least squares approach.

3. Experimental

^{15}N-theophylline, 74,2 atom % ^{15}N was used as internal standard. Theophylline was administered orally in children with asthma using Teo-Dur (Key Pharmaceuticals, Inc., USA), while infants received I.V. aminophylline. A EI Hewlett Packard 5989B mass spectrometer coupled to a 5890 gas chromatograph were used in the conditions: electron energy 70 eV; electron emission 300µA and ion source temperature 200^{o}C. The gas chromatograph-mass spectrometer (GC-MS) assay used a HP-5MS fused silica capillary column, 30mx0.25mm, 0.25µm film-thickness, programmed from 200^{o}C to 270^{o}C at 10^{o}C min^{-1}, the flow rate 1ml min^{-1}, with helium as carrier gas. Retention time for theophylline and internal standard was 4.2min. The molecular ion *m/z* 180 for theophylline and the molecular ion *m/z* 181 for the internal standard, were monitored for quantitative analyses in the selected ion monitoring (SIM) mode.

Extraction procedure:

0.5 ml of plasma containing the analyte (theopphylline) was placed into a 5 ml screw-cap vial and 5µl of internal standard ^{15}N-theophylline, 1 ml of the extraction solvent, chloroform: isopropanol 20:1 v/v and 0.2 g NaCl were added. After 1 min of mechanical mixing, the sample was centrifuged for 3 min and injected into the GC from the lower layer.

Population:

Two different groups were studied: A, formed by 27 children with asthma aged 2-16 years old, treated with slow-released theophylline and B, consisting from 13 infants with apnea of prematurity, aged between 2-10 weeks. Theophylline concentration measurements were performed in 40 hospitalized infants and children treated with theophylline for apnea of prematurity or asthma. A dose of 15.1mg kg^{-1} $24h^{-1}$, for group A was used. Blood and saliva paired samples were taken, at 4 hours and at 8 hours after morning dose. In group B, a loading dose of 5mg kg^{-1} of I.V.

aminophylline was administered and maintenance doses of 3mg kg^{-1}, every 8 hours. Plasma and saliva were sampled at 2 and 4 hours after loading dose and at 4 and 8 hours in the second and third day. Written informed consents were obtained from each subject parent prior to this study.

4. Results and Discussion

Calculation:

Regression curve obtained by using the mass spectrometric method and the least squares with matrix calculation were compared to correlate the levels of the drug in human plasma and saliva. Regression curve obtained by using standards with known concentration of theophylline in the range 0-40µg.mL^{-1} and the same quantity of the internal standard, 10µg.mL^{-1}, was y=0.336x = 0.103.

Isotopic deconvolutions:

The use of the isotopic labeled analogue of the analyte (the drug of interest) as internal standard and the presence of the analyte (tracer) with their natural isotopic abundance in plasma necessitate careful correction of the mass spectrum, to deconvolute the information of interest. Fractional isotopic abundances for natural theopphylline and isopopomer were calculated from experimentally measured isotopic ratios and synthetic isotopic ratios in the case when the isotopomer needed was missing. The set of simultaneous linear equations [14,15], each describing the isotopic contributors had to be solved having the general form:

$$I_x = \sum_{x=i,j} A_i X_j \quad (1)$$

where I_x represents the relative ion abundance for the x^{th} ion; X_j represents the unknown fractional abundance. The relative abundance of the contributors (A_i) was calculated for the two ions expressing the simultaneous equations in matrix notation:

$$I=AX \quad (2)$$

The least squares solution of X can be obtained by using the inverse of A transpose:

$$X=(A^T A)^{-1} A^T I \quad (3)$$

Table 1 is an example of a matrix construction in an experimental metabolic study.

Table 2 presents the vectors for the samples peak areas at m/z 180:[M]and 181:[M+1]. The samples were measured twice (n=2).

Table 1.

The matrix design (left) and the pseudoinverse matrix(right) used for theophylline calculation

theophylline	[M]	[M+1
n.a.	0.95	0.05
^{15}N	0.27	0.73

theophylline	[M]	[M+1]
n.a.	1.07	-0.07
^{15}N	-0.40	1.40

Table 2.

The measured isotopic ratios for theophylline in samples no.137-142 (n=2)

Sample	(M+0)	(M+1)
137	62.00	57.00
137	120.00	113.00
138	130.00	109.00
138	27.00	21.00
139	91.00	81.00
139	79.00	68.00
140	190.00	101.00
140	74.00	40.00
141	128.00	90.00
141	105.00	73.00
142	71.00	68.00
142	17.00	13.00

In the design matrix, in the position [M+1] for theophylline (m/z 180}, especially the natural contribution of the isotope ^{13}C is presented. In the case of ^{15}N-theophylline (m/z 181), in the position [M+1], especially the contribution of ^{15}N-theophylline (74,2 atom % ^{15}N), is presented but also the contribution of the isotope ^{13}C.

Table 3 presents the corrected data after multiplying the sample vector and the pseudoinverse matrix. The two values of each sample were averaged and then the normated matrix was obtained (Table 4).

Table 5 presents the quantitative values for drug calculated in plasma and saliva taking into account the standard and biofluid quantity.

Table 3.

The corrected isotopic ratios for theophylline in samples no.137-142 (n=2)

Sample	[M + 0]	[M +1]
137	43.93	75.07
137	83.96	149.04
138	96.28	142.72
138	20.65	27.35
139	65.53	106.47
139	57.81	89.19
140	163.87	127.13
140	63.56	50.44
141	101.68	116.32
141	83.74	94.26
142	49.22	89.78
142	13.09	16.91

Table 4.

Normated,and corrected isotopic abundances for plasma and saliva samples

sample	biofluid	[M + 0]	[M +1]
137	plasma	57.06	100.00
138	saliva	68.75	100.00
139	plasma	63.04	100.00
140	saliva	128.07	100.00
141	plasma	88.04	100.00
142	saliva	58.40	100.00

Table 5.

The concentrations ($Z_{i,j}$) of samples in µg. mL^{-1}

sample	[M + 0]	[M + 1]
137	5.71	10.00
138	6.88	10.00
139	6.30	10.00
140	12.81	10.00
141	8.80	10.00
142	5.84	10.00

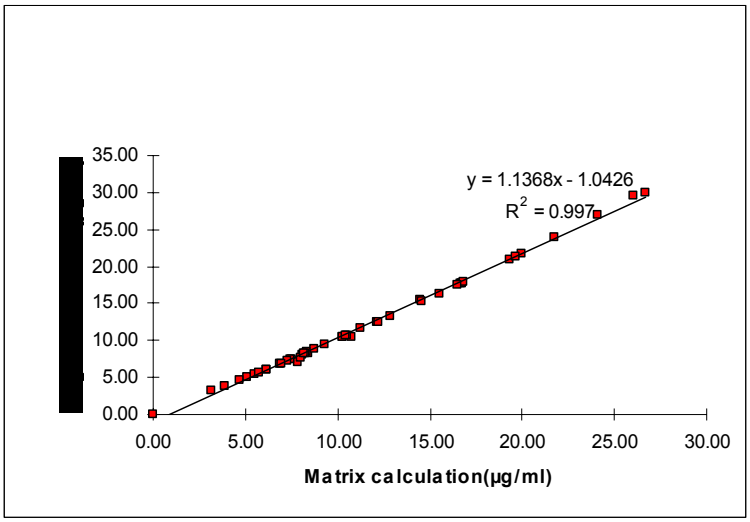

Figure 1. The comparison of the two calculation methods: (regression curve and matrix)

The results obtained for the plasma and saliva samples gave a good correlation by using the two methods of calculation. Figure 1 presents the comparison of the two calculation methods. The calculated coefficient of correlation was 0.9985.

Figure 2 presents the good correlations between plasma and saliva drug values obtained in the two groups of patients. Plasma and saliva levels of drug are presented in Table 6.

Table 6.

Comparative values of plasma and saliva levels of theophylline in group (27 children) and group B (13 infants)

Population	Range, µg mL^{-1}	Mean ± SD, µg.mL^{-1}
Plasma levels		
Group A=Children	1.98 – 21.96	7.98 ± 5.25
Group B=Infants	1.62 – 27.90	7.76 ± 5.85
Saliva levels		
Group A=Children	1.41 – 15.06	5.12 ± 3.45
Group B=Infants	1.02 – 18.23	5.51 ± 4.61
Saliva / plasma ratio		
Group A=Children	0.47 – 0.71	0.60 ± 0.09
Group B=Infants	0.43 – 0.88	0.69 ± 0.13

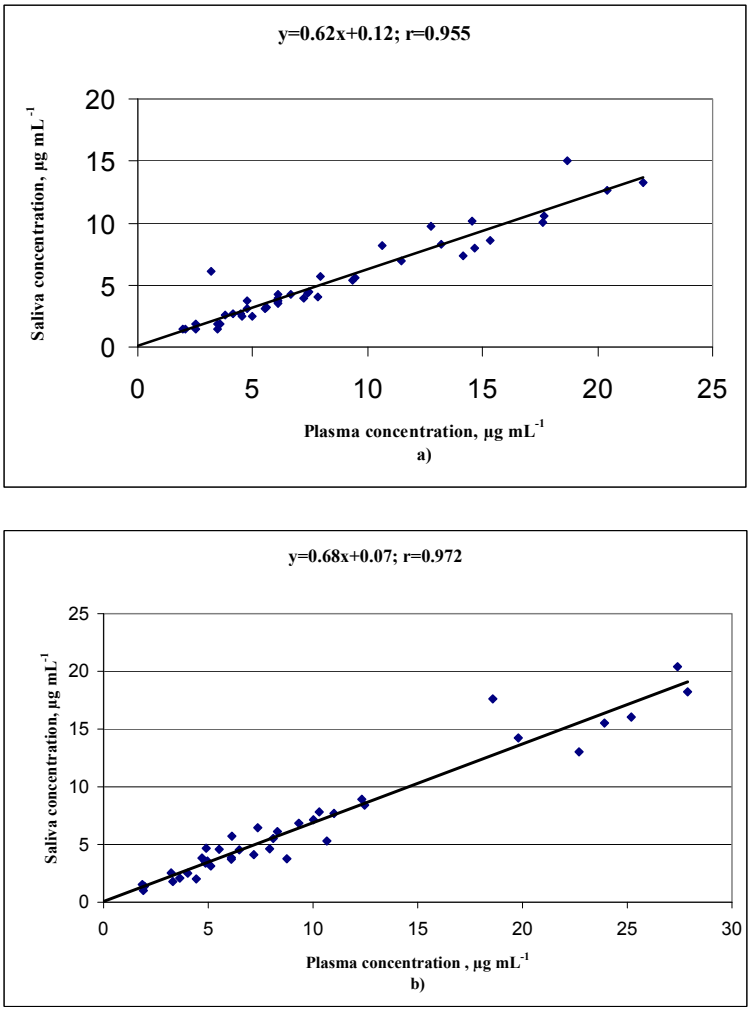

Figure 2. Correlation between plasma and saliva theophylline concentration in the two groups: a) group A = Children; b) group B = Infants

5. Conclusions

The isotope dilution mass spectrometric method used is simple, precise and rapid. The regression curve method of calculation gave similar results as the matrix calculation method (r=0.999). Good correlation was obtained between the drug levels measured in plasma and saliva.

REFERENCES

1. G.J. Park, P.H Katelaris, D.B., Jones, F. Seow, D.G. Le Couteur, M.C., Ngu, Hepatology, 38, 1227 (2003).
2. S. Wittayalertpanya, V. Mahachai, J. Med. Assoc. Thai. 84, .S189 (2001).
3. M. Culea, N. Palibroda, P. Panta Chereches, M. Nanulescu, Chromatographia, 53, S387 (2001).
4. N. Yamane, T. Takami, Z. Tozuka, Y. Sugiyama, A. Yamazaki, Y. Kumagai, Drug Metabolism Pharmacokinetics, 24, 389 (2009).
5. M. Lessio Castro, W. R. Vilela, R. C. Zauli, M. Ikegaki, V. L. Garcia Rehder, M.A. Foglio, S. Matias de Alencar, P. L. Rosalen, BMC Complement Altern. Med. 9, 25 (2009).
6. P. Meng, D. Zhu, H. He, Y. Wang, F.Guo, L. Zhang, Analytical Sciences, 25, 1115 (2009).
7. B. Fang, Y. Su, H. Ding, J. Zhang, L. He, Anal. Scie., 25, 1203 (2009).
8. R.D. Lowe, G.E. Guild, P. Harpas, P. Kirkbride, P. Hoffmann, N.H. Voelcker, H. Kobus, Rapid Commun Mass Spectrom. 23, 3543 (2009).
9. M. Culea, C. Mesaros, E. Culea, "Chemické listy" Journal, 102, s961 (2008).
10. D.M. Kraus, J.H. Ficher, S.J. Reitz, S.A. Kecskes, T.F. Yeh, K.M. McCulloch, E.C. Tung, M.J. Cwik, Clin. Pharmacol. Ther., 54, 351 (1993).
11. M. Culea, N. Palibroda, M. Chiriac, Z. Moldovan, Biomed. Environm. Mass Spectrom. 19, 360 (1990).
12. M. R. Loizzo, F. Menichini, R. Tundis, M. Bonesi, F. Conforti, F. Nadjafi, G. A. Statti, N.G. Frega, F. Menichini, J. Oleo. Sci., 58, 443 (2009).
13. N. Uchiyama, R. Kikura-Hanajiri, N. Kawahara, Y. Haishima, Y. Goda, CHEM. & PHARM. BULL., 57, 439 (2009).
14. J. I. Brauman, Spectral Analysis: Methods and Techniques, Ed. by J. A. Backburn, Marcel Dekker, New York (1970).
15. K. Nakamura, D.L. Hachey, C.S. Kreek, C.S. Irving, P.D. Klein, J. Pharm. Sci. 71, 40 (1982).

STUDIA UNIVERSITATIS BABEŞ-BOLYAI, PHYSICA, LIV, 2, 2009

A STUDY ON TRACE METALS IN AIRBORNE PARTICULATE MATTER USING ICP-MS TECHNIQUE

ANDREEA IORDACHE[1,2], MONICA CULEA[1], ONUC COZAR[1]

ABSTRACT. Atmospheric particles are generated through a variety of physical and chemical mechanisms, and are emitted into the atmosphere from numerous sources, by combustion, industrial and natural processes. There is a general agreement that airborne particulate matter is associated with adverse effects on human health. Determination of trace element concentrations in atmospheric aerosols is important because of their toxic effects on human health, for example, high levels of lead in the body can cause motor nerve paralysis, anaemia, and, in children, inhibition of the nervous system's development. High cadmium levels can cause cardiovascular problems and bone thinning.

The aim of our study was to determine the concentration of trace elements (Pb, Cd, Ni, Co, Cr, Cu and Mn) in the PM10 fraction. Destructive analytical procedures include microwave-assisted digestion of filter-based samples, which was followed by inductively coupled plasma - mass spectrometry (ICP-MS) determinations.

The procedure was applied to filters containing PM10 particles collected in the industrial area from Valcea, Romania.

Keywords: ambiental air, suspended particulate matter, PM10 fraction, ICP-MS

1. Introduction

Over the past two decades, a number of epidemiological studies has provided sufficient evidence that exposure to ambient particulate matter (PM) poses a significant threat on human health.

Atmospheric particles are generated through a variety of physical and chemical mechanisms, and are emitted into the atmosphere from numerous sources, by combustion, industrial and natural processes. They are involved in many atmospheric processes, and play an important role in reducing visibility, acid deposition, and the balance of radiation in the atmosphere[1]. There is a general agreement that airborne particulate matter is associated with adverse effects on human health[2]. The concentration and composition of particles may vary with size, time, and location, and depends strongly on the distance from the source, rate of emission, convective and

[1] *Babes-Bolyai University, Biomedical Physics Dept., 1 Kogalniceanu str, 3400 Cluj-Napoca, Romania*
[2] *National R&D Institute of Cryogenics and Isotopic Technologies – ICSI Rm. Valcea, 4 Uzinei St., Rm. Valcea, 240050, Romania, e-mail: andres_iro2002@yahoo.com*

turbulent diffusive transfer rates, on the efficiency of various removal mechanisms, and on meteorological parameters which affect vertical and horizontal distribution[3]. Toxicological studies have frequently implicated metal content (particularly water-soluble metal) as a possible harmful component of particulate matter. *In vivo* and *in vitro* studies have shown that metals generate reactive oxygen species, that activate cellular inflammatory response pathways[4].

Airborne particulate matter consists of many different substances suspended in air in the form of particles (solids or liquid droplets) that vary widely in size. Although particle size distribution and particle number are considered closely associated to adverse health outcomes, it would be fallible to underestimate the importance of the chemical composition of particles and especially of their content in toxic substances. The particles having a size, < 10 mm in diameter (PM10) are enough to be inhaled into the lungs where the chemicals ranging from metal compounds to acid droplets lead to severe health risk, especially respiratory problems in children and the elderly living in large metropolitan areas[5]. These particles pose the greatest health concern because they can pass through the nose and throat and get into the lungs. Particles larger than 10 micrometers in diameter that are suspended in the air are referred to as total suspended particulates (TSP). These larger particles can cause irritation to the eyes, nose and throat in some people, but they are not likely to cause more serious problems since they do not get down into the lungs.

In order to address this issue, the European Union (EU) has promulgated air quality standards for PM10 (EN 14902 "Ambient air quality-Standard method for the measurement of Pb, Cd, As, and Ni in the PM10 fraction of suspended particulate matter"). The 4th daughter directive of the EU air quality Framework Directive will require the long term assessment of lead, arsenic, nickel and cadmium concentrations, setting certain assessment thresholds, and render the fixed measurement of ambient concentrations mandatory when these thresholds are exceeded. However, uncertainty exists on the specific aerosol properties that are responsible for the health effects.

Among the various types of methods used for the measurement of trace elemental concentrations in environmental samples, the most popular ones include neutron activation analysis (NAA), X-ray fluorescence (XRF), particle-induced X-ray emission analysis (PIXE), stripping voltammetry (SV), atomic absorption spectroscopy (AAS), inductively coupled plasma (ICP) techniques. Among all these methods, ICP-MS has come to be one of the most attractive detection systems, as it is relatively fast, multi-elemental and quantitative[6].

In this study we report the composition in metals of PM10 level of particulate matter, examine the levels of concentrations in the industrial area, in Ramnicu-Valcea. Elemental concentrations were determined using an ICP-MS Varian 820 to analyze the ambient air filter samples.

2. Experimental

Materials and reagents

In order to check the instrumental errors, high purity ICP Multi Element Standard Solution VI CertiPUR 10 mg/L for Cd, Pb, Ni, Co and Cu obtained from Merck (Darmstadt, Germany) were used for external calibration during semi-quantitative analysis. Mixed cellulose ester membrane filters (47 mm diameter, Whatman) were used for the preparation of filter blanks. All solutions were prepared and stored in polypropylene vessels, which were cleaned prior to use by soaking in 10% HNO_3 and then rinsed several times with ultra-pure water, which was produced by a Smart 2 Pure system, TKA (resistivity of 18.2MΩ cm). An 63% HNO_3 for ICP-MS determination was used for microwave digestion preparation. The purity of the gaseous argon used to form the plasma in the ICP-MS was 99.9999 % (Messer, Austria).

All calibration solutions were prepared daily, at appropriate mass fractions as the samples to be analyzed, and in the same acid matrix as the sample and filter blank solutions.

Method

Sampling of PM10 was performed at an industrial location, Ramnicu Valcea with a reference medium volume sampler (Sven Leckel, MVS6) and with a Whatman 47 filter paper for 24 hours in the period august-october 2009. The sampling was done by drawing ambient air through the filter material by using a pump. The sampler was placed ca. 1.5 m above ground level and away from any obstructions to the free flow of air around the sampler. The sampler was operated at a known flow rate (2.3 m^3/h) for 24 h at 20±5 °C and 50±5 % relative humidity. Sampling was carried out with a frequency, twice a month for a period of three months.

The filters were cut longitudinally into strips and were totally digested in sealed teflon (PTFE) vessels by microwave assisted extraction (MAE), which appears superior to the traditional hot-plate method. Sample digestion was carried out using a Mars 5 Microwave System (CEM Microwave Technology Ltd., UK). The PTFE, closed microwave vessels were pre-cleaned by adding 10 ml of 63%HNO3. Samples to be digested were placed in the vessel with 10 ml of 63% HNO3, increasing the microwave temperature to 200°C over a 10 min period, and holding the temperature at 200° C for 5min. The temperature was then increased to 220°C over a 10 min period, and held at 220 °C for 20 min. Conditions for digestion are describe in Table 1:

Table 1.

Digestion programme using HNO_3

Step	Power (W)	% Power	Ramp (min)	Pressure (PSI)	Temperature (^{0}C)	Hold (min)
1	800	80	10	55	200	5
2	800	80	10	55	220	20

After cooling, all samples were diluted to a minimum of 100 ml with ultra-pure water before analysis. The dilution levels ensured that concentrations of analyte in solution were low enough so that not present special challenges in the interpretation of the ICP-MS data.

Subsequently, the extracts were analyzed using an Inductively Coupled Plasma/Mass Spectrometer (ICP-MS) Varian 820 equipped with an SPS-3 autosampler (Varian, Australia). All samples were introduced via the autosampler system with a peristaltic pump into the first channel. Each sample was analyzed in duplicate, each analysis consisting of five replicates.

This method allowed us to perform multi-element determination of trace elements. In this method, the extract solution is introduced by pneumatic nebulization into a radiofrequency- generated argon plasma where energy transfer processes cause analyte desolvation, atomization, and ionization. The ions are extracted from the plasma through a differentially pumped vacuum interface and separated on the basis of their mass-to-charge ratio by a quadrupole mass spectrometer. The ions transmitted through the quadrupole are registered by a continuous dynode electron multiplier and the ion information is then processed by a PC-based data handling system.

Prior to analysis, the ICP-MS, located in a temperature-controlled laboratory (18 ± 2 °C), was allowed a sufficient period of time to stabilize before optimization procedures were carried out. Instrumental operation parameters are given in Table 2.

Tabel 2.

Instrumental (a) and data acquisition (b) parameters of ICP-MS

(a) Instrumental parameters

RF power	1400 W
Argon gas flow	
Nebulizer	1.0 L/min
Auxillary	1.8 L/min
Plasma	18.0 L/min
Lens voltage	
Mirror Lens Left	37 V
Mirror Lens Right	31 V
Mirror Lens Bottom	30 V
Sample uptake rate	90 s

(b) Data acquisition parameters for quantitative mode

Measuring mode	Segmented Scan
Point per peak	5
Scans/Replicate	5
Replicate/Sample	5
Dwell time (ms)	1
Integration time (s)	395.08 s

3. Results and discussion

The 1st Daughter Directive of the EU Air Quality Framework Directive promulgates an annual limit value of 0.5 μg/m^3. The recent proposal of the European Commission for a directive relating to toxic metals set assessment thresholds for Cd and Ni. The mean annual concentration proposed 20 ng/m^3 for Ni and 5 ng/m^3 for Cd, all measured in the PM10 particulate fraction.

Under the optimized conditions, the resulting calibration curves for all analyte elements, obtained by the established method, are given in table 3. It can be seen clearly that within the ranges of the amounts of analyte elements studied, all calibration curves of these analyte elements are linear. Prior to analysis of samples, a quality control sample prepared from ICP Multi Element Standard Solution VI CertiPUR was analyzed to verify the calibration.

Tabel 3.

Calibration curves (y = a + bx) for the analyte elements obtained by ICP-MS Varian 820

Element	Range (μg/L)	Calibration curve, y = a + bx	Correlation coefficient, r
Ni	1-50	Y=18390x+146.4	0.9999
Cd	1-50	Y=23810x-2452.8	0.9999
Cr	1-50	Y=81740x+130107	0.9999
Co	1-50	Y=86080x+30372.3	0.9998
Pb	1-50	Y=42330x+7970	0.9999
Cu	1-50	Y=19820x+5787.3	0.9999
Mn	1-20	Y= 123600x+340293	0.9999

y = c/s; x = concentration

The laboratory blanks of unused filter strips contained the followed elements: Ni, Cd, Cr, Co, Pb, Cu and Mn. Therefore, filter-blank background subtraction was performed in the final calculations. The ICP-MS analyses were performed using the quantitative mode.

The digestion procedure show the requirements of the EN ISO 14902 for Pb, Cd and Ni. Recoveries of 85±5 % were also achieved for Cr, Co and Cu.

Instrumental detection limits of analyte elements obtained by ICP-MS and the average concentrations in atmospheric particulate matter collected are presented in Table 4.

Measured concentrations of Ni, Cd, Cr, Co, Pb, Cu and Mn in the industrial area of Valcea are lower than the respective assessment thresholds of European Commission. However, one should bear in mind that the determination of the exceedance of assessment thresholds requires a large monitoring periods (1 year).

Table 4.

Instrumental detection and the concentrations in atmospheric particulate matter (PM10) collected in the period august-october 2009 in the industrial area of Valcea (2 samplings /month)

Element	Instrumental Detection Limit (ng/m^3)	The concentration in the atmosphere (ng/m^3) in the period august-october 2009 (2 samplings/month)	
Ni	0.165	3.1437	2.896
		4.895	5.341
		6.7005	7.352
Cd	0.262	0.1361	0.1288
		0.563	0.977
		0.7943	1.0237
Cr	1.216	2.2629	2.678
		3.788	3.998
		8.7413	6.789
Co	0.148	0.3727	0.2556
		0.5006	0.6024
		0.5399	0.6234
Pb	4.292	18.6997	15.034
		27.7076	7.23
		4.8879	3.623
Cu	1.655	13.435	12.003
		17.4356	18.324
		29.4911	30.876
Mn	-	19.7501	18.659
		15.9634	16.012
		25.1578	22.189

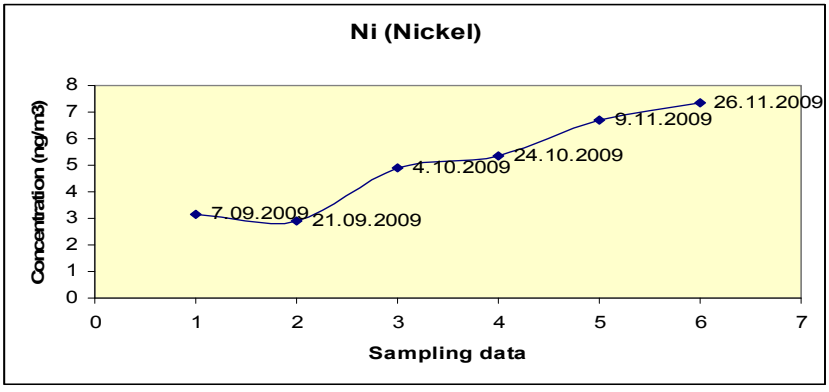

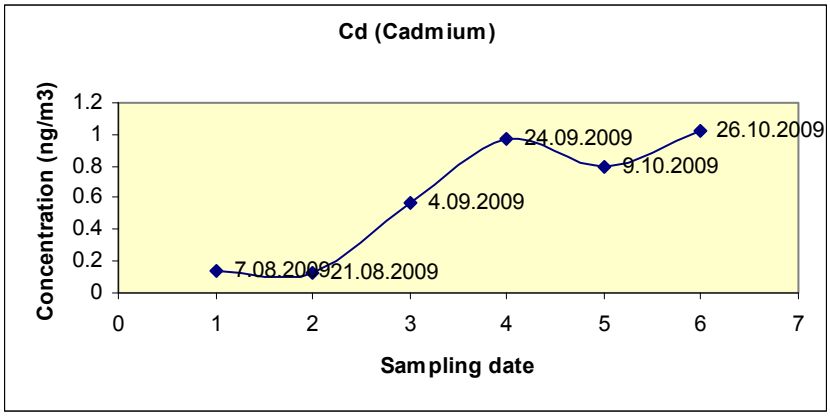
Cd (Cadmium)
Concentration (ng/m3)
1.2
1
0.8
0.6
0.4
0.2
0
0
1
2
3
4
5
6
7
Sampling date
7.08.2009
21.08.2009
4.09.2009
24.09.2009
9.10.2009
26.10.2009

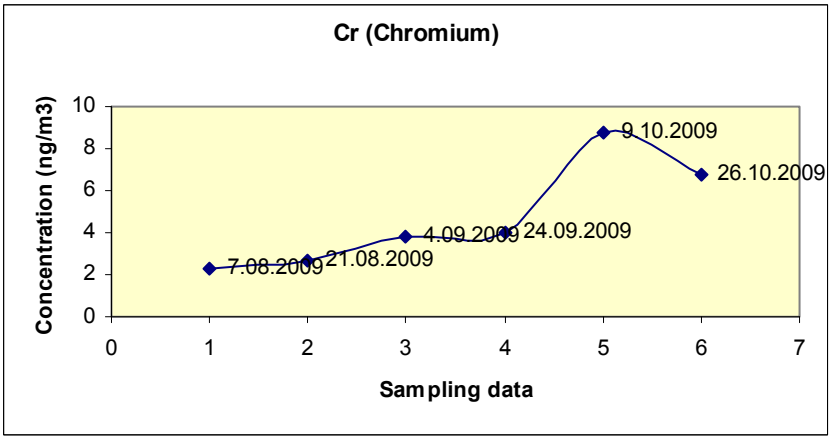
Cr (Chromium)
Concentration (ng/m3)
10
8
6
4
2
0
0
1
2
3
4
5
6
7
Sampling data
7.08.2009
21.08.2009
4.09.2009
24.09.2009
9.10.2009
26.10.2009

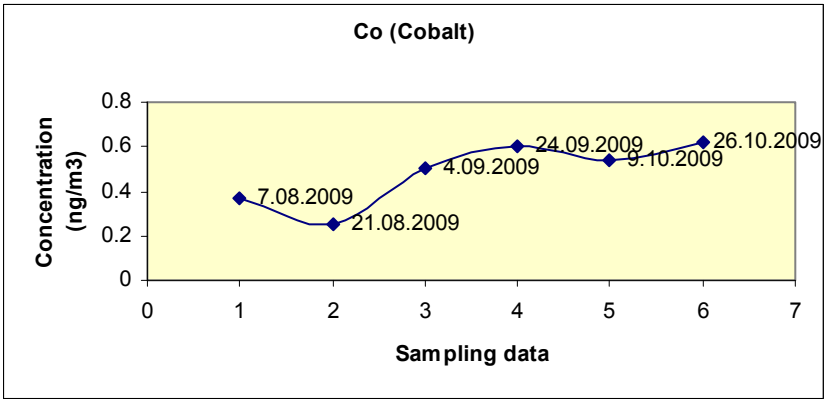
Co (Cobalt)
Concentration (ng/m3)
0.8
0.6
0.4
0.2
0
0
1
2
3
4
5
6
7
Sampling data
7.08.2009
21.08.2009
4.09.2009
24.09.2009
9.10.2009
26.10.2009

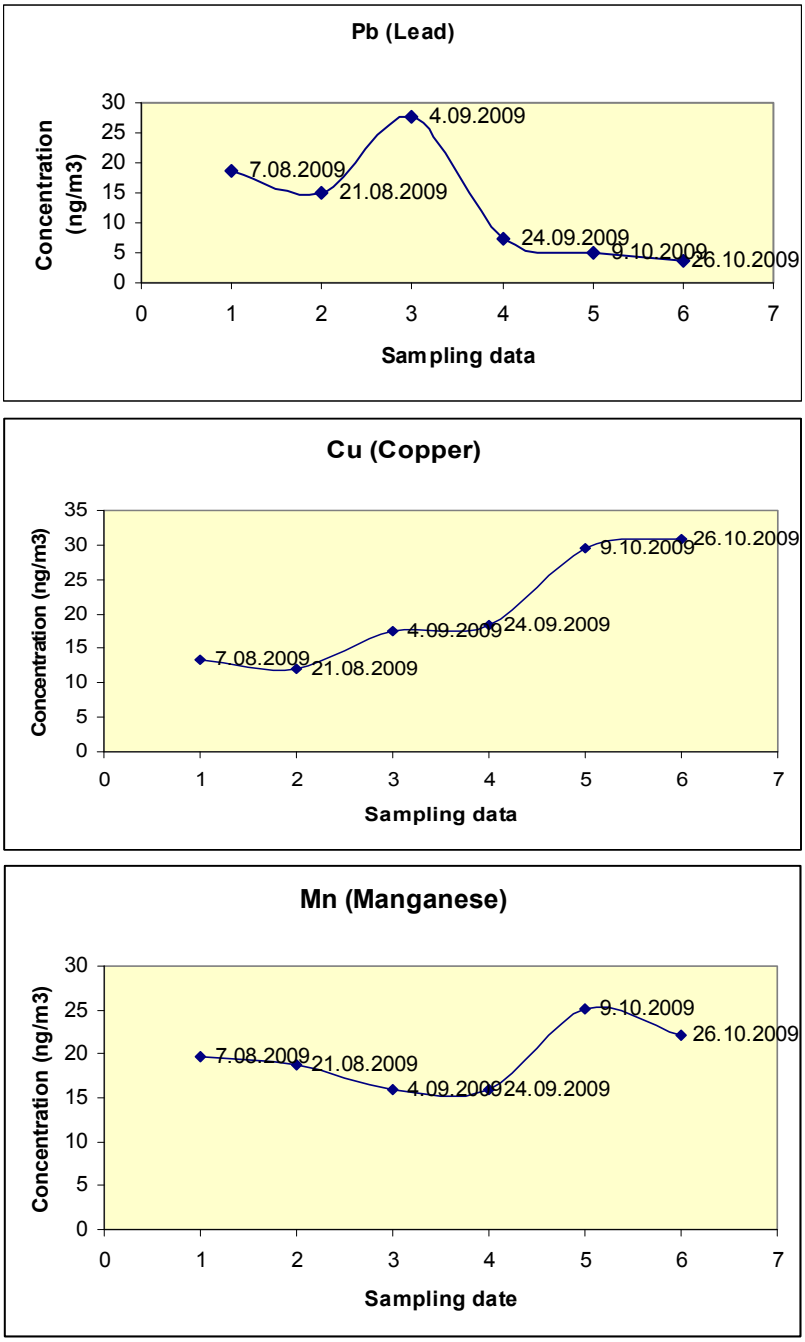

Figure 1. Variation of concentration of different trace metals in Valcea air during the period august-october 2009

The results of this work represent our contribution for determination the trace metals composition of PM10 particulate matter from industrial area, for three months.

4. Conclusions

The trace elements concentration in atmospheric particulate matter collected in the period august-october 2009 in the industrial air of Valcea area, analyzed by microwave-assisted digestion of filter-based samples followed by ICP-MS determinations showed that the values of concentrations for Pb, Cd and Ni and could exceed the annual limit value of the EU Air Quality Framework Directive.

REFERENCES

1. Mészáros E. Fundamentals of atmospheric aerosol chemistry. Budapest: Akadémiai Kiadó; 1999.
2. Dockery DW, Pope CA, Xu XP, Spenger JD, Ware JH, Fay ME, Ferris BG, Speizer FE. An association between air-pollution and mortality in 6 United-states cities. New Eng J Med 1993;329:1753-9.
3. Seinfield JH, Pandis SN. Atmospheric chemistry and physics. From air pollution to climate change. New York: John Wiley & Sons; 1998./McMurry PH. A review of atmospheric aerosol measurements. Atmos Environ 2000;34:1959-99).
4. Heal MR, Hibbs LR, Agius RM, Beverland IJ. Total and water-soluble trace metal content of urban background PM10, PM2.5 and black smoke in Edinburgh, UK. Atoms Environ 2005;39:1417-30.
5. H. Puxbaum, B. Gomisce, M. Kalina, H. Bauer, A. Salam, S. Stopper, O. Preining, H. Hauck, A dual site study of PM2.5 and PM10 aerosol chemistry in the larger region of Vienna, Austria, Atmospheric Environment (2004) 38: 3949–3958.
6. P. Chandra Mouli, S. Venkata Mohan, V. Balaram, M. Praveen Kumar, S. Jayarama Reddy, A study on trace elemental composition of atmospheric aerosols at a semi-arid urban site using ICP-MS technique, Atmospheric Environment (2006) 40:136–146.